Computational Prediction of Transport Properties in Battery Materials

by

Sheng Yang

A dissertation submitted in partial fulfillment
of the requirements for the degree of
Doctor of Philosophy
(Physics)
in the University of Michigan
2018

Doctoral Committee

Associate Professor Donald Siegel, Co-Chair
Professor Rachel S. Goldman, Co-Chair
Professor Cagliyan Kurdak
Assistant Professor Xiaoming Mao
Associate Professor Jeff Sakamoto

Sheng Yang

physheng@umich.edu

ORCID iD: 0000-0001-9642-2213

Acknowledgements

First and foremost, I would like to thank my advisor, Professor Siegel, for giving me invaluable mentorship in my Ph.D. studies. He provided inspiring suggestions on my research, and guided me in writing scientific papers.

Next I would like to thank Professor Juan Maria García Lastra and Tejs Vegge in Technical University of Denmark. I am grateful for the enlightening discussion with them. I am also grateful to Professor Rachel Goldman, Jeff Sakamoto, Xiaoming Mao, Cagliyan Kurdak for their valuable advice and serving on my dissertation defense committee. I additionally thank Dr. Nicolai Rask Mathiesen, Dr. Travis Thompson, and Dr. Woo-ram Lee. The collaborations with them are very enjoyable and fruitful. From our research group, I benefit a lot from the discussions with Dr. Maxwell Radin, Seungho Yu, Haesun Park and Jeff Smith.

Last but not least, a sincere thank you to my parents, my aunt and my grandmother, for their unconditional love, dedication and mental support in my life. They are always behind me facing obstacles. Without their encouragement and understanding, this endeavor would have been much more challenging.

Table of Contents

Acknowledgements **ii**

List of Figures **vi**

List of Tables **xi**

Abstract **xii**

Chapter 1 : Introduction **1**

1.1 Motivation 1

1.2 Solid-state Li metal batteries 2

1.3 Metal Oxygen Batteries 5

1.4 Lithium-O_2 batteries 7

1.4.1 Discharge/Recharge Mechanisms 8

1.4.2 Challenges. 10

1.5 Sodium-O_2 battery 11

1.6 Potassium-O_2 battery 12

1.7 Goals and Outline of this Dissertation 13

Chapter 2 : Methodology **15**

2.1 Kohn-Sham Density Functional Theory 15

2.2 Exchange-correlation functionals 18

2.3 GW methods 21

2.4 Implementation 23

2.5 Point Defects 24

2.5.1 Thermodynamics 24

2.5.2 Kinetics 27

2.6 Molecular dynamics 29

2.6.1 Principles of Molecular dynamics 29

2.6.2 Molecular Dynamics Potentials 30

Chapter 3 : Intrinsic Defect Conductivity in Na-O_2 Battery Discharge Phases: Na_2O_2 *vs.* NaO_2 **33**
3.1 Introduction 33
3.2 Methodology 36
3.3 Results and Discussion 37
3.3.1 Structure and Bandgaps. 37
3.3.2 Intrinsic Defects in Na_2O_2. 39
3.3.3 Intrinsic Defects in NaO_2 44
3.3.4 Mobilities 47
3.3.5 Conductivity 51
3.4 Conclusion 54
Chapter 4 : Intrinsic Defect Conductivity in LiO_2 and KO_2 **56**
4.1 Introduction 56
4.2 Methodology 58
4.3 Results and discussion 62
4.3.1 Structure and Bandgaps 62
4.3.2 Intrinsic Defects in LiO_2 66
4.3.3 Intrinsic Defects in KO_2 69
4.3.4 Defect mobilities 71
4.3.5 Superoxides Comparison 73
4.3.6 Conductivity 74
4.4 Conclusion 77
Chapter 5 : Crossover of Transition Metal Impurities Impedes Li-ion Transport in the Solid Electrolyte LLZO **78**
5.1 Introduction 78
5.2 Methodology 80
5.2.1 Computational models for LLZO. 80
5.2.2 Molecular Dynamics Simulation. 81
5.2.3 Sample Preparation and Characterization. 82
5.2.4 Cobalt Diffusion Model. 83
5.3 Results and discussion 84
5.3.1 Co Diffusion Across the LLZO/LCO Interface. 84

5.3.2 Low-Energy LLZO Structures. 87
5.3.3 Molecular Dynamics Simulations of Transition Metal and Li-Ion Transport. 89
5.4 Conclusion 96
Chapter 6 : Conclusions **97**
6.1 Transport in peroxides and superoxides 97
6.2 Solid electrolyte with transition metal impurities 99
6.3 Outlook and Future work 100
Bibliography **101**

List of Figures

Figure 1.1 Gravimetric and Volumetric Energy Densities for commercial Li-ion batteries and beyond Li-ion batteries. The discharge products for beyond Li-ion batteries are noted in parentheses. The energy density values are calculated based on the active components only. 1

Figure 1.2 Schematic of a Solid State Electrolyte Lithium ion battery with Li metal and an intercalation cathode (transition metal oxides). During discharge, Li+ carry the current within the battery from the anode to the cathode, through the solid state electrolyte. At external circuit, electron flows from anode to cathode. During charging, the lithium ions then migrate from the cathode to the anode while an external electrical power source (the charging circuit) applies a voltage to make electron flow from cathode to anode. 2

Figure 1.3 Schematic of a M-O_2 cell. Blue represents an alkali metal negative electrode, gray the separator, green the organic liquid electrolyte, black a porous carbon positive electrode support, yellow a catalyst, and gray the discharge product. 5

Figure 1.4 SEM images of the discharge products of (a) Li-O_2 cell (b) Na- O_2 cell (discharge to Na_2O_2) (c) Na-O_2 cell (discharge to NaO_2) (d) K-O_2 cell. Taken from (a) Lu *et.al.*[186] (b) Li *et.al.*[187] (c) Hartmann *et.al.*[75] (d) Ren *et.al.*[42] 7

Figure 1.5 Typical galvanostatic discharge-charge voltage profile of alkali metal-O_2 batteries. Taken from (a) Aurbach et. al.[63] (b) Hartmann et.al.[75] (c) Sun et.al.[76] (d) Ren et.al.[42] 10

Figure 3.1 Molecular Orbital (MO) diagrams for: (a) oxygen (O_2^0), (b) superoxide (O_2^{1-}) and, (c) peroxide (O_2^{2-}) dimers..... 34

Figure 3.2 Crystal structures of (a) hexagonal Na_2O_2 viewed along two directions, and (b) cubic (pyrite) NaO_2. Yellow spheres represent oxygen atoms; blue spheres are sodium atoms.... 37

Figure 3.3 Defect formation energy of the O vacancy (red lines), Na vacancy (green lines), electron polarons and hole polarons (black lines) obtained using the HSE_α ($\alpha = 0.48$) hybrid functional in Na_2O_2. There are two symmetry inequivalent oxygen and sodium. The solid line represents

the oxygen or sodium defects in oxygen-rich layer, while the dashed line represents the oxygen or sodium defects in oxygen-poor layer. 39
Figure 3.4 Magnetization Density for (a) hole polaron in Na_2O_2; (b) electron polaron in Na_2O_2; (c) hole polaron in NaO_2; and (d) electron polaron in NaO_2. Note that in panels (c) and (d) the bond axis of the oxygen dimers is into the plane of the page. The color scheme is set such that blue represents a magnetization density of zero, and red corresponds to 0.27 μ_B/Bohr^3..... 42
Figure 3.5 Density of States (DOS) of Na_2O_2 calculated using HSE_α ($\alpha = 0.48$). (a): DOS for the pristine compounds. (b): DOS projected onto an electron polaron cluster. (c): DOS projected onto a hole polaron cluster. A cluster is defined as an oxygen dimer and its nearest neighbor sodium ions. 42
Figure 3.6 Defect formation energy of the O vacancy (red lines), Na vacancy (green lines), electron polarons and hole polarons (black lines) obtained using the HSE_α ($\alpha = 0.48$) hybrid functional in NaO_2..... 44
Figure 3.7 Density of States (DOS) of NaO_2 calculated using HSE_α ($\alpha = 0.48$). (d): DOS for the pristine compounds. (e): DOS projected onto an electron polaron cluster. (f): DOS projected onto a hole polaron cluster. A cluster is defined as an oxygen dimer and its nearest neighbor sodium ions. 46
Figure 3.8 Energy barriers calculated using the NEB method for (a) ionic charge carriers and (b) polarons. Blue curves refer to NaO_2; black curves refer to Na_2O_2. For simplicity, only pathways with barriers less than 1 eV are shown. In panel (a) barriers are plotted for migration of three ionic species in NaO_2: negative sodium vacancies (V_{Na}^-), positive sodium interstitials (Na_i^+), and positive oxygen dimer vacancies ($V_{O_2}^{1+}$). One pathway between nearest-neighbor V_{Na}^-, Na_i^+ and $V_{O_2}^{1+}$ are considered. In Na_2O_2 only sodium vacancies (V_{Na}^-) are relevant, and five distinct pathways were considered between two symmetry inequivalent V_{Na}^- sites. In panel (b), electron polaron (e_p^-) and hole polaron (h_p^+) hopping barriers are compared with those for hole polaron hopping in Li_2O_2 from Radin *et al.*[55] (green dashed lines). 48
Figure 3.9 Nearest neighbor defect hopping (migration) pathways in NaO_2. The central O_2 has its bond axis normal to the plane of the page. The three arrows represent the directions of possible hops to the three nearest-neighbor O_2 sites. 49

Figure 3.10 Single point energy barriers for hopping of (a) hole polarons (h_p^+), (b) electron polarons (e_p^-), and (c) positive oxygen dimer vacancies (V_{O2}^+) in NaO_2 along the three directions depicted in Figure 3.9. 49
Figure 4.1 Crystal structures of (a) Orthorhombic LiO_2 (b) KO_2 (Precession) (c) KO_2 (High Symmetry Tetragonal). Red spheres represent oxygen atoms; Green spheres represent Li atoms; purple spheres are potassium atoms. 63
Figure 4.2 Precession model of KO_2 viewing from (a) [010] direction and (b) [001] direction. The O_2 rotation energy map with tetragonal constraint and keeping theta = 22°. Figure courtesy from Nicolai Rask Mathiesen. 63
Figure 4.3 Density of states (in arbitrary units) plots for bulk LiO_2 calculated using four different methods: (from top to bottom) GGA, HSE06, HSE ($\alpha = 0.48$) and HSE+G_0W_0. 64
Figure 4.4 Density of states (in arbitrary units) plots for bulk KO_2 calculated using four different methods: (from top to bottom) GGA, HSE06, HSE ($\alpha = 0.48$) and HSE+G_0W_0. 64
Figure 4.5 Defect formation energy of the O vacancy, Li vacancy and interstitials, electron polarons and hole polarons obtained using the HSEα ($\alpha = 0.48$) hybrid functional in LiO_2. 65
Figure 4.6 Magnetization density distribution for (a) hole and (b) electron polarons in LiO_2. (c) Structural and magnetic properties of O−O dimers with different charge states. The isosurfaces represent the spin density at the value of 0.04 e $Bohr^{-3}$ 67
Figure 4.7 Defect formation energy of the O vacancy, K vacancy and interstitials, electron polarons and hole polarons obtained using the HSEα ($\alpha = 0.48$) hybrid functional in KO_2. 68
Figure 4.8 Magnetization density distribution for (a) hole and (b) electron polarons in KO_2. (c) Structural and magnetic properties of O−O dimers with different charge states. The isosurfaces represent the spin density at the value of 0.04 e $Bohr^{-3}$. 69
Figure 4.9 Energy barriers calculated using the NEB method for (a) ionic charge carriers and (b) polarons in LiO_2. Blue curves refer to positive lithium interstitials (Li_i^+), green curves represent negative potassium vacancies (V_{Li}^-), and black curves are polarons (e_p^-, h_p^+)..... 70
Figure 4.10 Energy barriers calculated using the NEB method for (a) ionic charge carriers and (b) polarons in KO_2. Blue curves refer to positive potassium interstitials (K_i^+), green curves represent negative potassium vacancies (V_K^-), and black curves are polarons (e_p^-, h_p^+)..... 72
Figure 4.11 Bar plot of different defects (a) formation energies and (b) migration barriers for LiO_2 (white), NaO_2 (black) and KO_2 (grey). 73

Figure 5.1 Cubic $Li_7La_3Zr_2O_{12}$ (cLLZO), illustrating La-O polyhedral, Zr-O octahedra, and the 3D ring structure formed by the partially-occupied Li sublattice. The ring structure contains two symmetry-distinct Li sites: Li1(purple, tetrahedral coordination, 24d) and Li2 (green, octahedral coordination, 96h). 79
Figure 5.2 Optical (left) and SEM (right) images of the LCO/LLZO interface at three temperatures used for interface bonding. Figure courtesy from Woo-ram Lee. 82
Figure 5.3 Co concentration as a function of temperature and of distance normal to the LCO/LLZO interface. Blue data points represent EPMA measurements, while solid lines depict the diffusion profiles obtained from fitting the data with Equation 5.1. 84
Figure 5.4 Raman spectrum of LLZO after diffusion bonding with LCO. The "interface" region corresponds to the LLZO a few microns away from the LCO, the "dark blue" region corresponds to the LLZO which was significantly blue approximately 50-100 microns away from the interface, and the "white" region corresponds to the LLZO which was furthest away from the interface and still white as the native LLZO. N=3 spectra were recorded in each region and averaged. The average along with the standard error ($\pm$ one standard devation / $\sqrt{N}$). Figure courtesy to Travis Thompson. 85
Figure 5.5 Mean Square Displacement (MSD) plots (670 – 1400 K) of Co atoms taken from 2 ns NPT MD simulations for x = 0.5 in $Li_{6.25}Al_{0.25}Co_xLa_3Zr_{2-x}O_{12}$. 86
Figure 5.6 (a) Energy Distribution and (b) standard deviation of Al doped LLZO with two Al atoms on all 24d sites; one on 24d, one on 96h; two on 96h sites, respectively. 87
Figure 5.7 (a) Energy Distribution and (b) standard deviation of Mn doped LLAZO with four Mn atoms on all 24d sites; three on 24d, one on 96h; two on 24d, two on 96h sites; one on 24d, three on 96h sites; four on 96h sites, respectively. 88
Figure 5.8 (a) Energy Distribution and (b) standard deviation of Mn doped LLAZO with four Mn atoms on all 24d sites; three on 24d, one on 96h; two on 24d, two on 96h sites; one on 24d, three on 96h sites; four on 96h sites, respectively. 88
Figure 5.9 (a) Energy Distribution and (b) standard deviation of Ni doped LLAZO with four Ni atoms on all 24d sites; three on 24d, one on 96h; two on 24d, two on 96h sites; one on 24d, three on 96h sites; four on 96h sites, respectively. 89

Figure 5.10 (a) Energy Distribution and (b) standard deviation of Fe doped LLAZO with four Fe atoms on all 24d sites; three on 24d, one on 96h; two on 24d, two on 96h sites; one on 24d, three on 96h sites; four on 96h sites, respectively. 89

Figure 5.11 Probability density isosurfaces for Li and four transition metal impurities in LLAZO at T = 1000 K over a 1 ns MD simulation. (a) Magnified view of a portion of the Li isosurface from a pristine (i.e., impurity-free) LLAZO cell, and for LLAZO cells containing Co, Mn, Ni, or Fe TM impurities. (b). Isosurfaces from the entire simulation cell viewed along <111> depicting the mobility of Li-ions (far left), and for the various TM impurities (2^{nd} through 5^{th} panels). The isosurface level is equal to 10% of the maximum probability density. 90

Figure 5.12 Diffusion coefficient of (a) Li (b) Co as a function of temperatures at different Co concentration (x = 0.125 to x = 0.5) in $Li_{6.25-2x}La_3Al_{0.25}Co_xZr_2O_{12}$..... 91

Figure 5.13 Arrhenius plots of (a) diffusivity of transition metals (Fe, Co, Mn, Ni) in LLAZO and Li in pristine LLAZO; (b) diffusivity of Li in LLAZO containing transition metal impurities. Black circles in panel (a) represent the Co diffusivity as estimated from EPMA measurements..... 93

List of Tables

Table 1.1 Calculated thermodynamic parameters and energy densities of various non-aqueous, . 6
Table 2.1 Summary of GW methods. 23
Table 3.1 Calculated bandgaps for Na_2O_2 and NaO_2 at different levels of theory. In the case of NaO_2, values are reported for both the low temperature (Marcasite, *Pnnm*) and intermediate temperature (Pyrite, *Pa3*) phases. 38
Table 3.2 Defect formation energies E_f (eV) and concentrations C (cm^{-3}) in Na_2O_2 40
Table 3.3 Defect formation energies E_f (eV) and concentrations C (cm^{-3}) in NaO_2 45
Table 3.4 Calculated ionic and electronic conductivities (S cm^{-1}) for Na_2O_2 and NaO_2, and their comparison with prior calculations on Li_2O_2. For ionic conductivities in NaO_2, the first value refers to contributions from positive oxygen dimer vacancies ($V_{O_2}^{1+}$), the second value refers to contributions from sodium vacancies (V_{Na}^{-}). 51
Table 4.1 The calculated magnetic ordering, energy between ferromagnetic ordering and antiferromagnetic ordering, lattice parameters a, b, c (Å), O-O bond length dO-O (Å), the distance between Li atom and its nearest O atom dM-O_2 (Å), and the oxygen dimer orientation. 62
Table 5.1 Calculated activation energies (E_a) for transition metal (TM) diffusion in LLAZO (E_a (TM)) and for Li ion diffusion in pristine and TM-containing LLAZO (E_a (Li)). R_B refers to the bottleneck radius (R_B) for diffusion in pristine and TM-containing LLZO. 94

Abstract

Electric vehicles would benefit from batteries with higher energy densities, longer cycle lifetimes, and enhanced safety. State-of-art Li-ion batteries exhibit specific energy densities near 0.26 kW kg–1, limiting the range of electric vehicles and slowing their adoption. Among future battery chemistries, metal-oxygen batteries and solid electrolyte/Li-metal batteries have attracted attention due to their potential to achieve these performance gains.

The first goal of this thesis is to predict the electronic and ionic transport properties in the discharge products of metal-oxygen batteries based on alkali-metal anodes (i.e., Li-O_2, Na-O_2, and K-O_2 batteries). Peroxides (Li_2O_2, Na_2O_2) or superoxides (LiO_2, NaO_2, KO_2) are the primary discharge products in these batteries. Cells that discharge to superoxides exhibit low charging overpotentials, while those that discharge to peroxides do not. These differences could arise from a higher conductivity within the superoxide; however, this explanation remains speculative given that charge transport in superoxides is relatively unexplored. Here, density functional and quasi-particle methods are used to assess the electronic and ionic conductivities of metal-oxygen discharge products by calculating the equilibrium concentrations and mobilities of intrinsic charge carriers in Na_2O_2, LiO_2, NaO_2 and KO_2. All compounds are predicted to be electrical insulators, with band gaps exceeding 4 eV.

Ionic conductivity in Na_2O_2 is mediated by negative sodium vacancies, while it is governed by positive oxygen dimer vacancies in lithium, sodium, and potassium superoxides. The predicted ionic conductivities of the superoxides range from 9×10^{-12} to 4×10^{-9} S/cm. These values are 8 to 10 orders of magnitude larger than those in lithium and sodium peroxide (9×10^{-19} to 5×10^{-20} S/cm).

Electronic transport in the peroxides and superoxides is mediated by the hopping of polarons localized on O_2 dimers. The predicted equilibrium electronic conductivity in LiO_2, 9×10^{-12} S/cm, is 8 orders of magnitude larger than in Li_2O_2, Na_2O_2, NaO_2, and KO_2 (10^{-19} to 10^{-20}

S/cm). The moderate conductivity predicted for LiO_2 may explain the low overpotentials observed in LiO_2 cells. However, given that high conductivities are not predicted for NaO_2 or KO_2, the enhanced efficiency of these systems should not be attributed to enhanced charge transport; other factors, such as a reduced tendency for electrolyte decomposition, likely explain the small overpotentials in these systems.

A second goal of this dissertation is to assess the impact of transition metal (TM) impurities on the performance of $Li_7La_3Zr_2O_{12}$ (LLZO) solid electrolytes. These impurities are formed by crossover from Li-ion cathodes during interface formation. The presence of TMs in LLZO is hypothesized to impede Li-ion migration, however, the mechanisms responsible for this effect are not understood. Molecular dynamics simulations were used to evaluate the transport rates of Co and three other TMs (Mn, Fe, and Ni) in Al-doped LLZO, and to predict how TM impurities impact Li-ion migration. Fe impurities are the most mobile of the TMs investigated; nevertheless, all TMs exhibit lower diffusivities compared to Li. Importantly, the presence of TMs slows Li-ion migration, with the magnitude of the slowing following the same trend as the TM diffusivities. Because the TMs also migrate along the Li-sublattice, slower-moving TMs impede Li-ion migration via a traffic-jam process. Our work highlights a tradeoff associated with the synthesis of LLZO/cathode solid interfaces: although high-temperature processing increases interfacial contact, and lowers impedance, the use of high temperatures also increases TM crossover from cathode to solid electrolyte, reducing Li-ion mobility.

Chapter 1: Introduction

1.1 Motivation

The transition to a sustainable energy economy is contingent upon the capability to not only generate energy cleanly and efficiently, but also to store energy effectively[1]. Among various storage technologies, Li-ion batteries (LIBs) have emerged as the chief energy storage technology for applications that demand a high energy density, especially electric (and hybrid-electric) vehicles and consumer electronics. LIBs currently occupy 63% of worldwide battery sales with an estimated global market of $213.5 billion by 2020.[2]

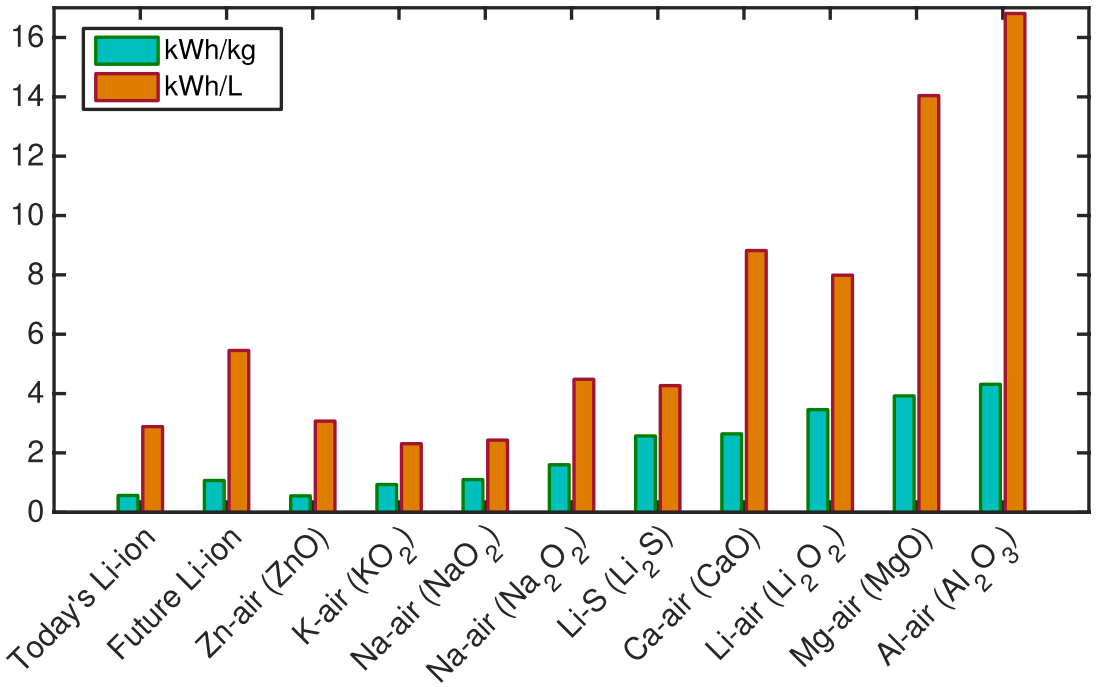

Figure 0.1 Gravimetric and Volumetric Energy Densities for commercial Li-ion batteries and beyond Li-ion batteries. The discharge products for beyond Li-ion batteries are noted in parentheses. The energy density values are calculated based on the active components only.

Despite the large and growing use of LIBs worldwide, improvements to their energy density has occurred at a slow pace. The growth rates of energy densities of LIBs based on watt-hours per kilogram (Wh kg^{-1}) and watt-hours per liter (Wh L^{-1}) are typically 7−8% per year.[3] As current LIBs approach the theoretical limits of their cathode/anode materials, the development of new/advanced electrode materials is highly desirable in order to achieve additional gains in energy density. Figure 1.1 summarizes the gains that may be possible for several 'beyond Li-ion' battery chemistries.

1.2 Solid-state Li metal batteries

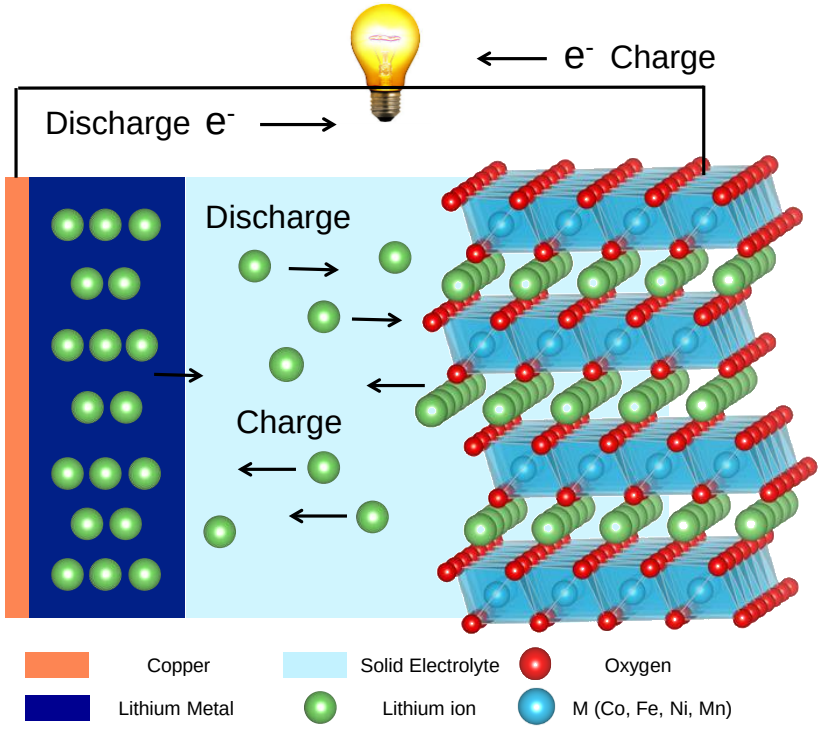

Figure 1.2 Schematic of a Solid State Electrolyte Lithium ion battery with Li metal and an intercalation cathode (transition metal oxides). During discharge, Li+ carry the current within the battery from the anode to the cathode, through the solid state electrolyte. At external circuit, electron flows from anode to cathode. During charging, the lithium ions then migrate from the cathode to the anode while an external electrical power source (the charging circuit) applies a voltage to make electron flow from cathode to anode.

The anode materials of current state-of-art LIBs are constructed from graphite and other carbon materials. One way to improve the energy density of Li-ion batteries is to use Li metal as the anode, which leads to a significantly improved energy density compared with that of commercial

LIBs (up to 0.26 kWh kg^{-1}).[4–8] Nevertheless, the rechargeable Li metal battery based on an organic liquid electrolyte (such as electrolytes with carbonates or ethers as solvents) shows an unstable chemistry at the Li/electrolyte interface, which turns out to induce severe outcomes.[9,10] For example, the formation of dendrites may lead to internal short-circuiting of the battery and pulverization of the anode.[11–15] The unstable interfacial chemistry also brings the solid electrolyte interface (SEI), which lowers the Columbic efficiency, depletes the electrolyte, and increases the interfacial resistance.[16] Moreover, these electrolytes are also flammable and volatile.[14,15] Therefore, the use of a liquid electrolyte presents severe challenges to the use of high-capacity Li-metal anodes.

Due to the instabilities between the lithium anode and liquid electrolytes, solid-state Li metal batteries have been increasingly researched. A model solid-state battery would consist of an intercalation cathode (IC), a lithium anode (LA), and a solid-state electrolyte (SSE). The most commonly used cathode material is $LiCoO_2$ (LCO), with several other compositions also in use or development. Examples include $LiNiO_2$ (LNO), $LiMnO_2$ (LMO), $LiFePO_4$ (LFP), $LiNi_{0.5}Mn_{0.5}O_2$, and $Li(Ni_{1/3}Mn_{1/3}Co_{1/3})O_2$.[17–20] The electrolyte should block electric contact of the electrodes, yet allow for facile Li^+ transport between electrodes. By eliminating the flammable liquid electrolyte, the safety of the battery can be significantly improved.[3,7] Furthermore, the shift from a liquid electrolyte to SSE is expected to significantly improve the energy density; 40 and 70% increases in specific energy and volumetric density, respectively, are projected.[7] Finally, dendrite formation is significantly suppressed, especially when the discharge/charge process of the batteries is performed at a low current density. Therefore, SEI stabilization by the SSE may bring a higher efficiency for the anode and a longer cycle life for the battery.[7]

Solid electrolytes can be divided into two major groups: inorganic solids (crystalline, glass or glass-ceramic) and organic solid polymers. Polymer-based electrolytes can potentially be low cost, improved electrode | SSE interface compared with liquid electrolyte, and their compliance can compensate for volume changes of the electrodes during battery cycling.[16] However, the polymer electrolytes' lithium-ion conductivity at room temperature is too low for most applications (minimum requirements for Li^+ conductivity at 25 °C is 10^{-5} S/cm)[21]; sufficient conductivities are often not achieved for temperatures below 80 °C.[22] Furthermore, the highest occupied molecular orbitals of many polymers are too low in energy to be compatible

with high-voltage cathode materials (with voltage outputs > 4.0 V vs Li+/Li).[21] This feature makes many polymers susceptible to oxidation when interfaced with cathodes.

Regarding inorganic solids, the garnet ceramics (such as $Li_7La_3Zr_2O_{12}$) and sulfide-based glass−ceramics (such as $Li_{10}GeP_2S_{12}$) are two types of widely investigated SSEs due to their high ionic conductivity (10^{-3} to 10^{-2} S cm^{-1}) compared with the values of liquid electrolytes. $Li_7La_3Zr_2O_{12}$ (LLZO) is regarded as an ideal candidate for lithium-ion batteries due to its large electrochemical window, robust mechanical property, thermal stability and safety.[16] The cubic phase of LLZO exhibits a room temperature ionic conductivity up to 2×10^{-4} S cm^{-1}. This high conductivity arises from the partially-occupied nature of its Li-sublattice, which forms a 3D percolating network and results in isotropic Li transport.[23] In undoped LLZO the cubic phase is unstable at temperatures below ~630 °C, and will transform to the thermodynamically stable tetragonal phase. The tetragonal phase exhibits a relatively low Li-ion conductivity at room temperature.[24] Doping with supervalent cations such as Al^{3+} and Ga^{3+} on the Li-sublattice,[25,26] or with Nb^{5+}, Te^{6+} and Ta^{5+} on the Zr-sublattice,[27–29] stabilizes the cubic phase at room temperature.

A viable solid electrolyte must also exhibit favorable interfacial properties with the electrodes. In the case of LLZO/cathode interfaces, some studies have reported (electro)chemical decomposition at these interfaces during cell cycling.[30,31] These reactions can result in an increase in interfacial impedance and a reduction in power density.[30,31] Interfacial properties are also of importance during synthesis/assembly of solid state cells. For example, the hot-pressing techniques used to archive high density LLZO pellets can also be used to form low-porosity solid-solid interfaces between an LLZO pellet and a cathode pellet.[32] The high temperatures used during processing can potentially result in side reactions and interdiffusion of species between the cathode and LLZO. These effects can also increase interfacial impedance.

Regarding the LLZO/cathode interface, there exist conflicting reports about the interfacial resistance of this system. Take the most commonly used cathode material $LiCoO_2$ (LCO) as an example, some authors reported no evidence of interfacial resistance, even after cycling.[33,34] In contrast, Kotobuki *et al.* and Kim *et al.* reported poor performance at LLZO/LCO interfaces caused by cross-over of La, Zr, and Co, resulting in increased interfacial resistance.[30,31] In another recent study, Park *et al.* found that the high temperature processing used to fuse LCO and LLZO pellets induced cross-diffusion of species and formation of the tetragonal LLZO at the interface, which impacted Columbic efficiency and cycle life.[35] Finally,

Miara *et al.* used density functional theory (DFT) calculations to investigate the stability of the solid electrolyte/cathode interface.[36] Their calculations showed that LCO was relatively stable during cycling compared with $LiMnO_2$ (LMO) and $LiFePO_4$ (LFP), and they predict decomposition of Co^{3+}(Zr) LLZO into La_2O_3, $Li_6Zr_2O_7$ and Li_8CoO_6 at high temperatures, leading to large interfacial resistance.

The crossover rates of the transition metals (TMs) and their effect on the lithium ion conductivities in solid electrolyte still need to be explored. In our recent work, a combination of experimental and computational techniques was performed to understand the TM cross-over from cathode materials to a solid electrolyte. See Chapter 4 in detail.

1.3 Metal Oxygen Batteries

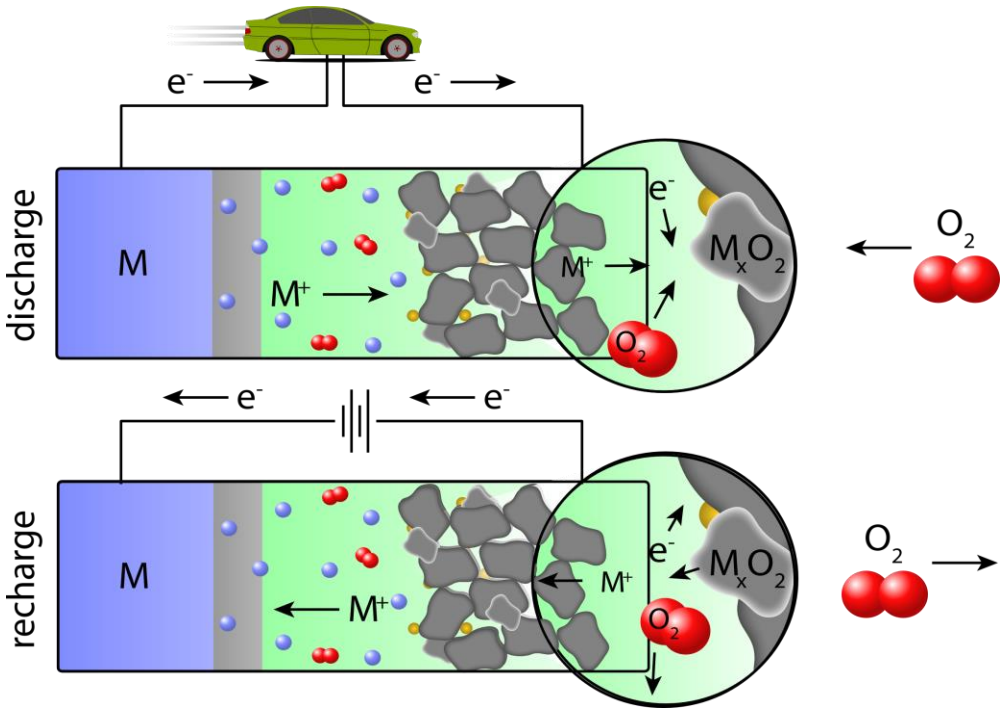

Figure 1.3 Schematic of a M-O_2 cell. Blue represents an alkali metal negative electrode, gray the separator, green the organic liquid electrolyte, black a porous carbon positive electrode support, yellow a catalyst, and gray the discharge product.

Another promising category of future battery technologies is metal-oxygen batteries. In contrast to conventional Li-ion batteries based on intercalation reactions, metal-oxygen batteries rely on the electrochemical reduction of molecular oxygen at the cathode surface. The most advanced

and mature examples of metal oxygen technologies are primary cells, using aqueous electrolyte solutions (e.g., Zn-O_2[37], Al-O_2[38], and Ca-O_2[39]). Unfortunately, these primary cells are not designed to be electrically recharged. In contrast, non-aqueous metal–oxygen batteries (Li-O_2[40], Na-O_2[41], K-O_2[42] and Mg-O_2[43]) are envisioned as being able to achieve high energy densities and rechargeability.

Two processes are relevant for rechargeable non-aqueous metal-oxygen batteries. The first process is called the oxygen reduction reaction (ORR). During discharge, dissolution of metal into ions into the electrolyte occurs on the anode side of the cell, while on the cathode side reduction of dissolved oxygen molecules occurs, forming an insoluble solid discharge product (typically an oxide, peroxide, or superoxide). The second process is referred to as the oxygen evolution reaction (OER). During charge, the discharge product within the cathode is decomposed to regenerate oxygen gas and dissolve metal ions into the electrolyte. In parallel, metal ions are reduced and deposited on the anode side to reform the metallic electrode.

Table 1.1 Calculated thermodynamic parameters and energy densities of various non-aqueous, reversible metal-O_2 batteries.

System	Chemical reaction	Theoretical cell voltage (V)	Theoretical specific energy density (kWh/kg)
Li-O_2	$2Li^+ + O_2 + 2e^- \leftrightarrow Li_2O_2$	2.96	3.46
Na-O_2	$Na^+ + O_2 + e^- \leftrightarrow NaO_2$	2.27	1.1
	$2Na^+ + O_2 + 2e^- \leftrightarrow Na_2O_2$	2.33	1.6
K-O_2	$K^+ + O_2 + e^- \leftrightarrow KO_2$	2.48	0.94
Mg-O_2	$2Mg^{2+} + O_2 + 4e^- \leftrightarrow 2MgO$	2.95	3.92

1.4 Lithium-O_2 batteries

It has been 21 years since Li–O_2 battery was introduced as a promising new battery technology[40] with high theoretical energy density of 3.46 kWh kg^{-1} (Table 1.1). It is often observed that the discharge product of a Li/O_2 cell is crystalline Li_2O_2. A number of different discharge product morphologies for Li_2O_2 have been reported, including disks[44,45], films[45,46], needles[47], and hollow spheres[48]. Among those morphologies, biconcave disks (often referred to as a "toroid") are the most commonly observed (Figure 1.4a).

Although the discharge product is primarily thought of as Li_2O_2, superoxide ions O_2^- have also been reported (occasionally) in the discharge product.[49] It should be noted that solid LiO_2 is difficult to synthesize in pure form because it is known to be thermodynamically stable only at <50K, at room temperature disproportionating to Li_2O_2.[50] The origin of this superoxide component remains unclear. It has been suggested to represent a surface species,[51,52] an oxygen-rich phase located in the inter-plate regions[53], or to be associated with the presence of point defects such as hole polarons[54,55].

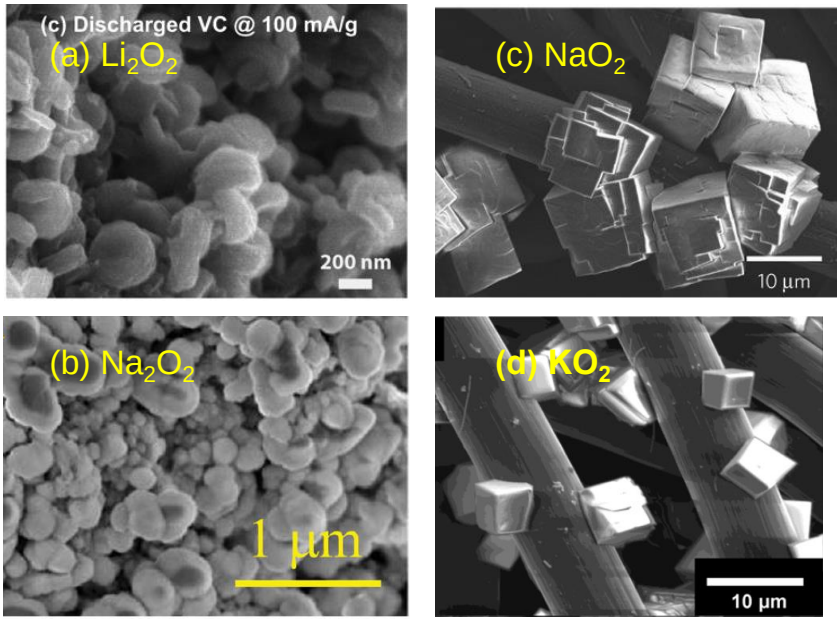

Figure 1.4 SEM images of the discharge products of (a) Li-O_2 cell (b) Na- O_2 cell (discharge to Na_2O_2) (c) Na-O_2 cell (discharge to NaO_2) (d) K-O_2 cell. Taken from (a) Lu *et.al.*[186] (b) Li *et.al.*[187] (c) Hartmann *et.al.*[75] (d) Ren *et.al.*[42].

Recently, Lu *et al.* suggested that it may be possible to stabilize LiO_2 through adsorption on an iridium-based electrode, with the result that LiO_2 becomes the product of the discharge reaction rather than an intermediate.[56] Such a cell shows improved reversibility than the O_2/ Li_2O_2 reaction, and was attributed to the high electronic conductivity of LiO_2. However, the conductivity of LiO_2 remains a matter of debate, because the methods previously used to evaluate the conductivity of this phase are subject to electron delocalization errors and electron correlation errors.[55,57] Additional characterization of the electronic structure of LiO_2 is needed. A detailed discussion of conductivity of LiO_2 using more accurate, hybrid functionals will be presented in Chapter 4.

1.4.1 Discharge/Recharge Mechanisms

O_2 reduction to Li_2O_2 on discharge. A general consensus has been reached that the reduction of O_2 to Li_2O_2 on discharge proceeds as follows. The first step is the one-electron reduction of O_2 to form LiO_2. An equilibrium exists between LiO_2* adsorbed on the electrode and LiO_2 dissolved in the electrolyte solution.[44]

(1.1) $$Li^+ + e^- + O_{2(sol)} \rightarrow LiO_2^*$$

(1.2) $$LiO_2^* \leftrightarrow Li^+ + O_{2(sol)}^-$$

Therefore, the solvation of LiO_2 depends on the LiO_2 solubility and the adsorption free energy of LiO_2* on the electrode.[58–60] Generally in the case for salts dissolved in aprotic solvents, the solubility depends primarily on solvation of the cations by the solvent molecules (Gutmann donor number (DN)[61] and the ionic dissociation strength.[62]

If a solvent has a sufficiently high donor number to strongly solvate Li+ (for example, dimethyl sulfoxide (DMSO), DN = 30), then LiO_2 is dissolved mainly in the electrolyte solution, where it disproportionates to Li_2O_2 that grows as micrometer-sized particles.[58,59]

(1.3) $$2Li^+ + 2O_{2(sol)}^- \rightarrow Li_2O_2 + O_2$$

(1.4) $$2Li^+ + O_{2(sol)}^- + e^- \rightarrow Li_2O_2$$

On the other hand, if Li^+ is weakly solvated (for example, acetonitrile CH_3CN, DN = 14), then LiO_2 is present primarily on the electrode surface, where it undergoes a second electron reduction or disproportionation to form a Li_2O_2 film on the electrode.

(1.5) $$Li^+ + LiO_2^* + e^- \rightarrow Li_2O_2^*$$

(1.6) $$2LiO_2^* \rightarrow Li_2O_2^* + O_2$$

Li_2O_2 oxidation to O_2 on charge. Various mechanisms have been proposed for oxidation of Li_2O_2 deposited as toroid or incorporated into the cathode as a macroscopic particle-containing powder.[63] Ganapathy *et al.* used operando X-ray diffraction to show that a Li-deficient component ($Li_{2-x}O_2$) is formed during the charging process, presumably as a result of a one-electron Li+ de-insertion.[64] This mechanism was also suggested by theoretical studies that showed that topotactic delithiation based on $Li_{2-x}O_2$ is rendered accessible at relatively small overpotentials of 0.3–0.4 V. [55]

A solution-mediated process could also occur during recharge. For example, it has been proposed that impurities present as contaminants or by-products of electrolyte decomposition may serve as soluble intermediate species.[65] These impurities in effect function as redox mediators, or perhaps transform Li_2O_2 into a more soluble species. For example, a small concentration of protons has been suggested to enable a recharge mechanism that begins with the transformation of Li_2O_2 into H_2O_2 via a single-displacement reaction,

(1.7) $$Li_2O_2 + 2H^+ \rightarrow H_2O_2 + 2Li^+$$

Since H_2O_2 is more soluble than Li_2O_2, it could then diffuse to the electrode and be electrochemically oxidized via the reaction

(1.8) $$H_2O_2 \rightarrow 2H^+ + O_2 + 2e^- \ .$$

1.4.2 Challenges.

Thermodynamically, the cell voltage for Li-O_2 battery is 2.96 V. However, practically, the ORR potentials are typically lower, reflecting the existence of an overpotential, and fall in the range of 2.5–2.8 V. The discharge overpotentials can be avoided by using ether-based electrolyte. By introducing new intermediate, Li 2,5-di-tert-butyl-1,4-benzoquinone ($LiDBBQO_2$), which is more stable (lower free energy) than LiO_2.[66] Li–O_2 cells can deliver high rates, high capacities and low discharge overpotential.

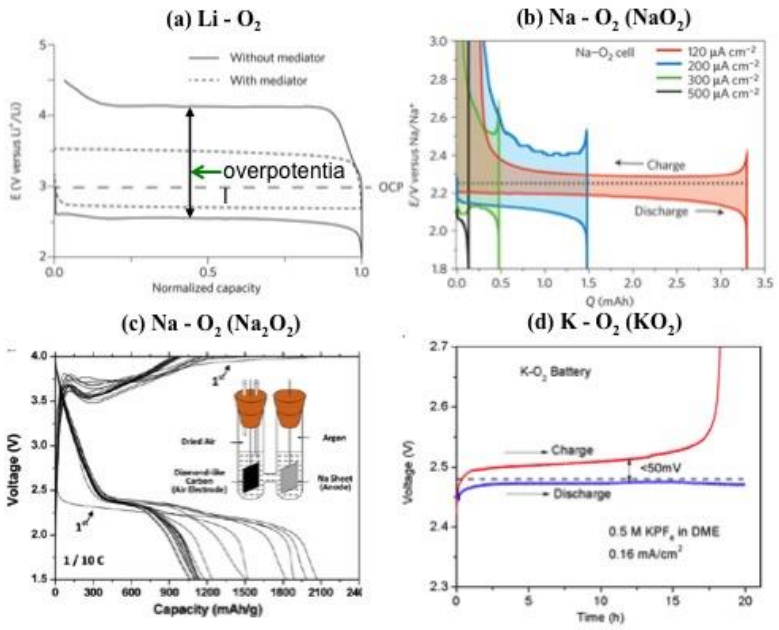

Figure 1.5 Typical galvanostatic discharge-charge voltage profile of alkali metal-O_2 batteries. Taken from (a) Aurbach et. al.[63] (b) Hartmann et.al.[75] (c) Sun et.al.[76] (d) Ren et.al.[42]

The overpotential for OER is even larger; typically > 4 V is required to charge the battery

in the absence of catalyst (Figure 1.5a). The OER overpotential significantly reduces the round-trip efficiency. The lifecycle of Li–O_2 cells, if fully discharged, is limited to less than 10 cycles with extremely low columbic efficiency. The large charging overpotential of Li-O_2 cells remains a big challenge to the commercialization of this battery chemistry. Some factors could substantially contribute to the observed overpotential, such as electrolyte and cathode degradation. For example, many studies reported that the organic carbonate electrolytes react with O_2 or discharge intermediates, resulting in the formation of Li_2CO_3 and CO_2 evolution.[67] As Li_2CO_3 accumulated at the Li_2O_2-electrolyte interface, an increase in overpotential is necessary to maintain the constant current.[68] Using soluble oxidation mediator such as tetrathiafulvalene,[69] 2,2,6,6-tetramethyl-1-piperidinyloxy (TEMPO)[70,71] and LiI,[72–74] the low charge overpotentials can be achieved without severely compromising electrolyte stability. Nevertheless, the search for a perfectly stable mediator with an appropriate operating voltage remains an unsolved challenge.

1.5 Sodium-O_2 battery

As an alternative to lithium-based chemistries, recent experiments have probed the performance of Na-O_2 batteries.[68,75–78] Substituting lithium by sodium offers benefits: (i) sodium salts used in the electrolyte are more abundant than equivalent lithium salts, making them both cheap and easily obtainable.[79] (ii) In contrast to lithium, sodium does not dissolve in aluminum, which enables the use of thin aluminum foil as a light and low-cost anode current collector.

Although Na and Li are both alkali metals, with Na located one row below lithium in the periodic table, the performance of Na-O_2 batteries appears to be very different from that of the analogous Li-O_2 system. For example, in Na-O_2 cells employing non-aqueous electrolytes, some studies have reported Na_2O_2 as the main discharge product,[76] while others report NaO_2.[68,75] Interestingly, Na_2O_2, instead of NaO_2, is the thermodynamically stable form of sodium oxide at room temperature. While Na_2O_2 can be obtained by burning Na in O_2 atmosphere, NaO_2 can be synthesized (chemically) only at liquid ammonia temperature.[41,80–82] From a thermodynamic point of view, with a Gibbs free energy of formation of -449.7 kJ/mol, Na_2O_2 is more stable at standard pressure and room temperature than is NaO_2 (ΔG_f= -437.5 kJ/mol).[83] However, the energy difference between the two forms is only 12 kJ/mol, suggesting that kinetic factors may

stabilize NaO_2. Theoretical calculations suggest that the crystal size could influence the NaO_2 stability.[84] Nano-sized NaO_2 crystals might be more stable than Na_2O_2 and further NaO_2 growth could be kinetically favored.

The possibility for NaO_2 formation during discharge in Na-O_2 batteries offers advantages for battery operation, especially during charging. Cells that discharge to Na_2O_2 exhibit high charging overpotentials, similar to those observed in Li-O_2 batteries (Figure 1.5b). On the other hand, cells that discharge to NaO_2 have much lower charging overpotentials, typically less than 200 meV (Figure 1.5c). [68,75,78]

While the greater mass of sodium implies that a Na-O_2 cell would exhibit approximately 50% lower specific energy compared with a Li-based cell (Table 1.1), the surprising discovery of low overpotentials in superoxide-based Na-O_2 cells suggests an important design strategy. That is, by stabilizing a solid superoxide discharge phase it may be possible to reduce overpotentials for the oxygen evolution reaction (OER) and thereby improve round-trip efficiency. In principle, this strategy could be applied not only for the Na-O_2 system, but also for Li-based and other metal-oxygen systems. In this regard, the Na-O_2 chemistry serves as an important prototype for understanding the connection between the composition of the discharge product and battery efficiency.

1.6 Potassium-O_2 battery

The K-O_2 battery represents another alkali-O_2 chemistry that has recently been reported to be rechargeable (Table 1.1). Different from the Na-O2 system, wherein the discharge product can adopt a range of compositions (NaO_2, Na_2O_2, $Na_2O_2 \cdot H_2O$, or mixtures), in the K-O_2 system KO_2 is the only discharge product observed. Potassium superoxide is thermodynamically stable,[42] and it has been demonstrated that K - O_2 cells containing KPF_6 salt in DME form solely KO_2 (no K_2O_2) during ORR.[42] This discharge product can be completely oxidized during OER. Importantly, the total overpotential for the first cycle was less than 50 mV, which is the lowest among alkali–oxygen cells (Figure 1.5d).[42]

There are few experimental studies of the electronic properties of alkali metal peroxides and superoxides. Thus, it is unclear whether the poor efficiency of peroxide-based cells – and

high efficiency of superoxide-based cells – are related to the conductivity of these phases. One early measurement reported moderately high conductivity in KO_2 (approximately 1-10 S/cm),[85] suggesting that the improved performance of the superoxide-based systems could be traced to their enhanced electronic conductivity. More recent experiments measured the total (electronic + ionic) conductivity of KO_2 at elevated temperatures (345 to 500 K). Extrapolating these data to 300 K yields a much lower value of 10^{-13} S/cm.[86,87] This contradictory result raises our interest to investigate the electronic and ionic defects properties of KO_2 using first principles calculations (Chapter 4).

1.7 Goals and Outline of this Dissertation

The purpose of this thesis is to characterize ionic and electronic charge transport mechanisms in two classes of 'beyond Li-ion' batteries: solid-state Li-ion batteries and metal-oxygen batteries. Roughly one half of this study is focused on the impact of transition metal impurities on the performance of the solid electrolyte LLZO. LLZO is one of promising solid electrolyte materials. To achieve high-density LLZO/cathode pellets, hot-pressing techniques are commonly used. However, the high sintering temperatures can potentially result in cross diffusion and side reaction of species at LLZO/cathode interface. The primary goal is investigate the effect of transition metal impurities on LLZO.

The remainder is aimed at understanding the conductivity of the discharge products of metal-oxygen batteries. In general, alkali peroxides or superoxides are the major discharge products in non-aqueous alkali metal-oxygen batteries. Batteries that discharge to superoxide (NaO_2, KO_2) have low charging overpotentials, while batteries that discharge to peroxide (Na_2O_2, Li_2O_2) have high charging overpotentials. Nonetheless, even for batteries that discharge to peroxide, the superoxide (LiO_2, NaO_2) acts as redox mediator and can affect electron/ion transport. There are few experimental and computational studies regarding to the charge transport mechanisms in alkali peroxides and superoxides. The primary goal is to characterize the mechanisms for charge transport vial intrinsic defects in a range of alkali peroxides (Na_2O_2) and alkali superoxides (LiO_2, NaO_2, KO_2). Understanding these mechanisms will foster the development of strategies to improve the discharge capacity and round-trip efficiency in these

batteries.

A brief outline of this thesis is given below:

In chapter 2 we discuss the computational methodology. We start by introducing the fundamentals of Density Functional Theory and the different exchange correlation functionals employed: the local-density approximation (LDA), generalized gradient approximation (GGA), and hybrid functionals. Next, we introduce the quasi particle GW methods, and describe the defect formation and migration calculations. Last, we introduce the principles of classical molecular dynamics and the interatomic potentials used in those calculations.

Chapter 3 presents a comprehensive study of intrinsic conductivity in sodium-air battery discharge phases: sodium superoxide and sodium peroxide. Band gap calculations are presented using density functional and quasi-particle GW methods for the bulk phases. Hybrid functionals were to calculate defect formation energies in both compounds. The mobility of these defects was evaluated using the Nudged Elastic Band method.

Chapter 4 discusses the intrinsic conductivity in two other alkali superoxides recently-reported as discharge phases in metal-oxygen batteries: lithium superoxide and potassium superoxide. Here we discuss Jahn-Teller distortions in bulk the phase. Next, we propose a precession model for potassium superoxide. Hybrid functionals and GGA+U functionals to evaluate defect formation energies and mobilities in LiO_2 and KO_2. Comparisons of the electronic structure are made across the superoxide series: LiO_2, NaO_2, and KO_2.

Chapter 5 quantifies the impact of transition metal impurities on ionic transport in the solid electrolyte $Li_7La_3Zr_2O_{12}$. Classical molecular dynamics simulations were used to investigate the transport rates of Co and three other transition metals (Mn, Fe, and Ni) in Al-doped LLZO, and to predict how TM impurities impact Li-ion migration. Our calculations suggest that Fe impurities are the most mobile of the four TMs investigated; nevertheless, all TMs exhibit lower diffusivities in LLZO compared with Li. Furthermore, the presence of TMs is shown to slow Li-ion migration, with the relative magnitudes of the slowing following the same trend as the TM diffusivities.

Finally, Chapter 6 concludes this thesis with summary of our findings and a brief discussion of possible extensions.

Chapter 2: Methodology

2.1 Kohn-Sham Density Functional Theory

Many chemical phenomena at the atomic scale are well-described by the time-independent, non-relativistic Schrodinger equation:

$$H\Psi_i(\vec{x}_1,\vec{x}_2,\ldots,\vec{x}_N,\vec{R}_1,\vec{R}_2,\ldots,\vec{R}_M) = E_i\Psi_i(\vec{x}_1,\vec{x}_2,\ldots,\vec{x}_N,\vec{R}_1,\vec{R}_2,\ldots,\vec{R}_M) \tag{2.1}$$

Here H is the Hamilton operator for a molecular system consisting of *M* nuclei and *N* electrons in the absence of magnetic or electronic fields, Ψ is the many-body wavefunction, and *E* is the total energy of system. The Born-Oppenheimer approximation assumes the nuclei as static because the nuclei are at least 2000 times heavier than the electrons. Under this assumption, the many-body Hamiltonian can be decoupled into an electronic part and nuclear part:

$$\left[-\frac{\hbar^2}{2m}\sum_{i=1}^{N}\nabla_i^2 + \sum_{i=1}^{N}V\left(\vec{r}_i\right) + \sum_{i=1}^{N}\sum_{j<i}U\left(\vec{r}_i,\vec{r}_j\right)\right]\Psi = E\Psi \ . \tag{2.2}$$

Here, m is the electron mass. The three terms in brackets in this equation define the kinetic energy of the electrons, the interaction energy between each electron and the collection of atomic nuclei, and the interaction energy between different electrons, respectively. Although Born-Oppenheimer approximation reduces the degrees of freedom from *3N+3M* to *3N*, solving the Schrodinger equation is still infeasible in all but for smallest systems.

Instead of using the electronic wave function as an independent variable, Kohn-Sham Density Functional Theory (DFT) [88] adopts the charge density as the quantity with respect to which the electronic energy is to be minimized. The formal basis of DFT is the Hohenberg-Kohn (HK) theorems: [88] the first HK theorem states that the external potential $V_{ext}(\vec{r})$ is (to within a constant) a unique functional of the ground state charge density.[89] The second HK theorem states that the ground-state energy of a many-body system is a universal functional of the charge density, $E[n(\vec{r})]$, which will reside in a global minimum when the charge density is in its ground state $n_0(\vec{r})$.[90] The electron (charge) density $n_0(\vec{r})$ is the probability that the *N* electrons are at a particular set of coordinates, $\vec{r_1}, \vec{r_2}, ..., \vec{r_N}$, and it is defined with respect to the single-electron wavefunctions:

(2.3) $$n\left(\vec{r}\right) = 2\sum_i \psi_i^*\left(\vec{r}\right)\psi_i\left(\vec{r}\right) .$$

The density $n\left(\vec{r}\right)$ in this case is a much simpler quantity than Ψ because it only depends on three spatial coordinates (x, y, z).

Within the Kohn-Sham formalism, Equation 2.2 is expressed in the form of a system of fictitious non-interacting electrons. To do this, we introduce the exchange-correlation energy:

(2.4) $$E_{\mathrm{XC}}[n] = F[n] - T_0[n] - E_{\mathrm{H}}[n] ,$$

where

(2.5) $$E_H[n] = \frac{1}{2}\int \frac{n(\vec{r})n(\vec{r}')}{\left|\vec{r}-\vec{r}'\right|} d\vec{r}d\vec{r}'$$

is the Hartree energy, representing the classical electrostatic energy. Equation 2.4 can then be written as

(2.6) $$E_{HK}[n] = \int n(\vec{r}) v_{ext}(\vec{r}) d\vec{r} + E_H[n] + T_0[n] + E_{XC}[n]$$

Here, $T_0[n(r)]$, $V_{ext}(r)$, $E_{xc}[n(r)]$ represent the many-body kinetic energy, external ionic potential, and the exchange correlation energy, respectively. The kinetic energy can be expressed as

(2.7) $$T\{\Psi_i\} = \sum_{i=1}^{N} \frac{\hbar^2}{2m} \psi_i^* \nabla^2 \psi_i$$

The exchange-correlation energy E_{xc} contains all quantum-mechanical effects not included by the other terms in the energy functional, such as electron exchange and correlation.

Equation 2.6 can be solved by direct numerical minimization or through a self-consistent approach using a set of single-particle Schrodinger-like equations, with Lagrange multipliers to account for the orthonormality constraint. This yields the Kohn-Sham equation

(2.8) $$\left\{ \frac{\hbar^2}{2m} \nabla^2 + V_{ext}(\vec{r}) + V_H[n(\vec{r})] + V_{XC}[n(\vec{r})] \right\} \psi_i = \varepsilon_i \psi_i \ ,$$

where

(2.9) $$V_H[n(\vec{r})] = \frac{\delta E_H[n(\vec{r})]}{\delta n(\vec{r})} = \frac{1}{2} \int \frac{n(\vec{r}')}{|\vec{r} - \vec{r}'|} d\vec{r}'$$

(2.10) $$V_H[n(\vec{r})] = \frac{\delta E_{XC}[n(\vec{r})]}{\delta n(\vec{r})} \ ,$$

Equation 2.8 has the same form as the time-independent Schrödinger equation (Equation 2.2) for non-interacting electrons in an effective local potential

(2.11) $$V_{eff}(\vec{r}) = V_{ext}(\vec{r}) + V_H[n(\vec{r})] + V_{XC}[n(\vec{r})] .$$

The solution of the Kohn-Sham equation relies on making an approximation for the exchange-correlation functional $E_{XC}[n]$, as discussed in section 2.2. The related *GW* family of methods are discussed in section 2.3.

2.2 Exchange-correlation functionals

Local Density Approximation (LDA). The simplest method of exchange-correlation functionals is the local-density approximations (LDA). The LDA consists of locally approximating the true exchange-correlation energy of a system by the exchange-correlation energy associated with a homogeneous electron gas that has the same density. The LDA is only dependent on the local density, and the total energy is commonly written as:

(2.12) $$E_{\mathrm{xc}}^{\mathrm{LDA}}[n(\vec{r})] = \int n(\vec{r}) \varepsilon_{\mathrm{xc}}^{\mathrm{LDA}}[n(\vec{r})] \mathrm{d}^3\vec{r} \ .$$

Here $\varepsilon_{\mathrm{xc}}^{\mathrm{LDA}}[n(\vec{r})]$ is the exchange-correlation energy density per electron of a homogeneous electron gas (HEG) of density $n(\vec{r})$. The $\varepsilon_{XC}[n(\vec{r})]$ for HEG can be accurately solved using quantum Monte Carlo methods over a wide range of densities.[91]

The LDA can be thought of as an expansion of the exchange-correlation energy in the limit of a slowly varying density; thus, the degree of reliability of LDAs general depends on the homogeneity of the charge density.

Despite its simplicity, the LDA works well for solid systems where the change density is often slowly-varying in space. The main source of error in LDAs is usually an underestimate the exchange energy, so LDA has a tendency to overbind; this overbinding can be particularly severe for molecular systems.

Generalized Gradient Approximation. An improvement to the LDA can be made by also incorporating a dependence on the gradient of the density. These so-called generalized gradient approximations (GGAs) take the form

$$E_{XC}^{GGA}[n] = \int n(\vec{r})\varepsilon_{XC}^{GGA}(n(\vec{r}), \left|\vec{\nabla} n(\vec{r})\right|) d^3\vec{r} \,. \tag{2.13}$$

In GGAs, the presence of a gradient generally increases the exchange energy and relieves, to some degree, the overbinding of homogeneous systems relative to inhomogeneous ones in LDAs. GGAs, and more accurate functionals which include higher-order derivatives of the density (meta-GGAs), are collectively referred to as semi-local functionals; *i.e.*, the contribution to the exchange-correlation energy from each point in space depends only on the value and derivatives of the density at that point.

Although semilocal functionals give a better description of inhomogeneous systems (where the charge density can vary more rapidly in space), like transition metals and molecules, there are certain situations which are known to be poorly described by semilocal functionals. Some phenomena known to be particularly problematic are:

1. Van der Waals interactions[92]
2. Strongly correlated systems[93] (*e.g.*, transition metal compounds)
3. Delocalization errors[94,95] (*i.e.*, self-interaction error)

The asymptotic $1/r^6$ behavior in long-range dispersion interactions cannot be captured by the local and semilocal functionals. Recently, Van der Waals interactions have been included in several density functionals.[96–101] Strongly correlated systems often refer to transition metal materials where incompletely filled d- or f- electrons result in strong electron-electron interaction. Delocalization errors refers to the tendency of semilocal functionals to favor fractional charges or delocalized charge distributions over integral occupancies or localized ones, and is a consequence of the fact that the exchange-correlation energy of semilocal functionals is generally a convex function of electron occupancy.[94,95,102] This issue can be compensated for by employing orbital-dependent methods, such as DFT+*U*, hybrid functionals (discussed below), and *GW* calculations.

Hybrid functionals. Some of the errors of GGAs can be mitigated through the incorporation of a portion of exact exchange from Hartree-Fock theory. The exact exchange energy functional is expressed in terms of the Kohn-Sham orbitals rather than the density. For example, the HSE (Heyd-Scuseria-Ernzerhof) functional uses an error function screened Coulomb potential to calculate the exchange portion of the energy. [103,104]

$$E_{xc}^{HSE} = a E_x^{SR}(\mu) + (1-a) E_x^{PBE,\,SR} + E_x^{PBE,\,LR}(\mu) + E_c^{PBE}. \tag{2.14}$$

Here E_x^{SR} is the short-range exact exchange energy, $E_x^{PBE,\,SR}$ and $E_x^{PBE,\,LR}$ are the short- and long-range contributions to exchange energy from the PBE GGA functional,[105] and E_c^{PBE} is the PBE correlation energy. There are two parameters: a screening parameter μ controlling the length scale for separating short- and long-range interactions, and the mixing parameter a governing the fraction of short-range Hartree-Fock exact exchange incorporated.

A value for the screening parameter of $\mu = 0.207 \text{Å}^{-1}$ (0.11 bohr^{-1}) and the mixing parameter $a = 0.25$ have been found to give a good description of solids properties such as enthalpies of formation, ionization potentials, and lattice constants.[103,104,11] However, in many cases setting $a = 0.25$ does not yield an accurate description of defect states and band edge

energies. In order to correctly describe defect states, one must have a correct description of delocalized electrons and hence the band edge positions. Semilocal density functionals can yield over-delocalized electron densities resulting in inaccurate defect geometries. Hybrid functionals generally improve upon this. One approach is to adjust the mixing parameter to reproduce the experimental gap of the material.[106–108]

For most of the calculations in this work, we employ a modified form of the HSE functional with a mixing parameter of $\alpha = 0.48$ inherited from our previous calculations on Li_2O_2.[55] While there has been no experimental measurement of the bandgap for alkali peroxides and alkali superoxides, accurate bandgaps can be calculated using higher accuracy theoretical schemes such as many-body perturbation based on the GW approximation. For the case of bulk Li_2O_2, the mixing parameter α was fitted to the average of the GGA + G_0W_0 and GGA + scGW band gaps (calculated at the $\alpha = 0.25$ geometry); this choice is motivated by the fact that GGA + G_0W_0 is known to underestimate gaps, while GGA + scGW (in the absence of vertex corrections) overestimates gaps.[109,110]

2.3 GW methods

The *fundamental gap* of insulators and semiconductors is the energy difference between the top of the valence band and the bottom of conduction band, and can be expressed as:

$$\Delta_{fundamental} = E(N+1) + E(N-1) - 2E(N), \tag{2.15}$$

where *E(N)* is the ground state energy of the system with *N* electrons. This expression can be interpreted as follows: we start with two neutral systems, and move an electron from one system to the other.

DFT in principle is an exact theory for ground-state properties, such as the total energy and atomic structure, but it is not intended to address excited state properties, such as band

structure and optical excitation energies. The gap calculated from DFT is called the *Kohn-Sham gap,* referring to the difference between the eigenvalues of the lowest unoccupied and highest unoccupied Kohn-Sham orbitals.

The Kohn-Sham gaps are in general much smaller than the fundamental gap. In some cases, such as crystalline germanium, semilocal functionals predict semiconductors to have no Kohn-Sham gaps.[93] When an electron is added to a system of interacting electrons, it interacts with surrounding electrons via the screened Coulomb interaction. The combination of the electron and the cloud of the disturbed neighboring electrons behave effectively like a new particle with renormalized properties called a quasiparticle. A solution to this problem is achieved with many-body perturbation theory in the GW approximation. Underlying the *GW* method is the quasiparticle equation,[111,112]

$$\left\{\frac{\hbar^2}{2m}\nabla^2 + V_{ext}(\vec{r}) + V_H[n(\vec{r})] + \int \Sigma(\vec{r},\vec{r}';\varepsilon_i)d\vec{r}'\right\}\psi_i = \varepsilon_i\psi_i\,, \tag{2.16}$$

where $\Sigma(\vec{r},\vec{r}';\varepsilon_i)$ is the self-energy operator. The eigenvalues of the quasiparticle equation physically represent energies for electron addition or removal, and hence the fundamental gap can be computed as a difference in quasiparticle energies.

The quasiparticle equation is generally solved by using a suitable approximation for $\Sigma(\vec{r},\vec{r}';\varepsilon_i)$. The *GW* approximation extends the well-known Hartree-Fock approximation for the self-energy, by replacing the Coulomb potential by a dynamically screened potential *W* and single-particle Green function *G*:[111]

$$\Sigma(\vec{r},\vec{r}';\varepsilon_i) \approx iG(\vec{r},\vec{r}';\varepsilon_i)W(\vec{r},\vec{r}';\varepsilon_i)\,. \tag{2.17}$$

G and *W* can be expressed in terms of the quasiparticle wavefunctions. In the simplest approach (G_0W_0), the eigenvalues of the Green's function *G* and screened potential *W* can be calculated non-selfconsistently from the DFT wavefunctions and eigenvalues, and the self-energy operator is considered as a perturbation to the Kohn-Sham potential. There exist several flavors of GW methods, with eigenvalues of G and W of the quasiparticle are updated in different fashions (separately/fixed). Following the notation of the Vienna *ab initio* Software Package,[113] several possible strategies are summarized in Table 2.1.

Table 1.2 Summary of GW methods.

Name	**Meaning**
G_0W_0 ("single-shot" *GW*)	Neither *G* nor *W* is updated.[113]
GW_0	Eigenvalues are used to update *G*.[109,114]
GW	Eigenvalues are used to update *G* and *W*.[109,114]
sc*GW*/QPsc*GW*	Eigenvalues and wavefunctions are used to update *G* and *W*.[110]

2.4 Implementation

Throughout this thesis, first principles calculations were performed using the Vienna *ab initio* simulation package (VASP).[115–118] Projector-augmented wave (PAW) pseudopotentials were employed,[119] with a plane wave basis set with a 460 eV cutoff for fixed-volume calculations and a 700 eV cutoff for relaxed-volume calculations. The Brillouin zone was sampled with Monkhorst-Pack grids.[120] Ball-and-stick models were generated using VESTA.[121]

2.5 Point Defects

2.5.1 Thermodynamics

Point defects are known to play a significant role in many import solid-state phenomenon, including mass transport, charge transport, and nucleation.[122–124] In this section we discuss the statistical physics of point defects in solids. The principle goal is to relate macroscopic quantities (equilibrium concentrations and diffusion coefficients) to microscopic quantities that can be calculated from atomistic simulations.

We use a notation X_s^q to represent a defect, where X is the identity of the defect or impurity, q is the charge state, S is the site. Here are some examples of commonly used defects notations: V_{Na}^- represents a negative sodium vacancy; Na_i^+ represents positive sodium interstitial; h_p^+ represents hole polaron.

Like all things in life, point defects are a balance between energy and entropy. The equilibrium defect concentration reflects a balance between the entropy gain associated with imperfections in the crystal lattice and the energy cost of introducing those imperfections. At equilibrium and in the dilute limit, the concentration of a point defect X_s^q in a crystal can be expressed in terms of its formation energy:

$$C = N_{sites} \exp(-\frac{E_f}{k_B T}), \tag{2.18}$$

Here the formation energy E_f is the amount of free energy required to create a single defect of type *k*. In general, we calculate formation energies as

$$E_f\left(X_s^q\right) = E_0\left(X_s^q\right) - E_0\left(pristine\right) - \sum_i n_i \mu_i + q\left(\varepsilon_F + \Delta V\right) + E_{MPI}\,. \tag{2.19}$$

Here $E_0\left(X_s^q\right)$ and $E_0\left(pristine\right)$ are the ground state DFT energies of supercells with and without a defect, respectively. The third term accounts for the addition/removal of atoms; n_i is the number of atoms of species i that have been removed ($n_i < 0$) or added to ($n_i > 0$), and μ_i is the chemical potential of species i. This term will be zero for polarons since we don't remove or add any atoms from the supercell. The fourth term accounts for the addition/removal of electrons; q is the equivalent charge associated with the defect, ΔV is the potential alignment term between defects supercell and pristine supercell and ε_F is the Fermi level (i.e., the chemical potential of electrons) referenced to the valence-band maximum (VBM) in the bulk. The final term E_{MPI} represents a finite-size correction, in order to accelerate convergence of the formation energy with respect to supercell size. A number of finite-size corrections have been proposed.[125–127] In this work, we employ the Makov-Payne monopole correction[125] since this is the leading error among the finite-size corrections. For the charged systems, the correction is given by the quadratic electrostatic potential

$$\frac{e^2 q^2 \alpha}{L\varepsilon}, \tag{2.20}$$

where q is the net charge of the system, α the Madelung constant of a point charge, ε the dielectric constant of the system.

The chemical potentials of the species reflect the reservoirs for atoms that are involved in creating the defects. Ultimately, the experimental conditions under which the defects are created uniquely define the relevant reservoirs. The Fermi level (chemical potential of electrons) is not the Fermi energy of the DFT calculations. The latter is adjusted to maintain the total electron number in the defect supercell calculation when Kohn-Sham states are occupied. If the size of the system is sufficiently large for any electric fields to be screened by mobile defects, then the Fermi level will be determined by the condition of charge neutrality:

(2.21) $$\sum_{X,q,s} qC\left(X_s^q\right) + n_e + n_h = 0 .$$

Therefore, ε_F can be found by standard root-finding algorithms with the combined set of defects X_s^q, free holes n_h and free electrons n_e.

Although most of our calculations are in the solid state, we must consider gaseous O_2. All the defects formation energy calculations are related with the discharge product in metal-air batteries, where the compounds are in equilibrium with the oxygen in the air or tank. Therefore, we assume the chemical potential of oxygen to be one half the free energy of gaseous O_2 at 300 K and 0.1 MPa.

(2.22) $$G_{O_2} = E_{O_2}^{DFT,corr} + k_B T - TS_{O_2}^{expt} .$$

where the $k_B T$ term accounts for the pV contribution to free energy, and $S_{O_2}^{expt}$ is the experimental entropy.[128] We have intentionally neglected the small contributions to the free energy due to the translational, rotational, and vibrational degrees of freedom because we are not including these terms in the bulk phases; this maintains some degree of error cancellation.

$E_{O_2}^{DFT,corr}$ represents the corrected ground state energy of the O_2 molecule. Because DFT systematically overbinds gas-phase O_2, which in turn leads to large errors in the calculated formation energies of oxides (O^{2-}), peroxides (O_2^{2-}) and superoxides (O^{2-}),[129–131] we calculated and applied correct the ground state energy of the O_2 molecule using the experimental formation enthalpy of peroxides and superoxides. The correction is different for oxides, peroxides, and superoxides. For Na_2O_2 defect calculations, we apply a correction to the energy of O_2 based on the experimental formation enthalpy of Na_2O_2 at 300 K; For LiO_2, NaO_2 and KO_2 defect calculations, we apply an average correction based on the formation enthalpy of LiO_2, NaO_2 and KO_2. For a solid with formula M_xO_y, where M is the alkali metal, the correction can be calculated using:

(2.23) $$E_0^{DFT,correction}(O_2) = \frac{2}{y}[E_0^{DFT}(M_xO_y) - xE_0^{DFT}(M) - \Delta H_f(M_xO_y)].$$

This increases the energy of O_2 molecule by 0.62, and 0.10 eV for the HSE_α ($\alpha = 0.48$) functional for peroxides and superoxides. We note that prior studies have found that the error in formation energy varies to some degree between different alkali and alkaline-earth metal oxides, peroxides, and superoxides.[131] This indicates that in addition to errors in the ground state energy of the O_2 molecule, there is some error associated with the solid phases. However, we note that our results are not greatly sensitive to the choice of correction: for example, A 0.1 eV change in the O_2 correction changes the polaron formation energy by only 0.025eV in Na_2O_2 and 0.05 eV in MO_2 (M = Li, Na, K).

2.5.2 Kinetics

One of the main goals of this work is to connect microscopic simulations to macroscopic properties, i.e. transport phenomena. The conductivity associated with a given defect depends upon its concentration and mobility. Defect mobilities, μ, are calculated using the Nernst-Einstein equation,

(2.24) $$D = \mu k_B T / e.$$

Here, D is the diffusion coefficient. There are several ways to estimate the diffusion coefficient. At atomistic scale, Transition State theory and Molecular Dynamics allows us to estimate defect mobilities in terms of microscopic quantities. In the case of isotropic media, the mobility can be expressed as[123]

(2.25) $$D_k = \gamma a^2 \nu \exp\left(-E_a / k_B T\right).$$

Where γ is a geometric factor relating to the lattice, v is the hopping attempt frequency, a is the jump distance and E_a is the defect diffusion barriers. The hopping attempt frequency, representing vibrational frequencies of the atoms in the potential minimum, can be computed from the vibrational spectra of the transition state.[132] The most important feature of this rate is that it changes by orders of magnitude as the temperature is changed over a small range. However, the fractional variation in v from system to system is generally small compared to the variation in the exponential term; thus the attempt rate is often assumed to be ~10^{13} Hz.[123,132]

The activation energy is the energy barrier along the minimum energy path (MEP). Standard geometry optimization algorithms are not helpful for finding the transition state, as the potential energy maximum along the MEP is a saddle point. Nudged elastic band (NEB) method[133] can be employed for finding the transition state energy.

Another way to calculate diffusion coefficient is through Molecular Dynamics. In statistical mechanics, the Mean Squared Displacement (MSD) can be calculated according to the deviation of the positions of the ions at each time-step relative to a reference position. The standard definition of MSD is

$$\left\langle \left| \delta \vec{r}_i(t) \right|^2 \right\rangle = \frac{1}{N} \sum_{i=1}^{N} \left\langle \left| \vec{r}_i(t) - \vec{r}_i(0) \right|^2 \right\rangle . \tag{2.26}$$

where N is the total number of atoms, $\vec{r}_i(t)$ is the displacement of the i-th ion at time t, and the bracket represents averaging over t. A linear fit performed during the equilibrium process can be used to extract self-diffusivity as

$$D = \frac{1}{6} \lim_{t \to \infty} \frac{\left\langle \left| \delta \vec{r}_i(t) \right|^2 \right\rangle}{t} . \tag{2.27}$$

Furthermore, the conductivity arising from charged defects (polarons or ions) depends on both the concentrations and mobilities of these carriers, and may be expressed as:

(2.28) $$\sigma = eC\mu .$$

2.6 Molecular dynamics

2.6.1 Principles of Molecular dynamics

Molecular dynamics (MD) is a simulation technique in which the time evolution of a set of interacting atoms can be followed by integrating their equations of motion. In MD, all physical quantities are calculated from sets of coordinates that are obtained by advancing "particles", that make up the system, over time. These time trajectories are obtained by solving Newton's classical equation of motion,

(2.29) $$F_i = m_i a_i .$$

Equation 2.29 is followed for each atom i in a system with N atoms. The net force acting on each particle is obtained at a given time, and will be calculated before the next movement of the particle. The smaller the time difference between the force calculations, the more accurate the simulation will be. However, if the time steps are too small, the simulation can be unnecessary slow. Newton's equation solved for N particles in a system with potential U has the following form:

(2.30) $$m_i a_i = -\nabla U_i(r) .$$

When solving the equations of motion, one commonly used method is the finite difference approach. The are several different integration alogrithms discussed in the literature, with the velocity Verlet alogorithm being one of the most efficient and popular.[134] The equation form of the velocity Verlet integration scheme is

$$x(t+\Delta t) = x(t) + \Delta t v(t) + \frac{(\Delta t)^2}{2m} F(t) . \tag{2.31}$$

$$v(t+\Delta t) = v(t) + \frac{\Delta t}{2m}\left[F\left(t\right) + F\left(t+\Delta t\right)\right] . \tag{2.32}$$

Here, positions and velocities are obtained at the next time step $t+\Delta t$ based on the values at the current time step t. The simulation is always started with initial positions and velocites given. For example, the initial positions of particles may be given by a structure and velocies can be randomly assigned from a normal distribution.

MD simulations are generally be performed in different thermodynamic ensembles, where combinations of three of the following parameters are held constant: pressure P, temeperature T, number of particles N, density ρ and volume V. For example, by keeping N, V and E constant, usually written as NVE, one obtains the microcanonical ensemble, corresponding to an isolated system with constant energy. Which ensemble is used depends on the problem or system one is interested in. The simulations performed in this thesis employ NVT (isothermal, canonical) and NPT (isobaric, isothermal) ensembles.

2.6.2 Molecular Dynamics Potentials

The integration of Newton's 2nd Law requires the specification of a suitable interaction potential between atoms. One such interatomic potential is the empirical bond valence (BV) method, which has been successfully used to predict of ionic conductivity in oxides and glasses.[135,136] It

expresses the concept that the bond length and bond valence (oxidation state) are related, and has provided insight into the link between structure and ion transport in solids. The variation of an individual bond valence can be straightforwardly translated into the variation of a Morse-type interaction potential

$$E = D_0 \left\{ \left(\exp\left[\alpha (R_{\min} - R) \right] - 1 \right)^2 - 1 \right\}. \tag{2.33}$$

with $b = 1/\alpha$. Adams *et al.* derived soft BV parameters for 132 cation types in oxides.[137] The total bond valence site energy BVSE (A) of a cation A can be determined as the sum over bond valence terms for the interactions with each of the N_X adjacent anions plus the Coulomb repulsion term. The Coulomb repulsion term runs over all N_A cations, where the fractional charges q_A, q_X are calculated based on

$$q_A = \frac{V_{id}(A_i)}{\sqrt{n_{Ai}}} \sqrt{\frac{\sum_j \frac{V_{id}(X_j) N_{Xj}}{\sqrt{n_{Xj}}}}{\sum_i \frac{V_{id}(A_i) N_{Ai}}{\sqrt{n_{Ai}}}}}. \tag{2.34}$$

$$q_{Xj} = \frac{V_{id}(X_j)}{\sqrt{n_{Xj}}} \sqrt{\frac{\sum_i \frac{V_{id}(A_i) N_{Ai}}{\sqrt{n_{Ai}}}}{\sum_j \frac{V_{id}(X_j) N_{Xj}}{\sqrt{n_{Xj}}}}}. \tag{2.35}$$

in which N_{Xi}, (N_{Aj}) refer to the occupancies of the ith anion X_i (jth cation A_j in the structure model), n_A, n_X represent the principal quantum numbers of cation A and anion X and $V_{id}(A)$, $V_{id}(X)$ the absolute value of their respective nominal charges. This scaling of fractional charges ensures that the structure is overall charge neutral. The Coulomb repulsions between two different cations A_1 and A_2 cations are then take the form:

$$(2.36)\quad E = q_i q_j \left[\begin{array}{l} \dfrac{1}{R_{A1-A2}} erfc\left(\dfrac{R_{A1-A2}}{\rho_{A1-A2}}\right) - \dfrac{1}{R_c} erfc\left(\dfrac{R_c}{\rho_{A1-A2}}\right) + \\ \left(\dfrac{1}{R_c^{\,2}} erfc\left(\dfrac{R_c}{\rho_{A1-A2}}\right) + \dfrac{2}{\sqrt{\pi} R_c \rho_{A1-A2}} \left(\exp\left(\dfrac{R_c}{\rho_{A1-A2}}\right)\right)^2\right)\left(R_{A1-A2} - R_c\right) \end{array} \right].$$

where R_c is the cutoff distance, $\rho_{A1-A2} = (r_{A1} + r_{A2})\, f$ is assumed to equal the sum of the covalent radii r_{Ai} of the two ions times a factor of f that depends on the average absolute cation electronegativity and the average cation charge in the compound. In this chapter, All classical molecular dynamics simulations were carried out using the LAMMPS package[138] with the Morse potential describe in this section.

Chapter 3: Intrinsic Defect Conductivity in Na-O_2 Battery Discharge Phases: Na_2O_2 vs. NaO_2

3.1 Introduction

As we discussed in Section 1.5, for Na-O_2 cells employing non-aqueous electrolytes, some studies have reported Na_2O_2 as the main discharge product,[76] while others report NaO_2.[68,75] Cells that discharge to Na_2O_2 exhibit high charging overpotentials, similar to those observed in Li-O_2 batteries. On the other hand, cells that discharge to NaO_2 have much lower charging overpotentials, typically less than 200 meV. [68,75,78] In this chapter, we identify which property of the superoxide phase is responsible for its low OER overpotential.[78,80,82,84] One possibility is that this behavior arises from a higher conductivity relative to the peroxide. Along these lines, Hartmann *et al.*[80] and Zhao *et al.*[78] argued that the large particle sizes typical of the NaO_2 phase observed in discharged Na-O_2 cells implied a higher conductivity. This would be consistent with an early report that found moderate conductivity in KO_2 (approximately 1-10 S/cm).[85] More recent experiments measured the total (electronic + ionic) conductivity of KO_2 at elevated temperatures (345 to 500 K). Extrapolating these data to 300 K yields a much lower value of 10^{-13} S/cm.[86,139] While the popularity of Li-O_2 batteries has recently sparked interest in the properties of Li_2O_2,[55,140,141] transport in superoxide phases has received less attention.[85,86,139] In the case of Li_2O_2, a small number of studies have predicted that both holes and electrons become self-trapped on oxygen dimers, forming small hole/electron polarons.[54,55,140–142] DFT+U calculations by Garcia *et al.* revealed that hole polarons have a much higher mobility than do electron polarons in Li_2O_2.[140] Radin *et al.* used a tuned hybrid functional to estimate the intrinsic conductivity of Li_2O_2 by combining the calculated concentrations of various charge-carrying point defects with their respective mobilities.[55] They identified hole polarons and negative lithium vacancies as the dominant charge carriers; the low concentrations and limited mobility of these species result in the low conductivity of Li_2O_2. This result was corroborated by

experiments,[143] which found the same charge-carrying species in bulk Li_2O_2. To our knowledge much less effort has been devoted to examining intrinsic conductivity in the Na-O system.[86,144]

In this chapter, first-principles calculations are used to predict the intrinsic conductivities of bulk Na_2O_2 and NaO_2. More specifically, the formation energies and concentrations of various charge carrying point defects with different charge states – polarons, vacancies, and interstitials – are evaluated. Subsequent calculations assess the mobilities of the highest-concentration charge carriers. Many-body perturbation theory (GW) reveals that both Na_2O_2 and NaO_2 are wide gap insulators with bandgaps of 6.65 and 5.30 eV, respectively. Similar to earlier studies on Li_2O_2,[55,141] hole polarons (localized on O_2 dimers) and negative sodium vacancies are identified as the main charge carriers in Na_2O_2. Combining the concentration and mobility data, we find that the electronic and ionic conductivity of Na_2O_2 is essentially the same as that for Li_2O_2.

Transport phenomena are more complex in case of the superoxide. Regarding electronic transport, our calculations predict that both electron and hole polarons contribute to the intrinsic conductivity of NaO_2 in roughly equal proportion. Although electron polarons are present in higher concentrations compared to holes, the trend in mobilities is reversed, with holes having lower hopping barriers. Ionic conductivity in NaO_2 is mediated by a mixture of negative sodium vacancies and positive oxygen dimer vacancies. Combining concentration and mobility data, our calculations find that the electronic conductivity of NaO_2 is only slightly higher than in the peroxide, and remains low in an absolute sense. This behavior differs markedly from the ionic conductivity, which is approximately 10 orders of magnitude higher in NaO_2 than in the peroxide.

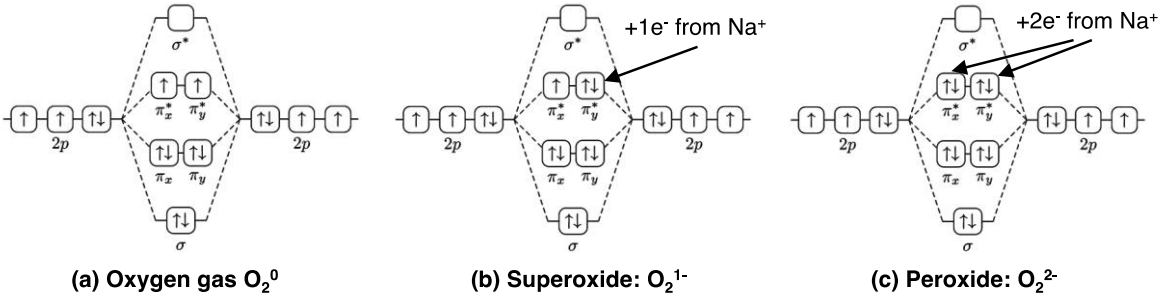

Figure 1.6 Molecular Orbital (MO) diagrams for: (a) oxygen (O_2^0), (b) superoxide (O_2^{1-}) and, (c) peroxide (O_2^{2-}) dimers.

These data reveal that long-range electronic transport in alkali peroxides and superoxides is governed by the unusual ability of oxygen dimers to adopt three distinct charge states: O_2^{2-}, O_2^{1-}, and O_2^{0}, Figure 3.1 More importantly, the modest electronic conductivity afforded by the superoxide suggests that enhanced bulk transport through this phase is unlikely to account for the low overpotentials associated with its decomposition. We therefore speculate that the improved performance of NaO_2-based cells arises from a reduction in the extent of side reactions, such as electrolyte decomposition.[68]

3.2 Methodology

Density functional theory (DFT) calculations were performed with the Vienna ab initio Simulation Package (VASP).[116–118,145] A Γ-centered K-point grid with density 4×4×6 (6×6×6) for Na_2O_2 (NaO_2) was used for calculations involving primitive cells. A 144 atom supercell generated from a 2×2×3 replication of the unit cell was used for defect calculations on Na_2O_2; a 2×2×2 supercell (96-atoms) was used for NaO_2. The Γ point was used for defect calculations involving supercells. All calculations were spin-polarized and used a planewave cutoff energy of 460 eV. For structure optimizations, all ions were relaxed to a force tolerance of 0.02 eV/Å or less. A ferromagnetic configuration was employed for NaO_2 ($Pa\bar{3}$) bulk calculations. We found this configuration to 15 meV/formula unit more stable than an anti-ferromagnetic state with spins that alternate on [002] planes. The magnetic state obtained from supercell calculations involving NaO_2 was observed to be consistent with that of the superoxide unit cell.

Given that semi-local functionals may poorly describe some aspects of alkali-metal superoxides and peroxides,[146,147] our calculations employ hybrid functionals based on the HSE formulation[103,104] and many-body perturbation (GW) methods,[114] in addition to the PBE generalized gradient approximation (PBE-GGA).[148] As discussed in Section 2.2, we adopt the mixing parameter $\alpha = 0.48$ in the present study.

Density functional perturbation theory, in combination with the HSE06 functional, was used to calculate the relaxed-ion static dielectric constants. The dielectric constants are needed as input to the monopole correction method. For Na_2O_2 our calculations yield values of $\varepsilon = 4.5$ within the basal plane, and $\varepsilon = 6.6$ along the c direction. In the case of NaO_2, the diagonal elements of the static dielectric matrix were evaluated using the low-temperature marcasite phase, as the higher-temperature pyrite phase exhibits imaginary modes in its phonon spectrum. Calculated values are: ε_{xx}=5.0, ε_{yy}=4.6 and ε_{zz}=3.8. Given the modest anisotropy in the dielectric constants in both phases, we adopt values of $\varepsilon = 5.2$ for Na_2O_2 and $\varepsilon = 4.5$ for NaO_2.

3.3 Results and Discussion

3.3.1 Structure and Bandgaps.

Na_2O_2 is reported to adopt an hexagonal crystal structure (space group $P\bar{6}2m$) with lattice constants a = 6.21 and c = 4.47 Å.[149] The calculated lattice parameters are a = 6.11 and c = 4.42 Å (HSE06), in satisfactory agreement with the experimental values. Sodium cations in the peroxide structure reside in distorted trigonal prism sites, with oxygen forming the prism vertices (Figure 3.2a). Na_2O_2 units exhibit an …ABAB… stacking sequence along the c axis: each layer has the same density of Na atoms; however, the oxygen density exhibits a higher value in 'A' layers ('oxygen rich' layer, with an O-O bond length of 1.49 Å) than in 'B' layers ('oxygen poor' layer, with O-O bond length of 1.48 Å).

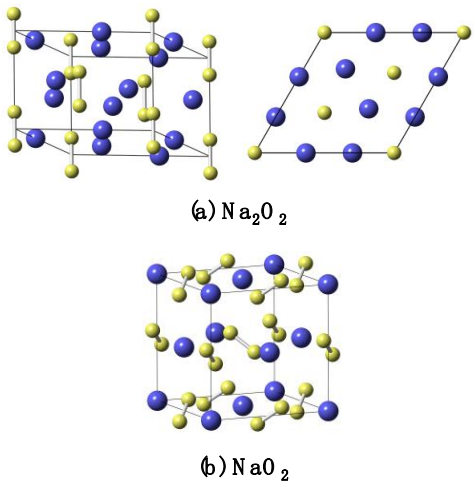

Figure 1.7 Crystal structures of (a) hexagonal Na_2O_2 viewed along two directions, and (b) cubic (pyrite) NaO_2. Yellow spheres represent oxygen atoms; blue spheres are sodium atoms.

The NaO_2 phase exhibits several polymorphs.[150] The stable structure below 196 K is tetragonal (space group $Pnnm$); from 196 K to 223 K the $Pa\bar{3}$ (NaCl rock salt structure type) is the stable phase, wherein the centroids of O_2^{2-} dimers occupy the Cl^- positions. The $Pa\bar{3}$ unit cell contains four oxygen dimers, each of which are aligned along different <111> directions. The calculated lattice parameter of the $Pa\bar{3}$ phase is a = 5.42 Å (HSE06), and is in good agreement with the experimental value of 5.46 Å.[151] Above 223 K, the O_2^{2-} dimers remain oriented along

<111> directions, but in a disordered fashion,[152] and the crystal structure adopts an FCC structure (a = 5.49 Å, space group $Fm3\bar{m}$). Given the difficulties associated with simulating a disordered structure, here we have adopted the ordered $Pa\bar{3}$ structure (Figure 3.2b) for our calculations. This choice is motivated both by the insensitivity of polaron and O_2 dimer migration barriers to dimer orientation (Figure 3.10), and by our earlier study which showed that the electrical conductivity of amorphous Li_2O_2 was not markedly improved compared to crystalline Li_2O_2.[153]

Table 1.3 Calculated bandgaps for Na_2O_2 and NaO_2 at different levels of theory. In the case of NaO_2, values are reported for both the low temperature (Marcasite, *Pnnm*) and intermediate temperature (Pyrite, $Pa\bar{3}$) phases.

	Method	Na_2O_2	NaO_2 ($Pnnm$)	NaO_2 ($Pa\bar{3}$)
Present Study	GGA	1.76	0	0
	HSE06	4.02	2.04	2.06
	HSE+G_0W_0	6.65	5.56	5.30
Previous Calculations	B3LYP	4.59 [188]	3.30 [188]	-
	HSE06	2.94 [82]	1.11 [82]	1.09 [82]

Table 3.1 summarizes the calculated bandgaps for Na_2O_2 and NaO_2 as a function of the level of theory. In the case of the GGA, a modest bandgap of 1.76 eV is predicted for Na_2O_2, while NaO_2 is predicted to have no gap (i.e., half-metallic behavior based on the density of states (not shown)). In contrast, use of the HSE06 hybrid functional results in the opening of a gap of 4.19 eV for Na_2O_2 and 2.06 eV for NaO_2. The bandgap for Na_2O_2 is similar to that previously reported for Li_2O_2.[54,154] Nevertheless, for both compounds the HSE06 gap is somewhat larger than those reported by Lee *et al.*[82] Comparison calculations were also performed on the tetragonal and rock salt structure variants for NaO_2; the data reveal that the bandgap is not very sensitive to the structure type. Non-self-consistent G_0W_0 calculations were performed using wave functions generated by self-consistent HSE06 calculations. Convergence tests were performed with respect to the number of electron states included in the calculation; 512 bands

were used for all G_0W_0 calculations. Quasi-particle GW methods have been shown to yield reliable estimates for bandgaps across many different materials.[109] The HSE+G_0W_0 data indicates that both Na_2O_2 and NaO_2 are wide band gap insulators, with band gaps of 6.65 and 5.30 eV, respectively. We believe the G_0W_0 calculations provide the best estimate of the true bandgaps of these compounds.

3.3.2 Intrinsic Defects in Na_2O_2.

Figure 3.3 shows the calculated formation energies for O vacancies (V_O), O_2 vacancies (V_{O2}, in which an entire O_2 molecule is removed), Na vacancies (V_{Na}), Na interstitials (Na_i), electron polarons (e_p^-) and hole polarons (h_p^+) as a function of the Fermi level in Na_2O_2 (Figure 3.3). The slope of each line in Figure 3.3 indicates the charge state for the respective defect species: a positive (negative) slope indicates a positively (negatively) charged defect, while a slope of zero indicates a neutral species. Kinks in the curves indicate transitions between charge states; only segments corresponding to the lowest energy charge states are shown. The zero of the Fermi level corresponds to the valence band maximum (VBM), and the vertical dashed line represents the position of the Fermi level that satisfies charge neutrality.[155]

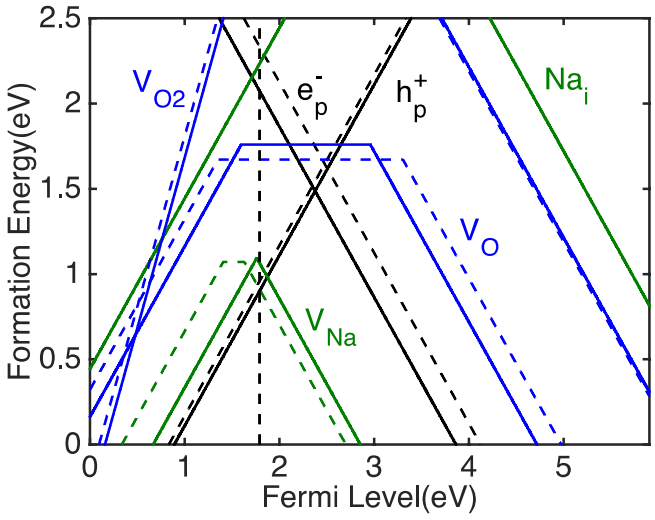

Figure 1.8 Defect formation energy of the O vacancy (red lines), Na vacancy (green lines), electron polarons and hole polarons (black lines) obtained using the HSE_α ($\alpha = 0.48$) hybrid functional in Na_2O_2. There are two symmetry inequivalent oxygen and sodium. The solid line represents the oxygen or sodium defects in oxygen-rich layer, while the dashed line represents the oxygen or sodium defects in oxygen-poor layer.

Table 1.4 Defect formation energies E_f (eV) and concentrations C (cm^{-3}) in Na_2O_2

Defect Type	E_f (eV)	C (cm^{-3})	Defect Type	E_f (eV)	C (cm^{-3})
h_{p1}^{+}	0.90	1×10^{7}	V_{O1}^{+}	1.95	5×10^{-11}
h_{p2}^{+}	0.96	6×10^{5}	V_{O1}^{0}	1.76	9×10^{-8}
e_{p1}^{-}	2.07	2×10^{-13}	V_{O1}^{-}	2.93	2×10^{-27}
e_{p2}^{-}	2.33	5×10^{-18}	V_{O2}^{+}	2.11	5×10^{-14}
V_{Na1}^{+}	1.12	3×10^{3}	V_{O2}^{0}	1.67	1×10^{-6}
V_{Na1}^{0}	1.09	1×10^{4}	V_{O2}^{-}	3.18	6×10^{-32}
V_{Na1}^{-}	1.06	3×10^{4}	$V_{O_2^1}^{2+}$	3.27	2.5×10^{-33}
V_{Na2}^{+}	1.46	8×10^{-3}	$V_{O_2^1}^{1+}$	4.29	2×10^{-50}
V_{Na2}^{0}	1.07	2×10^{4}	$V_{O_2^1}^{0}$	6.21	9×10^{-83}
V_{Na2}^{-}	0.91	1×10^{7}	$V_{O_2^1}^{1-}$	8.15	3×10^{-115}
Na_i^{+}	2.24	1×10^{-15}	$V_{O_2^2}^{2+}$	3.40	1×10^{-35}
Na_i^{0}	3.46	4×10^{-36}	$V_{O_2^2}^{1+}$	4.34	1×10^{-51}
Na_i^{-}	4.93	9×10^{-61}	$V_{O_2^2}^{0}$	6.19	1×10^{-82}
			$V_{O_2^2}^{1-}$	7.87	7×10^{-111}

As shown in Figure 3.3, the dominant charged defects in Na_2O_2 are negative sodium vacancies (V_{Na2}^{-}), and hole polarons (h_{p1}^{+}) localized on oxygen dimers, with formation energies of 0.91 and 0.90 eV, respectively. (Negative sodium vacancies can occupy two symmetry-distinct Na sites: V_{Na1}^{-} and V_{Na2}^{-}. V_{Na1}^{-} refers to a vacancy in the oxygen rich layer, while V_{Na2}^{-} occupies a Na site in the oxygen poor layer. We find that V_{Na1}^{-} is 0.15eV more stable than V_{Na2}^{-}. Similarly, h_{p1}^{+} represents a hole polaron in the oxygen rich layer, while h_{p2}^{+} represents a hole polaron in the oxygen poor layer; we find h_{p1}^{+} to be 0.06 eV more stable than h_{p2}^{+}.) This behavior is similar to what has been reported in Li_2O_2,[55] wherein the dominant charge-carrying defects

were identified as negative lithium vacancies (V_{Li}^{-}) and hole polarons with formation energies of 0.95 eV. The defects having the next-lowest formation energies are neutral oxygen vacancies (V_O, $E_f > 1.5$ eV) and electron polarons (e_p^-, $E_f > 2$ eV). Using the calculated formation energies as input to Equation 2.28, the equilibrium concentrations of h_p^+ and V_{Na2}^- are estimated to be 1×10^7 cm^{-3}, which are in reasonable agreement with those of Araujo *et al*., 2×10^8 cm^{-3},[144] whose calculations employed a slightly different value for the mixing parameter, α. As expected, our predicted concentrations are very similar to those for V_{Li}^- and h_p^+ reported in our previous calculations on Li_2O_2,[55] 1×10^7 cm^{-3}. A summary of calculated defect formation energies and concentrations in Na_2O_2 is provided in Table 3.2. Contrary to some experimental studies on Na_2O_2,[86] we do not find that sodium interstitials are present in high concentrations in Na_2O_2. Indeed, out of a trial set of 9 candidate Na interstitial geometries, even the most stable configuration has a high formation energy in excess of 2 eV.

In peroxides and superoxides a hole (electron) polaron consists of a missing (additional) electron localized on an O_2 dimer, resulting in a contraction (extension) of the covalent O-O bond. The localization of a polaron at any given dimer site may be corroborated by examining changes in the O-O bond length, magnetization density, and density of states (DOS) of the system. In Na_2O_2, we observed that the O-O bond length decreases from 1.47/1.48 on the two symmetry-distinct O_2 sites, to 1.31 Å when a hole polaron is present. Analysis of the magnetization density reveals that a magnetic moment $\mu = 1\mu_B$ emerges on dimers hosting a hole polaron (Figure 3.4a), with a characteristic shape of a $\pi_{x,y}^*$ orbital, which is consistent with the presence of an unpaired electron in a superoxide-like O_2^{1-} dimer (Figure 3.1b). The magnetic moment remains unchanged ($\mu = 0\ \mu_B$) for other O_2^{2-} ions in the supercell.

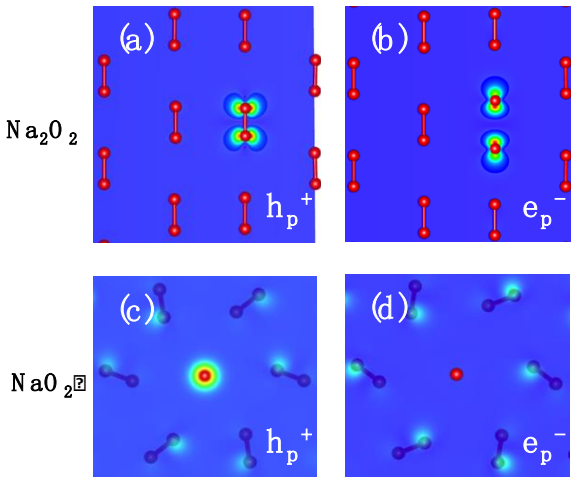

Figure 1.9 Magnetization Density for (a) hole polaron in Na_2O_2; (b) electron polaron in Na_2O_2; (c) hole polaron in NaO_2; and (d) electron polaron in NaO_2. Note that in panels (c) and (d) the bond axis of the oxygen dimers is into the plane of the page. The color scheme is set such that blue represents a magnetization density of zero, and red corresponds to 0.27 μ_B/Bohr^3.

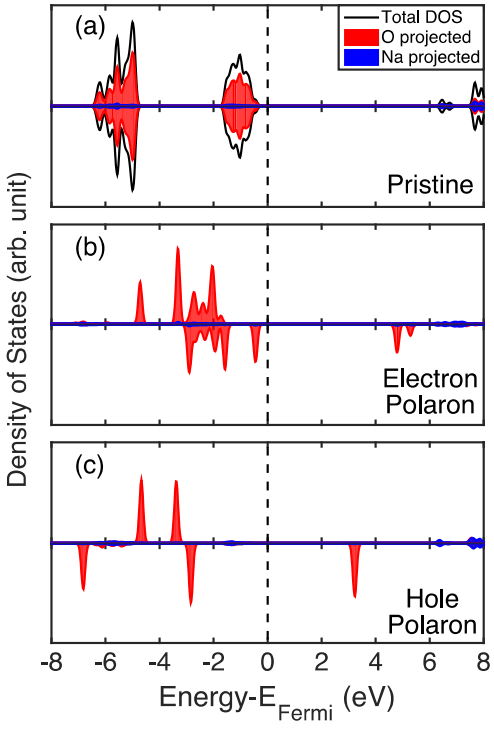

Figure 1.10 Density of States (DOS) of Na_2O_2 calculated using HSE_α ($\alpha = 0.48$). (a): DOS for the pristine compounds. (b): DOS projected onto an electron polaron cluster. (c): DOS projected onto a hole polaron cluster. A cluster is defined as an oxygen dimer and its nearest neighbor sodium ions.

The density of states (DOS), Figure 3.5, provides further information regarding the electronic structure of pristine and defective Na_2O_2. (Note that in Figure 3.5 the Fermi level E_f is set to the highest occupied eigenvalue, which is a convention commonly used in first-principles calculations. A more accurate description of the E_f is given in Figure 3.3 and Figure 3.6, which accounts for charge neutrality; in this case E_f is 2.4 (1.8) eV above the VBM for NaO_2 (Na_2O_2).) The DOS for the pristine supercell (Figure 3.5) indicates an equal number of spin-up and spin-down states, with full occupation of $\pi_{x,y}^*$ orbitals on the O_2^{2-} dimer. Localization of a hole on the O_2 dimer results in a splitting between the occupied states and unoccupied states of $\pi_{x,y}^*$ (Figure 3.5c). This leads to the emergence of a new (empty) state above the Fermi level.

Formation of an electron polaron in Na_2O_2 increases the formal negative charge on the effected peroxide (O_2^{2-}) ion to O_2^{3-}. This electron occupies a σ^* orbital, resulting in a large increase to the O-O bond length from 1.48/1.49 to 2.20/2.29 Å. The presence of the additional electron is also reflected in the DOS (Figure 3.5b), where a new peak appears below the conduction band minimum (CBM), which is accompanied by the emergence of a new state below the Fermi level and a splitting of occupied spin up and spin down channels. This change is concurrent with the emergence of a magnetic moment $\mu = 1\mu_B$ on the dimer hosting the additional (unpaired) electron, Figure 3.5b, which has the characteristic shape of a σ^* orbital.

3.3.3 Intrinsic Defects in NaO_2

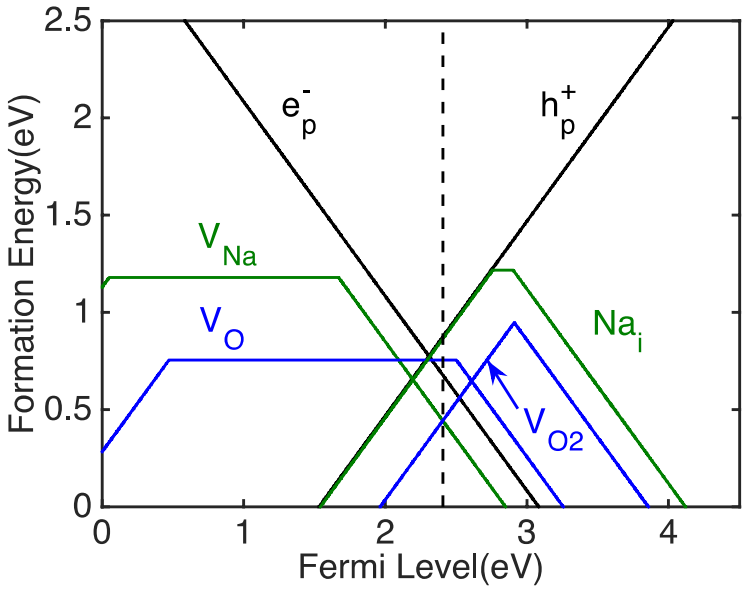

Figure 1.11 Defect formation energy of the O vacancy (red lines), Na vacancy (green lines), electron polarons and hole polarons (black lines) obtained using the HSE_α ($\alpha = 0.48$) hybrid functional in NaO_2.

Figure 3.6 shows the calculated formation energies for O vacancies (V_O), O_2 vacancies (V_{O2}, in which an entire O_2 molecule is removed), Na vacancies (V_{Na}), Na interstitials (Na_i), electron polarons (e_p^-) and hole polarons (h_p^+) as a function of the Fermi level in NaO_2 (Figure 3.4). In NaO_2 the present calculations suggest that the dominant ionic charge carriers consist of three species: negative sodium vacancies (V_{Na}^-), positive oxygen dimer vacancies ($V_{O_2}^{1+}$), and positive sodium interstitials (Na_i^+). These have formation energies 0.44, 0.44 and 0.87 eV, respectively. The formation energies of V_{Na}^- and $V_{O_2}^{1+}$ are approximately 0.46 eV smaller than those of the lowest-energy defects in Na_2O_2, suggesting that the superoxide will support a higher concentration of ionic defects compared to the peroxide. Indeed, the equilibrium concentrations of V_{Na}^- and $V_{O_2}^{1+}$ are on the order of 10^{15} cm^{-3}, which is eight orders of magnitude higher than for the dominant defects in Na_2O_2 and Li_2O_2. These findings agree qualitatively with the experimental data of Gerbig *et al.*, who found that O_2 vacancies and potassium interstitials were the dominant ionic charge carriers in potassium superoxide.[139] A summary of calculated defect formation energies and concentrations in NaO_2 is provided in Table 3.3.

Electron polarons (e_p^-) are predicted to be the highest-concentration electronic charge carriers in NaO_2, with formation energies of 0.68 eV (Figure 3.6). Somewhat surprisingly, the superoxide also appears to support hole polarons (h_p^+) as minority carriers; the formation energy for hole localization is 0.88 eV, only moderately higher than that for the formation of a localized excess electron.

Table 1.5 Defect formation energies E_f(eV) and concentrations C (cm^{-3}) in NaO_2

Defect Type	E_f(eV)	C (cm^{-3})	Defect Type	E_f(eV)	C (cm^{-3})
e_p^-	0.68	1×10^{11}	h_p^+	0.88	5×10^{7}
V_{Na}^+	3.54	1×10^{-37}	V_O^+	2.69	4×10^{-23}
V_{Na}^0	1.18	4×10^{2}	V_O^0	0.76	1×10^{10}
V_{Na}^-	0.44	9×10^{14}	V_O^-	0.85	3×10^{8}
Na_i^+	0.87	7×10^{7}	$V_{O_2}^{1+}$	0.44	9×10^{14}
Na_i^0	1.22	9×10^{1}	$V_{O_2}^{0}$	1.09	1×10^{4}
Na_i^-	1.72	4×10^{7}	$V_{O_2}^{1-}$	1.45	1×10^{-2}

For an electron polaron in NaO_2 the O-O bond length increases from 1.30 to 1.47 Å, the latter value being very similar to that of peroxide O_2 dimers in Na_2O_2 (1.47/1.48 Å). Moreover, the added electron fills a $\pi_{x,y}^*$ orbital, making that orbital fully occupied, Figure 3.1c. Subsequently, the magnetic moment on this dimer disappears, while it remains $1\mu_B$ for the rest of O_2^{1-} ions in the supercell (Figure 3.4d). We note that the formation energy of an electron polaron in NaO_2 (0.68 eV) is much lower than in Na_2O_2, 2.07-2.33 eV. This may be explained by the fact that in NaO_2 an electron polaron occupies a $\pi_{x,y}^*$ orbital, whereas in Na_2O_2 it must occupy a higher energy σ^* orbital.

Regarding the nature of hole polarons in NaO_2, similar to what is observed for Na_2O_2, missing electrons localize on O_2 dimers, resulting in a decrease of the O-O bond length from 1.30 to 1.19 Å. Thus a hole polaron transforms a superoxide dimer, O_2^{1-}, into a neutral gas-like state, O_2^0; this is further supported by the similarity in the O-O bond length for gaseous O_2, 1.21 Å.[156] The magnetic moment on the dimer hosting the hole polaron, $\mu = 2\mu_B$, is twice as large as in the peroxide, Figure 3.4c, and is consistent with gaseous O_2: The trapping of a hole in NaO_2

results in two unpaired electrons in the $\pi_{x,y}^*$ orbital (Figure 3.1a), with each electron contributing a magnetic moment of $1\mu_B$. Consequently, only a spin-down peak can be seen in the DOS of the hole polaron (Figure 3.7f).

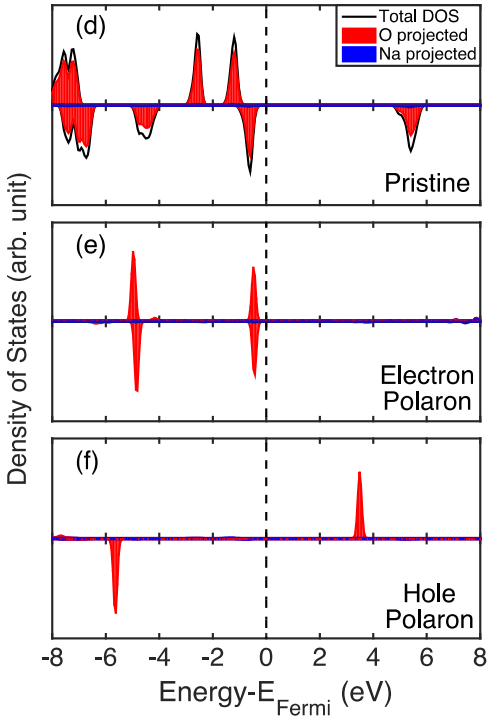

Figure 1.12 Density of States (DOS) of NaO_2 calculated using HSE_α ($\alpha = 0.48$). (d): DOS for the pristine compounds. (e): DOS projected onto an electron polaron cluster. (f): DOS projected onto a hole polaron cluster. A cluster is defined as an oxygen dimer and its nearest neighbor sodium ions.

The DOS for Na_2O_2 and NaO_2 share many features upon addition and removal of electrons. For example, in pristine NaO_2, the missing electron in the $\pi_{x,y}^*$ orbitals results in a splitting of the energy levels (Figure 3.7d). This behavior is very similar to the DOS of an O_2 dimer in Na_2O_2 that hosts a hole polaron, Figure 3.7c. Similarly, the addition of an electron to NaO_2 converts a superoxide (O_2^{1-}) dimer to a peroxide-like charge state (O_2^{2-}), creating an electron polaron. Note that the DOS for this state, Figure 3.7e, closely resembles that of pristine Na_2O_2.

3.3.4 Mobilities

The second quantity needed to estimate the conductivity of the Na-O_2 discharge phases is the mobility of the predominant (i.e., highest-concentration) charge-carrying species. We first consider the mobilities of ionic species. In Na_2O_2, ionic conductivity originates from the migration of negative sodium vacancies, V_{Na}^-. (Since during this process a sodium cation, Na^+ moves counter to the vacancy, one may equivalently consider this mechanism to be vacancy-mediated Na-ion migration.) Energy barriers for seven vacancy migration pathways in Na_2O_2 were calculated using the NEB method. Figure 3.8a shows the energy profiles for those pathways where the energy barriers are less than 1eV. We explored both intra-layer and inter-layer migration pathways. The lowest energy pathway, "Na_2O_2-intra3," corresponds to migration between a vacant Na site in an oxygen rich layer (V_{Na1}^-) and an adjacent site in the oxygen poor layer (V_{Na2}^-). This process has an energy barrier of 0.34 eV relative to V_{Na1}^- and 0.50 eV relative to V_{Na2}^-. Setting E_b to the average of these two values gives a defect diffusion coefficient of 9×10^{-10} cm^2 s^{-1}. The calculated diffusion barriers in Na_2O_2 are in reasonable agreement with that of Araujo *et al*., 0.50 eV,[144] and are only slightly larger than what has been reported for the migration of negative lithium vacancies in Li_2O_2, 0.30 to 0.39 eV.[55,157,158] The slight increase in barriers found for Na_2O_2 may be due to the longer diffusion distance in this phase compared to that of Li_2O_2 (3.02 Å *vs.* 2.60 Å).

Activation energies for the three dominant ionic charge carriers in NaO_2 (V_{Na}^-, Na_i^+ and $V_{O_2}^{1+}$) were also evaluated. The calculations suggest that these defects have modest migration barriers (Figure 3.8a), pathways labeled "NaO_2-V_{Na}^-", "NaO_2-Na_i^+" and "NaO_2-V_{O2}^+") of 0.35, 0.20 and 0.26 eV, respectively, corresponding to diffusion coefficients of 2×10^{-8}, 3×10^{-6} and 6×10^{-7} cm^2 s^{-1}. The high symmetry of the NaO_2 crystal structure suggests that vacancy migration V_{Na}^- occurs via a single pathway wherein a vacancy migrates from one vertex of a Na-ion octahedron to a nearest-neighbor vertex. This pathway lies close to the octahedron's edge, and slightly below the octahedron faces which meet at the edge joining the relevant vertices. The calculated energy barrier for this process, 0.35 eV (Figure 3.8a), is slightly smaller than the average barrier for vacancy migration in Na_2O_2. The diffusion of an O_2 vacancy is accompanied by the migration of an O_2 dimer in the opposite direction. The barrier for this process includes the rotation of the dimer as it reorients itself along the [111] direction of the nearest-neighbor site. As previously mentioned, this process exhibits a small barrier of 0.26 eV (Figure 3.8a),

which qualitatively agrees with the experimental data from Gerbig *et al.*, who found that superoxide ions are highly mobile in the heavier alkali-metal superoxides.[139]

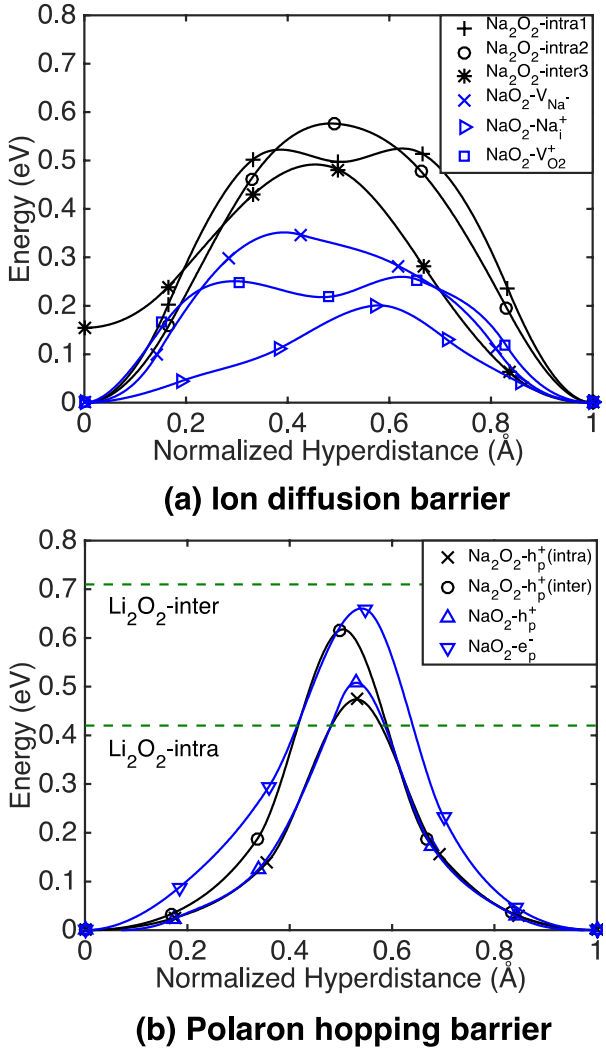

Figure 1.13 Energy barriers calculated using the NEB method for (a) ionic charge carriers and (b) polarons. Blue curves refer to NaO_2; black curves refer to Na_2O_2. For simplicity, only pathways with barriers less than 1 eV are shown. In panel (a) barriers are plotted for migration of three ionic species in NaO_2: negative sodium vacancies (V_{Na}^-), positive sodium interstitials (Na_i^+), and positive oxygen dimer vacancies ($V_{O_2}^{1+}$). One pathway between nearest-neighbor V_{Na}^-, Na_i^+ and $V_{O_2}^{1+}$ are considered. In Na_2O_2 only sodium vacancies (V_{Na}^-) are relevant, and five distinct pathways were considered between two symmetry inequivalent V_{Na}^- sites. In panel (b), electron polaron (e_p^-) and hole polaron (h_p^+) hopping barriers are compared with those for hole polaron hopping in Li_2O_2 from Radin *et al.*[55] (green dashed lines).

Regarding the mobilities of electronic species, Figure 3.3 and Figure 3.6 indicates that hole polarons are the dominant charged defects in Na_2O_2 while electron polarons are the dominant charged defects in NaO_2. Consequently, activation energies for polaron hopping were calculated for both compounds, Figure 3.8(b) using the HSE_α functional. For Na_2O_2, five hole polaron hopping pathways were considered, accounting for the two symmetry inequivalent oxygen dimer sites, as well as intralayer and interlayer hops.

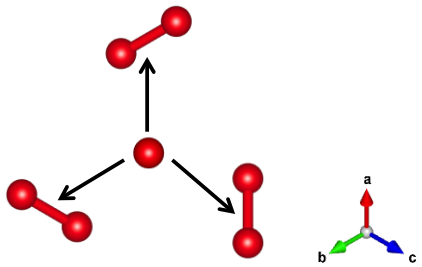

Figure 1.14 Nearest neighbor defect hopping (migration) pathways in NaO_2. The central O_2 has its bond axis normal to the plane of the page. The three arrows represent the directions of possible hops to the three nearest-neighbor O_2 sites.

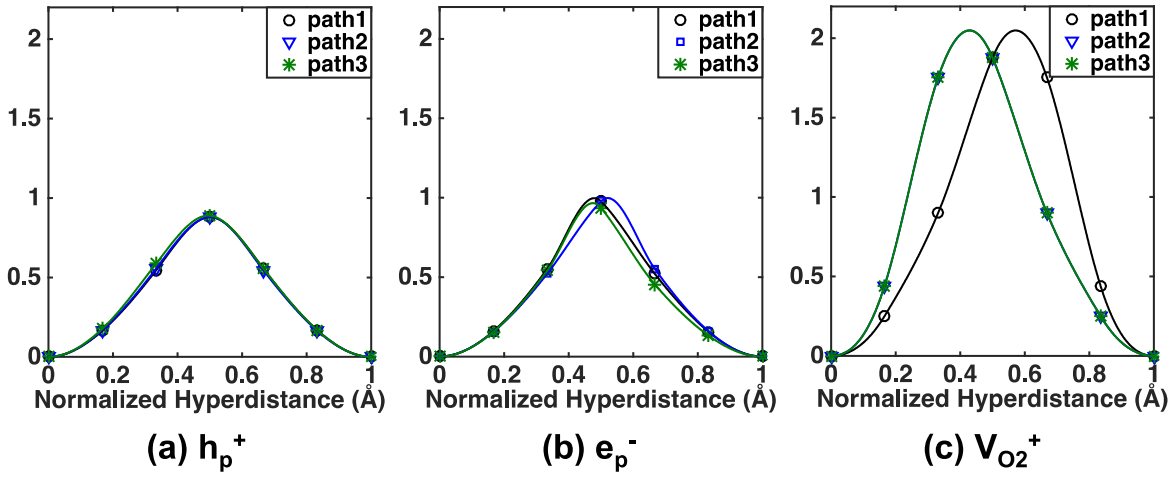

Figure 1.15 Single point energy barriers for hopping of (a) hole polarons (h_p^+), (b) electron polarons (e_p^-), and (c) positive oxygen dimer vacancies (V_{O2}^+) in NaO_2 along the three directions depicted in Figure 3.9.

In the case of NaO_2, all O_2 dimers are aligned along the 4 [111] directions (Figure 3.9). For each defect type involving an O_2 site (electron polarons, hole polarons, and oxygen dimer

vacancies), there are three symmetry inequivalent nearest neighbor hopping directions to an adjacent O_2 site. Accounting for the different [111] orientations of these dimers, three symmetry-distinct hops are possible. Figure 3.10 shows that the un-relaxed barriers for these hops are identical (In all cases the barrier heights for the different pathways differ by less than 10 meV.), indicating that dimer orientations does not strongly influence the barriers for polaron hopping in NaO_2 (i.e. polaron hopping is isotropic).

Figure 3.8b shows the polaron hopping barriers for Na_2O_2 (black) and NaO_2 (blue) calculated using the CI-NEB method. We find that the intralayer barrier in Na_2O_2, $E_b^{intra} = 0.47$ eV is 0.15 eV lower than the interlayer barrier, $E_b^{inter} = 0.62$ eV. This implies that hole polaron hopping is anisotropic, and should be faster in the in-plane directions (i.e., along [1-100] or [11-20]) compared to out-of-plane hopping along [0001]. This is similar to what was previously reported in Li_2O_2, where the in-plane barrier (Figure 3.8b dashed blue line) was 0.42 eV and out-of-plane barrier (dashed green line) was 0.71 eV.[55] Importantly, in NaO_2 the calculated barrier for migration of an electron polaron, 0.66 eV, is higher than that for migration of a hole polaron, 0.51 eV. Therefore, the mobility trend for polaron migration in NaO_2 (i.e., more facile hopping of holes), is the reverse of the stability trend (i.e., electron polarons are more stable).

3.3.5 Conductivity

The conductivity arising from charged defects (polarons or ions) depends on both the concentrations and mobilities of these carriers, and may be expressed as:

$$\sigma = eC\mu = \frac{C\nu a^2 e^2}{k_B T} e^{-E_B/k_B T} . \quad (3.1)$$

Table 1.6 Calculated ionic and electronic conductivities (S cm^{-1}) for Na_2O_2 and NaO_2, and their comparison with prior calculations on Li_2O_2. For ionic conductivities in NaO_2, the first value refers to contributions from positive oxygen dimer vacancies ($V_{O_2}^{1+}$), the second value refers to contributions from sodium vacancies (V_{Na}^{-}).

Compound	Ionic Conductivity (S/cm)	Electronic Conductivity (S/cm)
Li_2O_2	9×10^{-19}	5×10^{-20}
Na_2O_2	5×10^{-20}	1×10^{-20}
NaO_2	$4\times10^{-9}/1\times10^{-10}$	1×10^{-19}

The calculated conductivities for Na_2O_2 and NaO_2 are summarized in Table 3.4, and compared with prior calculations on Li_2O_2. Turning first to Na_2O_2, our calculations suggest that the conductivity of Na_2O_2 is nearly identical to that of Li_2O_2: In both of these compounds the ionic conductivity is similar to the electronic conductivity, with values of approximately 10^{-20} S/cm. The low conductivity values suggest that transport through pristine Na_2O_2 bulk will be limited, unless pathways coupled to microstructural features emerge (surfaces, grain boundaries, amorphous regions, *etc*.) Another possibility is that charge will be transported through a liquid phase mechanism involving a soluble superoxide intermediate.[159] Such an intermediate could acquire charge (i.e., be reduced) via electron tunneling through a thin Na_2O_2 film or through adsorption on a portion of the porous carbon support that is not buried by the discharge phase.

Regarding transport in NaO_2, Table 3.4 shows that the ionic conductivity of this phase is predicted to be significantly higher than in the peroxides. The calculated total ionic conductivity in NaO_2 is $4x10^{-9}$ S/cm. Most of this conductivity can be attributed to *p* type conduction arising from positive oxygen dimer vacancies, with n type conduction from negative sodium vacancies contributing to a lesser degree. These conductivity values are 9 to 10 orders of magnitude higher than in Na_2O_2 or Li_2O_2.

The counterbalancing trends in the concentrations and mobilities of hole and electron polarons in NaO_2 results in a nearly equal contribution of these species to the electrical conductivity of NaO_2. Conductivity arising from electron polarons is predicted to be 8.2×10^{-20} S/cm, while for holes the conductivity is about 5.5 times smaller, 1.5×10^{-20} S/cm.

We previously argued that electronic transport was more important than ionic transport in determining the efficiency of Li/O_2 batteries that discharge to crystalline Li_2O_2.[55] This argument was based on the observation that typical cathode support materials, such as carbons, are ion blocking. Consequently, ionic transport would be hindered (except for a transient contribution) due to the inability of Li ions to cross the Li_2O_2/C interface. This scenario also should hold for the Na/O_2 systems considered here. Nevertheless, facile ionic diffusion could facilitate de-sodiation during charging, resulting in the formation of a sub-stoichiometric $Na_{1-x}O_2$ phase. (Consideration of a de-sodiation pathway is motivated by earlier studies of the $Li\text{-}O_2$ system which proposed de-lithiation as a mechanism for charging of Li/O_2 cells.[153,160]) If the resulting $Na_{1-x}O_2$ phase exhibited higher electronic conductivity than its stoichiometric parent, then faster ionic conductivity would indirectly contribute to enhanced charge transport. Additional study is needed to test this hypothesis.

We focus the remainder of our discussion on conductivity due to hopping of polarons. It has been suggested that the large size of NaO_2 particles formed during discharge, and the low overpotentials observed during charging, indicate that this phase should have a higher electronic conductivity than Na_2O_2.[78,80] An earlier experiment also reported that KO_2 had a moderately high electronic conductivity which was comparable to that of copper dust. Nevertheless, the present calculations do not support the notion of high conductivity in NaO_2, given that they predict the superoxide to have a bulk electronic conductivity (10^{-19} S/cm) that is nearly identical to that of sodium peroxide. Our results are consistent with the conclusions reached by Gerbig *et al.,* who measured conductivities of the heavier alkali-metal superoxides (KO_2, RbO_2 and CsO_2.), and

found that electronic conductivities were comparable to those of Li_2O_2.[86] A prior study indicated that a conductivity of 10^{-12} S/cm was needed to achieve the performance targets suggested for a practical Li/O_2 cell.[55] According to that analysis, a conductivity of 10^{-19} S/cm (as calculated for NaO_2) would result in an overpotential for the oxygen evolution reaction of approximately 0.4 V, which is significantly larger than what is observed during charging of NaO_2-containing cathodes.[68,75] Therefore, we conclude that a higher electronic conductivity of NaO_2 *cannot* explain the improved performance of cells that discharge to NaO_2.

Which other factors could play a role? Possibilities include conduction pathways that are coupled to microstructural features, such as a higher concentration of polarons at surfaces or grain boundaries.[52,154,161] Deviations from equilibrium conditions – for example during fast discharge – could also result in a higher, non-equilibrium density of charge carriers frozen into the system. Chemical factors may also play a role: A recent study by McCloskey *et al*.[68] observed that less electrolyte decomposition occurred in a Na-O_2 battery during the first galvanostatic discharge-charge cycle. The presence of these side-reaction products has been suggested as a source of overpotentials during OER in Li/O_2 cells.[162–164]

3.4 Conclusion

In this chapter, a combination of density functional and quasi-particle calculations have been used to characterize charge transport in the peroxide and superoxide discharge products commonly observed in Na-O_2 batteries. Higher conductivity within the NaO_2 phase has been proposed to explain why cells that discharge to NaO_2 exhibit much lower charging overpotentials than those that discharge to Na_2O_2. The present study tests this hypothesis by calculating the intrinsic conductivity of these phases. In so doing, it explores the connection between cell efficiency and the composition of the discharge product. This connection remains poorly understood, as are the mechanisms of charge transport in peroxides and superoxides.

Our calculations reveal that both Na_2O_2 and NaO_2 are electronic insulators, with band gaps in excess of 5 eV. In the case of sodium peroxide, the transport properties are remarkably similar to those reported previously for lithium peroxide, suggesting a low conductivity on the order of 10^{-20} S/cm.

Compared to the peroxides, transport in superoxides has not been widely explored. The present study reveals that transport in NaO_2 has some features in common with the peroxide; nevertheless, several important distinctions exist. Similar to Na_2O_2, NaO_2 is predicted to be a poor electrical conductor, wherein transport is limited by sluggish charge hopping between O_2 dimers. Different from Na_2O_2, in NaO_2 this transport is mediated by a *combination* of electron and hole polarons. More specifically, conductivity arising from electron polarons is predicted to be 8.2 x 10^{-20} S/cm, while for holes the conductivity is about 5.5 times smaller, 1.5 x 10^{-20} S/cm. The mixed contribution to electrical conductivity is due to counterbalancing trends in the concentrations and mobilities of hole and electron polarons in NaO_2. Taken together, these data indicate that electronic transport in alkali peroxides and superoxides is governed by the unusual ability of oxygen dimers to adopt three charge states: O_2^{2-}, O_2^{1-}, and O_2^{0}.

An additional distinguishing feature of the superoxide is its ionic conductivity, which is 10 orders of magnitude larger than the electronic component. The ionic component is comprised primarily of *p*-type contributions from mobile oxygen dimer vacancies, and from *n*-type contributions from negative sodium vacancies. The mobility of oxygen dimers in the NaO_2 lattice is consistent with a recent experimental study by Gerbig *et al*., who found that superoxide ions are highly mobile in the heavier alkali-metal superoxides.

The limited electronic conductivity predicted for NaO_2 suggests that bulk transport within this phase is unlikely to account for the low overpotentials associated with its decomposition during charging in a Na/O_2 electrochemical cell. We therefore conclude that the enhanced efficiency observed in cells that discharge to NaO_2 must arise from other phenomena, such as a reduction in the extent of electrolyte decomposition or enhanced charge transport through liquid-phase processes.

Chapter 4: Intrinsic Defect Conductivity in LiO_2 and KO_2

4.1 Introduction

As discussed in Section 1.4, a typical Li-O_2 cell exhibits a high charging overpotential, which significantly reduces its round-trip efficiency. The primary discharge product of a Li/O_2 cell is crystalline Li_2O_2, and it's proposed that high overpotentials originate from the low intrinsic conductivity of Li_2O_2.[1] Superoxide ions O_2^- have also been reported (occasionally) in these cells in the discharge product by *in situ* spectroscopic data. Solid lithium superoxide LiO_2 is difficult to synthesize in pure form because it is known to be thermodynamically stable only at T < 50K. Therefore, in a typical Li/O_2 cell, it is expected that LiO_2 disproportionates into Li_2O_2 and O_2.[2] Surprisingly, Lu *et al.*[3] have synthesized crystalline LiO_2 during discharge of a Li-O_2 cell using a graphene cathode decorated with iridium (Ir) nanoparticles. They showed that the LiO_2 formed in the Li-O_2 battery is stable during repetitive charge and discharge cycles, and exhibits a relatively low overpotential. The low charging overpotentials were explained by several factors, one of them being the metallic behavior of LiO_2 predicted by DFT calculation with generalized gradient approximation (GGA) functional.[3] However, calculations using hybrid functionals predict an insulating behavior for bulk LiO_2, with a band gap of 3.7 ~ 4.0 eV.[4,5]

Other metal-oxygen batteries have been made by replacing lithium with other alkali metals. One example is Na-O_2 battery. As discussed in Section 1.5, the discharge product of Na-O_2 batteries appears to be very different from that of the Li-O_2 batteries. Some studies have reported Na_2O_2 as the main discharge product,[6] while others report NaO_2.[7] A Na-O_2 cell with Na_2O_2 as a discharge product suffered from a high charging overpotential of ~1 V.[6] In contrast, significantly low charging overpotentials of Na-O_2 cell (~ 0.2 V) have been reported when the

discharge product consisting mainly NaO_2.[7] Our previous work (Chapter 3) employing hybrid functionals found both Na_2O_2 and NaO_2 are band insulators with band gap excess of 5 eV.[8]

K-O_2 batteries are yet another example of a metal-oxygen system. As discussed in Section 1.6, KO_2 appears to be the primary discharge product observed. KO_2 is thermodynamically stable, and it has been demonstrated that K-O_2 cells containing KPF_6 salt in DME form solely KO_2 (no K_2O_2) during the oxygen reduction reaction. Importantly, the total overpotential for the first cycle of these cells was less than 50 mV. Experimentally, there are controversial reports regarding the conductivity of KO_2. One early measurement reported moderately high conductivity in KO_2 (approximately 1~10 S/cm).[9] More recently, Gerbig *et al.* examined the total (ionic + electronic) conductivity of KO_2 using the electromotive force method. The value of the electronic conductivity could not be exactly determined in the investigation, but was estimated to be less than 10^{-7} Ω^{-1} cm^{-1} at 200 °C,[10] a much smaller value than in the initial report.

Given the importance placed on the conductivity of the superoxides in controlling the efficiency of M-O_2 batteries, and the apparent lack of consensus in the literature regarding these properties, the goal of this chapter is to systematically calculate the intrinsic conductivities across the remaining superoxide family: LiO_2 and KO_2. A hybrid functional with tuned fraction of screened exact exchange was used to calculate the bulk electronic properties and intrinsic defects properties in LiO_2 and KO_2. Comparisons are made to our earlier work on NaO_2 (Chapter 3).[8] We examined charge transport in each material by predicting the concentrations and mobilities of several charge-carrying point defects such as polarons, vacancies, and interstitials. We found that both LiO_2 and KO_2 are bulk insulators, with bandgaps in excess of 4 eV. LiO_2 has high electronic and ionic conductivity. Particularly, LiO_2 exhibits high equilibrium concentrations and high mobilities of electron polarons, leading to a high electronic conductivity. KO_2, similar to NaO_2, has high ionic conductivity but low electronic conductivity. By comparing with our previous work on Li_2O_2,[1] Na_2O_2 (Chapter 3) and NaO_2 (Chapter 3), we propose general intrinsic defect conduction mechanisms in peroxides and superoxides. In these materials, electronic transport is mediated by polaron hopping, wherein oxygen dimers adopt three different charge states: O_2^{2-},

O_2^{1-}, and O_2^0. Regarding ionic carriers, defects on the cation lattice (metal vacancies) dominate for peroxides, whereas oxygen dimer vacancies prevail for the alkali superoxides.

4.2 Methodology

Density Functional Theory (DFT) calculations were performed using the Vienna ab initio Simulation Package (VASP).[11–14] Geometries and the electronic structures were relaxed by both the GGA+U method (with the Perdew−Burke−Ernzerhof (PBE) functional[15]) and the Heyd-Scuseria-Emzerhof (HSE06) hybrid functional.[16,17] A Γ-centered K-point grid with density 6 × 6 × 6 for LiO_2 and KO_2 was used for calculations involving primitive cells. The plane wave energy cutoff was set at 460 eV for the hybrid functional, and 900 eV for GGA+U method. For structure optimizations, all ions were relaxed to a force tolerance of 0.02 eV/Å or less. Many-body perturbation theory (GW) was used for the calculation of accurate bandgaps. A HSE06 calculation was used as the starting point for all GW calculations.

As discussed in Section 2.2, semilocal functionals may poorly describe electronic properties of alkali-metal superoxides.[8,18] For defect calculations, the semi-local functionals may fail to predict localized charge distributions such as polarons, and can underestimate the polaron hopping barriers.[1] Therefore, we used the 'α-tuned' hybrid functional approach, where α is a mixing parameter controlling the fraction of Hartree-Fock exchange included. Based on previous calculations in which the impact of the mixing parameter on formation energies and migration barriers were examined in superoxides and peroxides,[1,4] the present study adopts the value α = 0.48. This value allows consistent comparisons to be made between the present calculations on alkali superoxides (Chapter 3) and prior studies involving alkali peroxides (Chapter 3).

Regarding the crystal structure for LiO_2, it should be noted that no standard X-ray diffraction (XRD) pattern has yet been established. Nevertheless, some previous experimental observations suggested the marcasite structure (space group *Pnnm*) as a plausible candidate for the ground-state configuration.[19] Moreover, the experimental O-O stretching frequency in the MO_2 (M = Li, Na, K, Rb, Cs) exhibits a small dependence upon the alkali metal cation. The O^{2-}

Raman frequency is 1097 cm^{-1} for LiO_2, which drops to 1094 cm^{-1} for NaO_2, then increases to 1108 cm^{-1} for KO_2, 1110 cm^{-1} for RbO_2, and 1114 cm^{-1} for CsO_2.[20] The small difference in the Raman frequency implies that alkali metal superoxides have similar O-O bond length. Therefore, many DFT studies built a proposed LiO_2 structure by replacing Na with Li in the NaO_2 marcasite structure.[4,19,21] Consequently, we adopt the marcasite structure (Figure 4.1a) for our calculations in the present work. In the LiO_2 marcasite structure, the LiO_2 units exhibit an ABAB stacking sequence along c axis: each layer has the same number of Li atoms and O_2 molecules. The oxygen dimers in (001) plane within one layer, with the angles between the oxygen dimer and the a-axis equal to +41° and -41° for A and B layers, respectively.

As for the crystal structure for KO_2, at room temperature it crystallizes with a body-centered-tetragonal structure (space group *I4/mmm*) of CaC_2 type, wherein the O_2^- ions are on average orientated parallel to the tetragonal axis.[22] Because of the orbital degeneracy of the O_2^- ion, the energy of the system can be lowered by a Jahn-Teller distortion. This can arise from both tilting of the O_2^- molecular axis away from a high-symmetry direction[23] and the displacement of the center of mass from a symmetry position. There have been several theoretical reports to study the coupled structural and electronic properties in KO_2. Nandy *et al.* optimized the structure with no symmetry constraints imposed by the initial structure where all O_2^- ions are parallel to the z-axis, leading to a structure (not tetragonal), which is 22 meV/f.u. lower in energy than the high symmetry structure.[24] Kim *et al.* kept the tetragonal symmetry but rotated all the O_2 dimers by ~30° in the same direction.[25] The resulting structure exhibited a bandgap, consistent with the insulating nature of KO_2.[18] However, the precise direction of the tilted O_2 bond axis is still uncertain.

In this study, we explore a precession model for the KO_2 room temperature structure. Starting from the high symmetry tetragonal (HST) structure, we assume all the O_2 dimers precess around the z-axis. There are two O_2 dimers in the HST conventional unit cell; three angles were used to describe the O_2 orientation: θ, φ1 and φ2 (Figure 4.2a). Given the computational expense of hybrid functionals, the search for the lowest energy angles was performed using a two-step procedure with the GGA + U method. At first step, we rotated the two O_2 molecules in the unit cell simultaneously along the [100] axis. This was done by relaxing the lattice constants and θ while keeping the constraint of φ1= 0, φ2 = 90° and tetragonal symmetry. An optimal angle of θ

= 22° with was found to have the lowest energy, assuming ferromagnetic ordering. As a second step, we rotated the two O_2 dimers separately along the [001] axis (z-axis). This was done by varying φ1 and φ2 while constraining θ = 22° and maintaining tetragonal symmetry.

Figure 4.2b shows the energy map resulting from varying φ1 and φ2. A maximum energy was found when the two O_2 dimers were oriented along the same direction (φ1= 0°, φ2 = 270°), while the minimum energy was found when the O_2 dimers were oriented along opposite directions when viewing along the z-axis, i.e., φ1= 0°, φ2 = 90°. The difference between the maximum energy and minimum energy is small, only 5 meV/atom, implying that the O_2 orientation has a small effect on the total energy. The lowest energy KO_2 structure (θ = 22°, φ1= 0°, φ2 = 90°, Figure 4.1) was used this for subsequent bulk and defects calculations. Similar to LiO_2 and the low temperature NaO_2 phase (*Pnnm* structure), oxygen dimers in bulk KO_2 (precession model) are located in (001) plane.

For defect calculations, the simulation cells consisted of a 3 × 3 × 2 LiO_2 supercell (108 atoms) and a 3 ×3 ×2 KO_2 supercell (108 atoms). Based on previous calculations in NaO_2, all the defects considered were selected from five defect types:[8] negative metal vacancies (V_M^-), positive metal interstitials (M_i^+), positive dimer vacancies (VO_2^+), electron polarons (e_p^-) and hole polarons (h_p^+). The importance of these defects in LiO_2 was also shown by Li *et al.*[4]

The Γ point was used for all defect calculations. See Section 2.3 for details. The chemical potential of oxygen was assumed to be fixed by equilibrium with oxygen in the atmosphere, which is given by the formula,

$$\mu_O = \frac{1}{2}\mu_{O_2} = \frac{1}{2}\left[E_{O_2}^{DFT,corr} + k_B T - TS_{O_2}^{expt}\right], \tag{4.1}$$

where the $k_B T$ term accounts for the pV contribution to the free energy, and $S_{O_2}^{exp}$ is the experimental entropy.[26] We have intentionally neglected contributions to the free energy from

translational, rotational, and vibrational degrees of freedom because we are not including these terms in the bulk phases; this choice maintains some degree of error cancellation.

In alkali superoxides, the chemical potential of alkali metals (Li, Na, K) were established by the relation

(4.2) $$\mu_M + 2\mu_O = E_{tot}[MO_2] \ ,$$

where *M = Li, Na, K* is the alkali metal, and $E_{tot}[MO_2]$ is the total energy per formula unit of the corresponding alkali superoxide. Knowing that DFT calculations tend to overbind gas-phase O_2, an O_2 correction of 0.20 eV was applied for the ground-state energy of the O_2 molecule. This is correction value was determined using a linear fit between the calculated and experimental formation enthalpies for the alkali superoxides: marcasite LiO_2, pyrite NaO_2, and tetragonal KO_2. Coincidentally, we note that this value is equal to the value in our previous work on NaO_2,[8] where we calculated the correction using the experimental value of the NaO_2 formation enthalpy only. This coincidence, however, allows us to compare the results of the present study on LiO_2 and KO_2 with our previous work on NaO_2.[8]

4.3 Results and discussion

4.3.1 Structure and Bandgaps

Table 1.7 The calculated magnetic ordering, energy between ferromagnetic ordering and antiferromagnetic ordering, lattice parameters a, b, c (Å), O-O bond length dO-O (Å), the distance between Li atom and its nearest O atom dM-O_2 (Å), and the oxygen dimer orientation.

Structure	Magnetization	E_{FM}-E_{AFM} (meV)/f.u.	a (Å)	b (Å)	c (Å)	dO-O (Å)	dM-O_2 (Å)	O_2 Orientation
LiO_2 (Orthorhombic)	FM	-6	4.011	4.783	3.042	1.30	2.52/2.39	[110]
NaO_2 (Pyrite)	FM	-42	5.416	5.416	5.416	1.31	2.71	Four <111>
KO_2 (HST)	FM	-36	3.991	3.991	6.843	1.31	2.91/3.36	[001]
KO_2 (Precession)	FM	-2	4.111	4.111	6.720	1.31	2.91/3.36	[110]

Table 4.1 summarizes the calculated structural and energetic properties of the superoxide phases examined here. These include: lattice parameters a, b, c, O-O bond length, O_2 dimer orientation, the most stable magnetic phase, the energy difference between FM and AFM phases, and the distance between an alkali metal ion (Li, Na, K) and its nearest O atom. For LiO_2, the calculated lattice parameters are a = 4.01 Å, b = 4.78 Å and c = 3.04 Å, in good agreement with previous calculations using the HSE06 functional (a = 3.99 Å, b = 4.77Å and c = 3.01Å).[4] Ferromagnetic ordering (FM) was found to be more stable than Anti-Ferromagnetic ordering (AFM), with an

energy difference of 6 meV/f.u.. This is consistent with previous calculations that predicted FM ordering to be more favorable.[4]

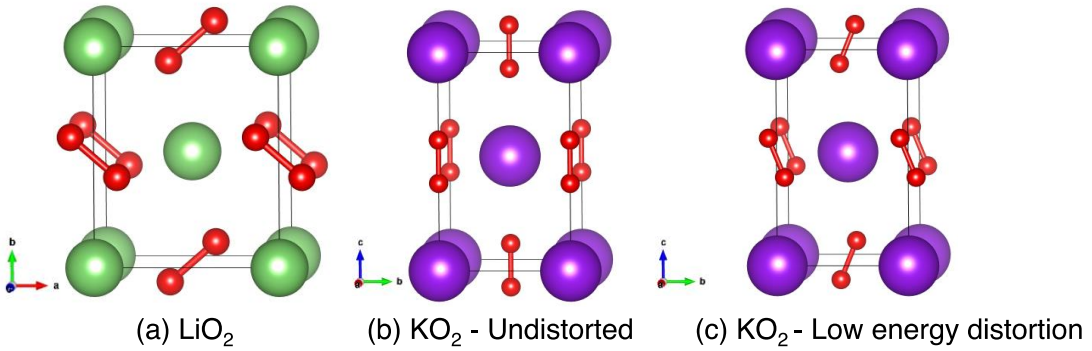

Figure 1.16 Crystal structures of (a) Orthorhombic LiO_2 (b) KO_2 (Precession) (c) KO_2 (High Symmetry Tetragonal). Red spheres represent oxygen atoms; Green spheres represent Li atoms; purple spheres are potassium atoms.

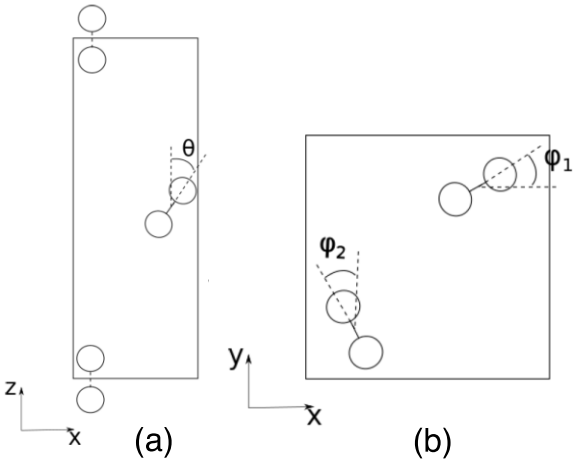

Figure 1.17 Precession model of KO_2 viewing from (a) [010] direction and (b) [001] direction. The O_2 rotation energy map with tetragonal constraint and keeping theta = 22°. Figure courtesy from Nicolai Rask Mathiesen.

The KO_2 phase calculated from the precession model has lattice parameters of a = 4.11Å, b = 4.11Å, c = 6.72Å, while the HST structure has a lattice parameters of a = 3.99Å, b = 3.99Å, c = 6.84Å. Both sets of lattice constants are in reasonably good agreement with the experimental values of a = 4.03Å, b = 4.03Å, c = 6.70Å.[27] FM ordering was found to be more stable than AFM ordering, with a 2meV/formula unit energy difference. This is consistent with previous DFT calculations, which used GGA + U with U values from 3 to 6 eV. In those calculations the FM-AFM energy difference was in the range of -3 to -1 meV/f.u..[24]

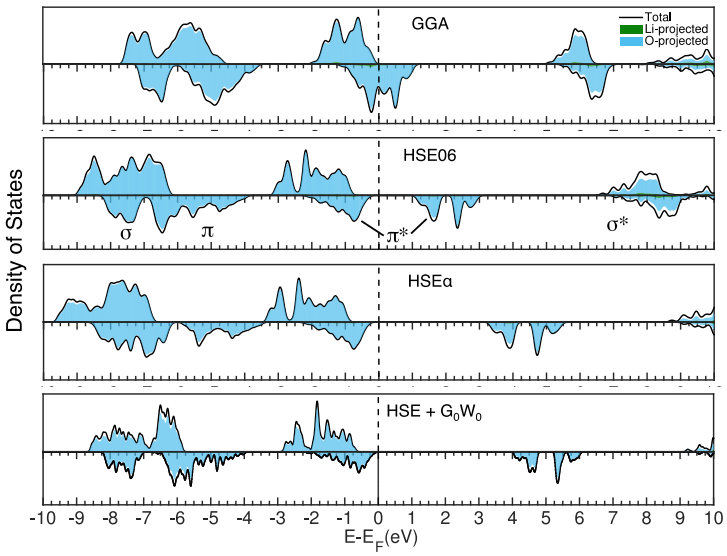

Figure 1.18 Density of states (in arbitrary units) plots for bulk LiO_2 calculated using four different methods: (from top to bottom) GGA, HSE06, HSE ($\alpha = 0.48$) and HSE+G_0W_0.

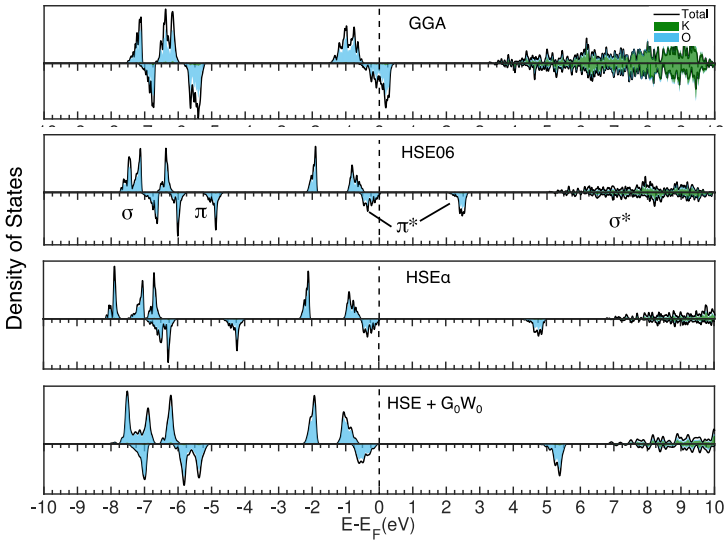

Figure 1.19 Density of states (in arbitrary units) plots for bulk KO_2 calculated using four different methods: (from top to bottom) GGA, HSE06, HSE ($\alpha = 0.48$) and HSE+G_0W_0.

Figure 4.3 and Figure 4.4 show the calculated projected Density of States (DOS) at different level of theory for LiO_2 and KO_2, respectively. The energy zero in these plots was aligned such that the energy of the valence band maximum is set to zero. From energy -10 eV to 6 eV, the DOS was mainly comprised of oxygen states, with little state density on the alkali metal ions. These results, including our previous calculations on NaO_2, imply that alkali

superoxides, which consist of alkali metal ions (M^+) and superoxide dimers (O_2^-), are highly ionized crystals. In the case of the semilocal GGA functional, LiO_2 and KO_2 are predicted to have half-metallic behavior, showing no bandgap, which is in agreement with similar calculations in the literature.[18,28] In contrast, use of the HSE functional opens a bandgap in both compounds by splitting the π^* states. A better estimate of the bandgap can be determined by the non-self-consistent G_0W_0 approximation using the HSE06 wavefunction as input. Convergence tests were performed with respect to the number of empty bands; a total of 512 bands were used for all G_0W_0 calculations. The HSE + G_0W_0 data indicates that LiO_2 has a bandgap of 4.16 eV, close to the result of 4.02 eV by Li *et al.*[4] It also predicts that KO_2 has a bandgap of 4.95 eV, suggesting that KO_2 is a wide bandgap insulator.[24,25] We believe the HSE + G_0W_0 calculations provide the most accurate of the bandgaps of these compounds.

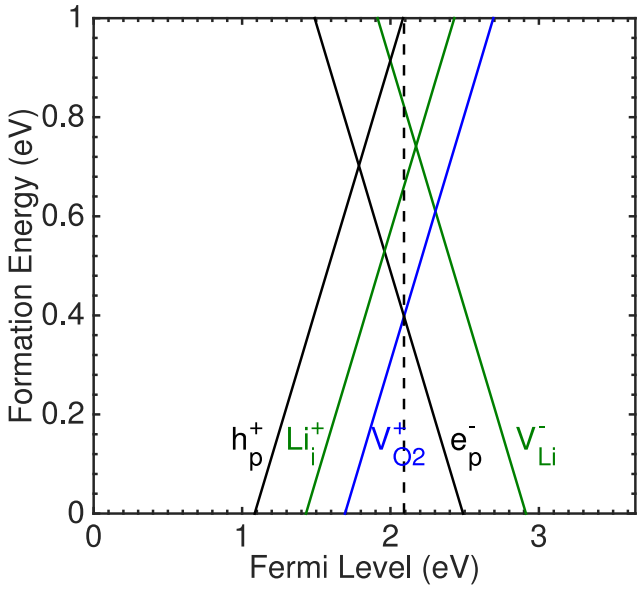

Figure 1.20 Defect formation energy of the O vacancy, Li vacancy and interstitials, electron polarons and hole polarons obtained using the HSEα (α = 0.48) hybrid functional in LiO_2.

4.3.2 Intrinsic Defects in LiO_2

Figures 4.5 and 4.6 show the calculated defect formation energies in LiO_2 and KO_2, respectively. The slope of the each line indicates the charge state for the respective defect species: a positive (negative) line indicates a positively (negatively) charged defect. The zero of the x-axis corresponds to the valence band maximum (VBM), while the maximum value represents the conduction band minimum (CBM). The vertical dotted line at 2.1 eV gives the position of the Fermi energy, which is established by the charge neutrality condition. We note that in the present study, the defect formation energies were calculated under equilibrium condition, whereas in actual batteries, these concentrations may not be realized due to non-equilibrium effects. It is possible that the actually defects concentrations are much higher than our equilibrium predictions. Therefore, our predicted defects concentrations represent lower bounds.

Table 4.2 Defects formation energies (**E_f**) and concentrations (**C**) in LiO_2

Defects	E_f (eV)	C (cm^{-3})
e_p^-	0.40	7×10^{15}
h_p^+	1.00	5×10^{5}
V_{Li}^-	0.82	6×10^{8}
V_{O2}^+	0.40	7×10^{15}
Li_i^+	0.66	6×10^{11}

The dominant charged defects in LiO_2 are positive oxygen dimer vacancies, V_{O2}^+, and electron polarons, e_p^-, the latter localized on oxygen dimers. The respective formation energies are 0.40 and 0.40 eV. Table 4.2 summarizes the equilibrium concentrations for all defects considered. The concentrations of V_{O2}^+ and e_p^- are estimated to be 7×10^{15} cm^{-3}, which are about 8 orders of magnitude greater than the reported value in Li_2O_2.[1] The predicted concentration of V_{O2}^+ in LiO_2 is close to that for the same defect species in NaO_2 reported in our previous calculation[8], 9×10^{14} cm^{-3}. Our findings for LiO_2 differ from those recently reported by Li *et al.*[4] They found that the dominant defect species in LiO_2 are h_p^+ and V_{Li}^- with concentrations of 1×10^{13} cm^{-3}. This difference can be explained by Li *et al.'s* use of a different estimate for the

oxygen chemical potential: They used the total energy for oxygen at zero kelvin as the oxygen chemical potential, neglecting pV contributions and contributions from the experimental entropy.

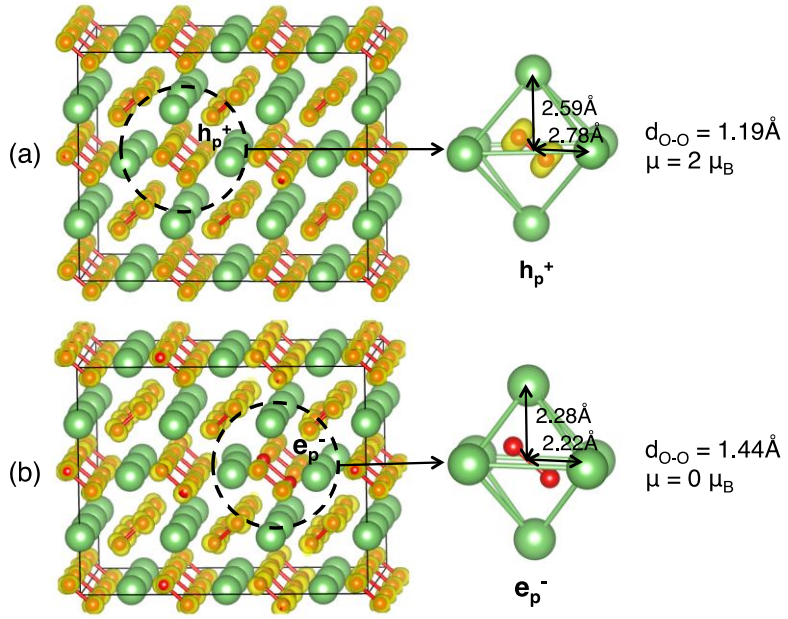

Figure 1.21 Magnetization density distribution for (a) hole and (b) electron polarons in LiO_2. (c) Structural and magnetic properties of O−O dimers with different charge states. The isosurfaces represent the spin density at the value of 0.04 e $Bohr^{-3}$

In LiO_2, a hole (electron) polaron consists of a missing (additional) electron localized on an O_2 dimer, resulting in a distortion of the lattice (Figure 4.6): The O−O dimer bond length and the distance between the O_2 dimer hosting the polaron and the nearest neighbor lithium atoms become distorted. In pristine LiO_2 the oxygen dimers sit in the center of octahedral formed by lithium ions. For an electron polaron in LiO_2 the O-O bond length expands from 1.30 to 1.44 Å, the latter value being slightly smaller to that of peroxide O_2 dimers in Li_2O_2 (1.48 Å). Each octahedron has two distinct O_2-Li bond distances. The six neighboring lithium atoms are attracted by the added electron, leading to the contraction of the O_2-Li distances from 2.52/2.39 Å to 2.28/2.22 Å. Moreover, the added electron fills a $\pi_{x,y}^*$ orbital, making that orbital fully occupied. Subsequently, the magnetic moment on this dimer disappears, while it remains 1μ_B for the rest of O_2^{1-} ions in the supercell (Figure 4.6b) that do not host a polaron. We note that the formation energy of an electron polaron in LiO_2 (0.40 eV) is much lower than in Li_2O_2, 3.12 eV.[1]

This may be explained by the fact that in LiO_2 an electron polaron occupies a $\pi_{x,y}^*$ orbital, whereas in Li_2O_2 it must occupy a higher energy σ^* orbital.

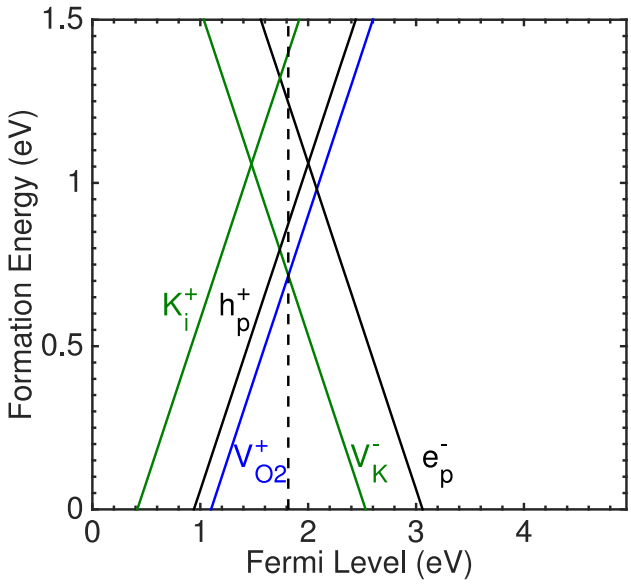

Figure 1.22 Defect formation energy of the O vacancy, K vacancy and interstitials, electron polarons and hole polarons obtained using the HSEα (α = 0.48) hybrid functional in KO_2.

Regarding hole polarons in LiO_2, our calculations indicate that these missing electrons also localize on O_2 dimers, resulting in a decrease of the O-O bond length from 1.30 to 1.19 Å. The six neighboring lithium atoms at the O_2-Li octahedron vertices are repelled by the additional positive charge, leading to the elongation of the O_2-Li distances from 2.52/2.39 Å to 2.59/2.78 Å. A hole polaron transforms a superoxide dimer, O_2^{1-}, into a neutral state, O_2^0; identical to that of gaseous O_2. Similar results were found in previous work by Li *et.al.*[4] and in our previous calculations on NaO_2.[29] The magnetic moment on the dimer hosting the hole polaron, $\mu = 2\ \mu_B$, is twice as large as in the peroxide (Figure 4.6a), and is consistent with that observed for gas phase O_2: the trapping of a hole on an O_2 dimer results in two unpaired electrons in the $\pi_{x,y}^*$ orbital, with each electron contributing a magnetic moment of $1\mu_B$.

4.3.3 Intrinsic Defects in KO_2

Figure 4.7 shows the calculated defect formation energies in KO_2 as a function of the Fermi level. The predominant defect species, i.e. the defects with the lowest formation energies, are the negatively charged potassium vacancy (V_K^-), and the positively charged oxygen dimer vacancy (V_{O2}^+), both having formation energies of 0.72 eV. Table 4.3 summarizes the concentrations for all defects considered. The equilibrium concentrations of V_{O2}^+ and V_K^- are estimated to be 2×10^{10} cm^{-3}, which are about 5 orders of magnitude smaller than for the same defect types in NaO_2 and 6 orders smaller than in LiO_2.

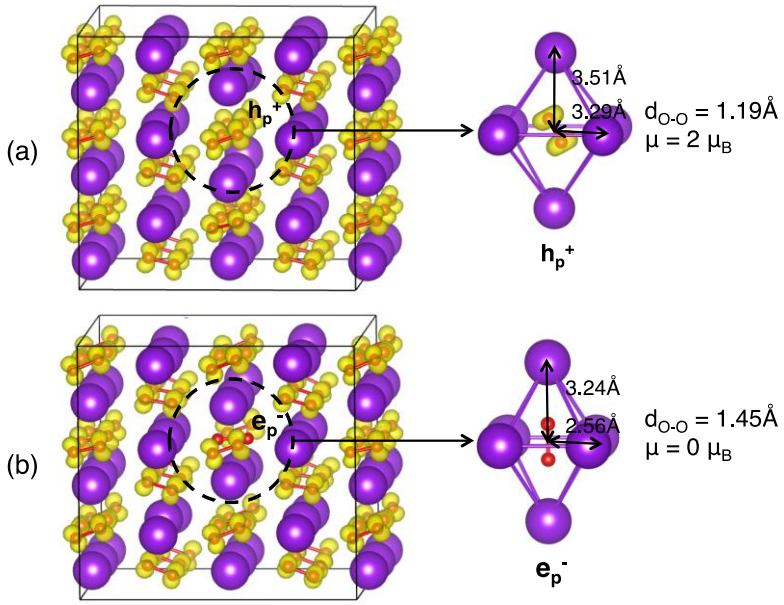

Figure 1.23 Magnetization density distribution for (a) hole and (b) electron polarons in KO_2. (c) Structural and magnetic properties of O−O dimers with different charge states. The isosurfaces represent the spin density at the value of 0.04 e $Bohr^{-3}$.

Table 4.3 Defects formation energies ($\mathbf{E_f}$) and concentrations ($\mathbf{C}$) in KO_2

Defects	E_f (eV)	C (cm^{-3})
e_p^-	1.24	2×10^1
h_p^+	0.88	4×10^7
V_K^-	0.72	2×10^{10}
V_{O2}^+	0.72	2×10^{10}
K_i^+	1.40	6×10^{-2}

Like LiO_2 and NaO_2, in KO_2 the electronic conductivity is mediated by polarons localized on O_2 dimers. The formation energy of a hole polaron in KO_2 (0.88 eV) is lower than for the electron polaron, 1.24 eV. These formation energies result in an equilibrium concentration of 4×10^7 cm^{-3} and 2×10^1 cm^{-3}, respectively. For hole polarons in KO_2, missing electrons localize on O_2 dimers, resulting in a decrease of the O-O bond length from 1.30 to 1.19 Å, and increase of d(K-O_2) from 2.91/3.36 Å to 3.29/3.51 Å. The hole polaron remove one electron from $\pi_{x,y}^*$ orbital, making that orbital half occupied and a magnetic moment of $\mu = 2\mu_B$. As for an electron polaron in KO_2, the O-O bond length expands from 1.30 to 1.45 Å, accompanied with decrease of d(K-O_2) from 2.91/3.36 Å to 2.56/3.24 Å. Moreover, the oxygen with the electron polaron rotates 22° around x-axis, leading to the dimers parallel with the z-axis. The overall geometry change coincides with a change in magnetic moment to $\mu = 0$ μ_B, where the $\pi_{x,y}^*$ orbital now is fully occupied.

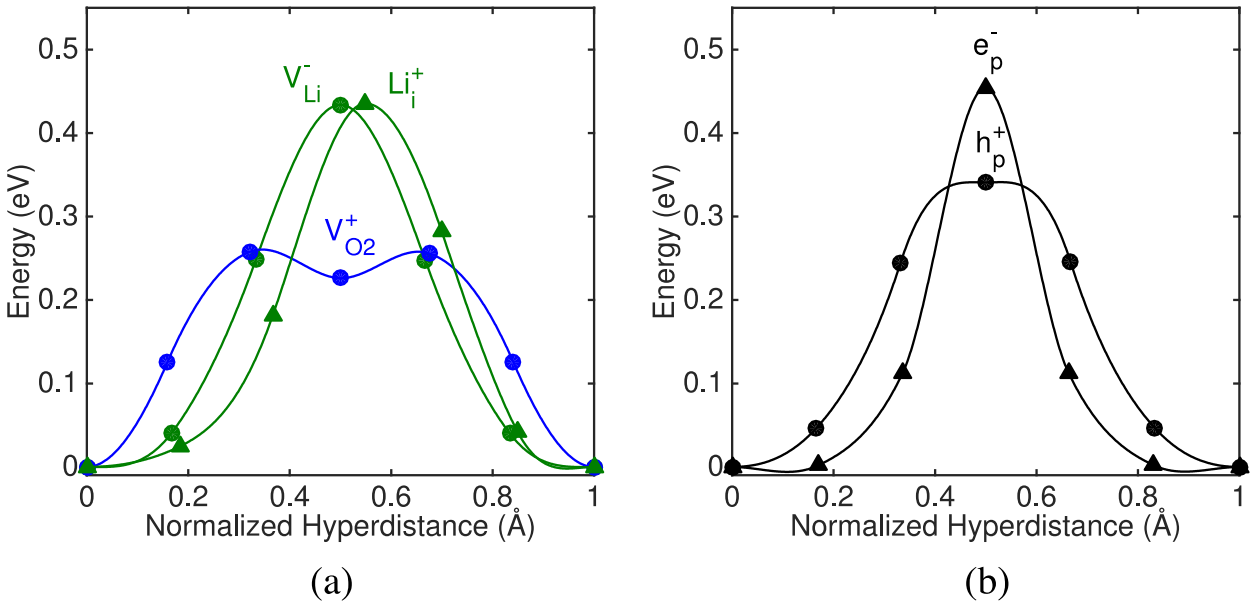

Figure 1.24 Energy barriers calculated using the NEB method for (a) ionic charge carriers and (b) polarons in LiO_2. Blue curves refer to positive lithium interstitials (Li_i^+), green curves represent negative potassium vacancies (V_{Li}^-), and black curves are polarons (e_p^-, h_p^+)

4.3.4 Defect mobilities

The second quantity needed to estimate the conductivity of LiO_2 and KO_2 is the mobilities of the predominant charge-carrying species. We first consider the mobilities of ionic species. In LiO_2, ionic conductivity originates from the migration of negative lithium vacancies, V_{Li}^-, positive oxygen vacancies, V_{O2}^+ and positive lithium interstitials. For each species, there are three symmetry distinct pathways. Li *et al.* proposed that the migration barriers had a positive relationship with the length of diffusion path; therefore, we constrain our calculation to the shortest hopping pathway, i.e., migration along the z-axis. The calculations suggest that all of these defects have modest migration barriers (Figure 4.9a). The calculated barriers for V_{Li}^-, Li_i^+ and V_{O2}^+ are 0.43, 0.43 and 0.26 eV, respectively, corresponding to diffusion coefficients of 5×10^{-10}, $2\times10^{-10,}$ and 4×10^{-7} $cm^2\,s^{-1}$. Migration of the negative lithium vacancy occurs via a pathway where the vacancy hops from one vertex of a distorted Li-ion octahedron to a nearest-neighbor vertex. The calculated energy barrier for this process, 0.43 eV (Figure 4.9a), is much smaller than the average barrier for vacancy migration in Li_2O_2,[1] which has a barrier 0.93~0.95 eV. The diffusion of an O_2 vacancy is accompanied by the migration of an O_2 dimer in the opposite direction. Although the O_2 dimers before and after O_2 vacancy migration are parallel, a 90° rotation occurs during the migration process, leading a V-shaped energy profile, similar to that in NaO_2.[8] The O−O bond does not break during the migration.

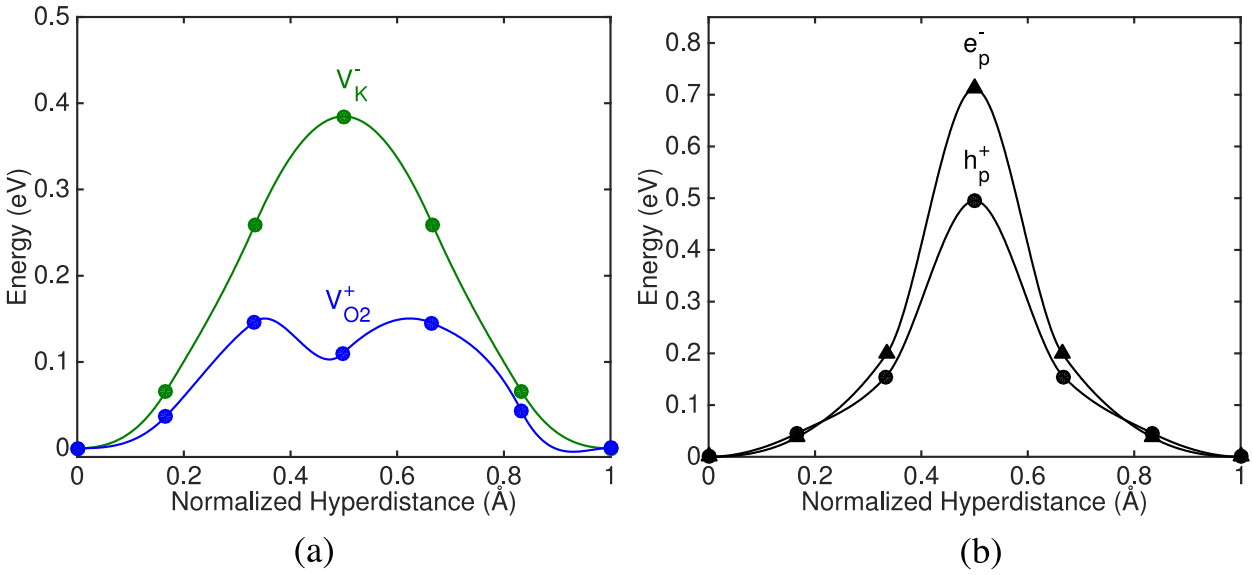

Figure 1.25 Energy barriers calculated using the NEB method for (a) ionic charge carriers and (b) polarons in KO_2. Blue curves refer to positive potassium interstitials (K_i^+), green curves represent negative potassium vacancies (V_K^-), and black curves are polarons (e_p^-, h_p^+).

Regarding defect mobilities in KO_2, we examine the mobilities of ionic species having the highest concentrations. In KO_2, ionic conductivity originates from the migration of negative potassium vacancies, V_K^- and positive oxygen vacancies, VO_2^+. For each species, there are two symmetry distinct pathways: intralayer (along [100] or [010]) and interlayer (along [111]) migration. For negative potassium vacancies, the intralayer migration along the short path is more favored. It occurs via a single hop from one vertex of a K-ion octahedron to a nearest-neighbor vertex. The calculated energy barrier for this process, 0.38 eV (Figure 4.10a), is larger than that in NaO_2, 0.35 eV, but lower than in LiO_2, 0.42 eV. This corresponds to diffusion coefficients of 7×10^{-9} cm^2 s^{-1}. For the positive O_2 vacancy, the interlayer migration is more favored than intralayer migration. The oxygen dimers in the same layer are parallel, while oxygen in the interlayer path have orientations that differ by 44°. The translation of an O_2 dimer in the opposite direction accompanies the intralayer migration of a vacancy. In contrast, interlayer vacancy migration is accompanied by the rotation and translation of an O_2 dimer, leading to a V-shaped migration pathway, similar to what is observed in LiO_2 and NaO_2.[8] No break rupture or significant change to the O−O bond is observed during this migration. The migration barriers for "V_{O2}^+" is 0.15 eV (Figure 4.10), corresponding to diffusion coefficients of 5×10^{-5} cm^2 s^{-1}. The exceptionally low migration barrier for positive O_2 vacancies results in faster

migration of these vacancies than in LiO_2 and NaO_2. Regarding the mobilities of electronic species, in KO_2, the calculated barrier for migration of an electron polaron, 0.71 eV, is higher than that for migration of a hole polaron, 0.50 eV. These barriers are similar to our previous calculations of NaO_2, Na_2O_2 and Li_2O_2.[1,8]

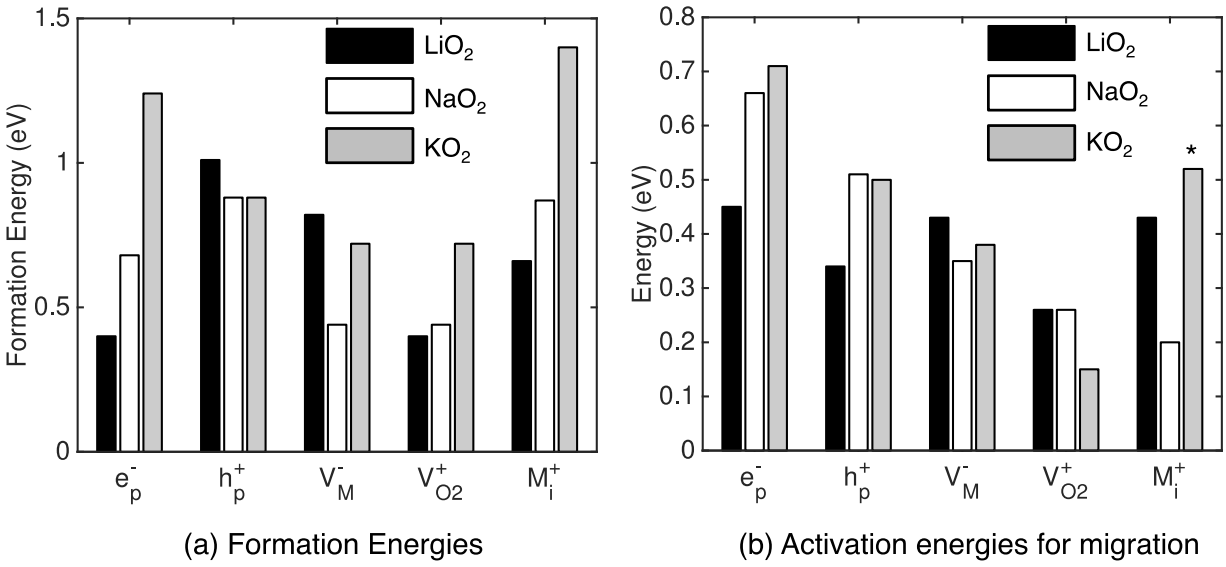

Figure 1.26 Bar plot of different defects (a) formation energies and (b) migration barriers for LiO_2 (white), NaO_2 (black) and KO_2 (grey).
* K_i^+ migration barriers undergo a disordering intermediate structure.

4.3.5 Superoxides Comparison

Figure 4.11 shows a histogram plot of (a) the formation energies and (b) migration barriers for in LiO_2 (white), NaO_2 (black)[8] and KO_2 (grey). These plots allow us to see that V_{O2}^+ defects have the lowest formation energies in all of the superoxides (Figure 4.11a). This is in good agreement with Gerbig *et al.*'s experimental measurements, where they found perceptible concentration of oxygen vacancies in superoxides. LiO_2 and NaO_2[8] have similar lowest energy defect formation energies, while KO_2 have higher defects formation energies than those in LiO_2 and NaO_2[8]. The concentrations of defects are dependent on the chemical potentials of electrode, specifically, the O_2 partial pressure and applied potential, whereas the mobilities of the defects are more of intrinsic properties for materials. For electron polarons and hole polarons (Figure 4.11b), LiO_2 shows the smallest polaron hopping barriers, NaO_2 falls in between, and KO_2 has slightly higher

barriers than NaO_2. The change of barrier height seems to be related to the hopping distances, as the hopping distances of LiO_2, NaO_2 to KO_2 are 3.03, 3.83, and 4.11 Å, respectively, showing an increasing trend of the hopping distances. The migration barriers for negative metal vacancies have small differences among superoxides. As for positive oxygen dimer vacancies, LiO_2 and NaO_2 have the same migration barriers, 0.26 eV, whereas KO_2 has a smaller barrier, 0.15 eV. The small barriers of O_2 vacancy migration implies fast O_2^+ diffusion in superoxides, and agrees well with Gerbig *et al.*'s experimental measurements, where they found high mobilities of O_2 in KO_2.[10]

4.3.6 Conductivity

The calculated equilibrium conductivities for LiO_2 and KO_2 are summarized in Table 4.4 and Figure 4.12, and compared with prior calculations on Li_2O_2, NaO_2 and Na_2O_2. Turning first to LiO_2, our calculations suggest that the ionic and electronic conductivities of LiO_2 are 4×10^{-9} and 9×10^{-12} S/cm, respectively. These values are much larger to that of Li_2O_2, with the ionic and electronic conductivity 10 orders and 8 orders higher, respectively.

Table 1.4 Calculated dominant defects and (ionic + electronic) conductivities (S cm^{-1}) for LiO_2 and KO_2, and their comparison with prior calculations on Li_2O_2,[55] Na_2O_2 and NaO_2.

Compound	Ionic Conductivity (S/cm)	Electric Conductivity (S/cm)	Dominant species
LiO_2	4×10^{-9}	9×10^{-12}	e_p^-, V_{O2}^+
Li_2O_2	9×10^{-19}	5×10^{-20}	e_p^-, h_p^+, V_{O2}^+, V_{Na}^-
NaO_2	4×10^{-9}	1×10^{-19}	h_p^+, V_{O2}^+
Na_2O_2	5×10^{-20}	1×10^{-20}	h_p^+, V_{Li}^-
KO_2	5×10^{-12}	1×10^{-20}	h_p^+, V_{Na}^-

Regarding to KO_2, the ionic conductivity is mainly contributed by positive oxygen vacancies, with calculated conductivity of 5×10^{-12} S/cm, three orders lower than LiO_2 and NaO_2, but 8 orders higher than in Li_2O_2 and Na_2O_2. Our results are consistent with the conclusions reached by Gerbig *et al.,* who measured ionic conductivities of the heavier alkali-metal superoxides (KO_2, RbO_2 and CsO_2.) at 200 ℃, and extrapolate a room temperature ionic

conductivity of ~10^{-13} S/cm. Their ^{18}O isotope Exchange experiments showed that the oxygen transport through KO_2 was based on the migration of intact oxygen dimers, and this migration contributes to the ionic conductivity. The predicted electronic conductivity is of KO_2 is 10^{-20} S/cm, similar to that of Li_2O_2,[1] suggesting that electronic transport through pristine KO_2 will be negligible, unless pathways coupled to microstructural features (surfaces, grain boundaries, amorphous regions, *etc*.) contribute. Our results are consistent with the conclusions reached by Gerbig *et al.,* because they found that electronic conductivities of KO_2 were comparable to those of Li_2O_2.[31]

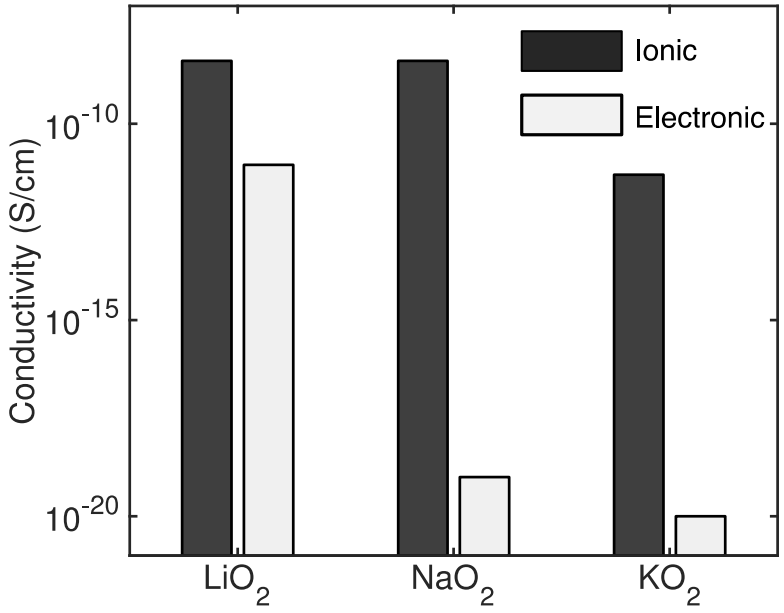

Figure 4.13 Bar plot of ionic (black) and electronic (gray) conductivities (in log scale) for LiO_2, NaO_2 and KO_2.

We focus the remainder of our discussion on conductivity in all superoxides. The main charge carriers in Li_2O_2 and Na_2O_2 are negative alkali metal vacancies and (positive) hole polarons. As for the case of superoxides, the main charge carriers are polarons and positive oxygen dimer vacancies. In the context of electronic conductivities, LiO_2 has the highest electronic conductivities, whereas conductivities of other peroxides and superoxides are 7~8 orders lower. The low electronic conductivities found in KO_2 and NaO_2 suggests that low overpotentials in superoxide-based batteries cannot be explained by the high electronic conductivities of KO_2 and NaO_2. However, in practical batteries the defects concentrations could

be much higher than the values in the present study, resulting much higher electronic conductivities that can lead to low charging overpotentials. As for ionic conductivities, all of the superoxides have much higher ionic conductivities than do the peroxides, and these mostly originate from high concentrations and mobilities of positive oxygen dimer vacancies.

4.4 Conclusion

A combination of density functional and quasi-particle calculations have been used to characterize charge transport in the superoxide discharge products observed in Li-O_2 and K-O_2 batteries. Higher conductivity within the LiO_2 and KO_2 phase has been proposed to explain why cells that discharge to LiO_2 and KO_2 exhibit much lower charging overpotentials. The present study tests this hypothesis by calculating the intrinsic conductivity of these phases. Our calculations reveal that both bulk LiO_2 and KO_2 are wide bandgap insulators, and not half-metals. Rather, charge transport in these phases will occur via the hopping of localized carriers such as ions or polarons. Polarons are predicted to localize on oxygen dimers.

In the case of potassium superoxide, the transport properties are remarkably similar to our previous reports for sodium superoxide, suggesting low electronic conductivity on the order of 10^{-20} S/cm, and a higher ionic conductivity on the order of 10^{-12} S/cm. The limited electronic conductivity predicted for KO_2 suggests that bulk transport within this phase is unlikely to explain the low overpotentials associated with its decomposition during charging in a K/O_2 electrochemical cell.

In the case of lithium superoxide, polarons exhibit low-to-moderate hopping barriers for electrons and holes, with values of 0.34 and 0.45 eV, respectively. We find that the electronic conductivity is mainly contributed by electron polarons, and is around 8 orders of magnitude higher than that in Li_2O_2, which may help justify the experimentally observed low overpotential of the Li-O_2 cells with presence of LiO_2.

By comparing with our previous work on NaO_2, we note that a distinguishing feature of the alkali metal superoxides is that the ionic component of conductivity is comprised primarily by positive oxygen dimer vacancies. The mobility of oxygen dimers in the KO_2 lattice is consistent with a recent experimental study by Gerbig *et al*., who found that superoxide ions are highly mobile in KO_2, RbO_2 and CsO_2. [10]

Chapter 5: Crossover of Transition Metal Impurities Impedes Li-ion Transport in the Solid Electrolyte LLZO

5.1 Introduction

The garnet with composition $Li_7La_3Zr_2O_{12}$ (LLZO) is regarded as a highly promising solid electrolyte, batteries due to its chemical stability against Li metal, and electrochemical stability (0−6 V vs Li/Li+).[16] The cubic phase of LLZO (Figure 5.1) exhibits a room temperature ionic conductivity up to 2×10^{-4} S cm^{-1}. In undoped LLZO the cubic phase is unstable at temperatures below ~630 °C, and will transform to the thermodynamically stable tetragonal phase (space group I4/acd). The tetragonal phase exhibits a relatively low Li-ion conductivity at room temperature.[24] Doping with supervalent cations such as Al^{3+} and Ga^{3+} on the Li-sublattice,[25,26] or with Nb^{5+}, Te^{6+} and Ta^{5+} on the Zr-sublattice,[27–29] stabilizes the cubic phase at room temperature. The density of the solid electrolyte membrane is another important factor in achieving high ionic conductivity and suppressing dendrite formation.[170] For example, hot-pressing/sintering at temperatures and pressures in the range of 1300 K and 60 MPa is commonly used to increase the relative density of LLZO pellets, with values as high as 99% reported.[171,172]

In this chapter, we use a combination of experimental and computational techniques to characterize transition metal cross over from a Li-ion cathode to a solid electrolyte. The LCO/LLZO interface is adopted as a model system. We assess the extent of Co cross over, the location of Co in the LLZO lattice, and the impact on Li-ion transport arising from the presence of Co impurities in LLZO. Hot-pressing of LLZO and LCO pellets resulted in a color change in LLZO from white to blue in regions proximal to the LLZO/LCO interface. This color change coincides with the diffusion of Co from LCO to LLZO; the Co concentration as a function of position from the interface was quantified at different processing temperatures using electron probe micro-analysis. Raman spectra suggest that the Co occupies sites within the Li-sublattice of LLZO. Classical molecular dynamics simulations were used to investigate the transport rates

of Co and three other transition metals (Mn, Fe, Ni) that are commonly used in Li-ion cathodes. We find that Fe impurities are the most mobile of the four TMs investigated; nevertheless, all TMs exhibit lower diffusivities in LLZO compared to Li. The higher diffusivity of Fe can be explained by the higher number of active octahedron vacancy density.

The presence of TMs is shown to slow Li-ion migration, with the relative magnitudes of the slowing following the same trend as the TM diffusivities. Because the TMs also migrate along the Li-sublattice, these observations suggest that slower-moving TMs impede Li-ion migration via a traffic-jam-like process. Our work highlights a tradeoff associated with the synthesis of solid-solid LLZO/cathode interfaces: although high-temperature processing increases interfacial contact, and thus lowers impedance, the use of high temperatures also increases the likelihood for undesirable TM crossover from cathode to solid electrolyte, thereby increasing impedance.

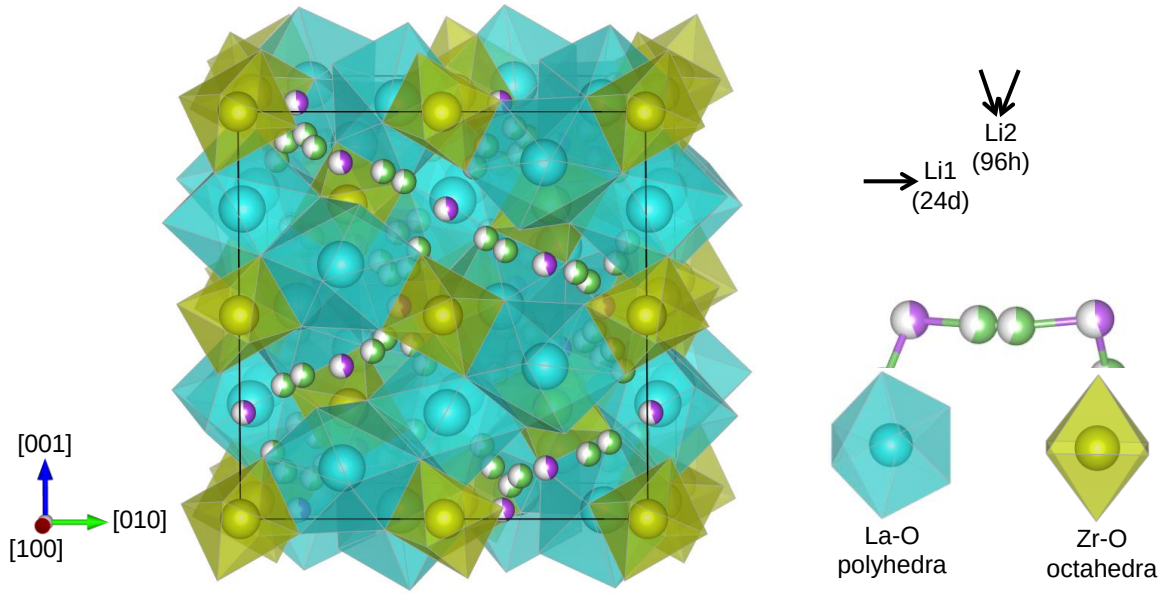

Figure 1.27 Cubic $Li_7La_3Zr_2O_{12}$ (cLLZO), illustrating La-O polyhedral, Zr-O octahedra, and the 3D ring structure formed by the partially-occupied Li sublattice. The ring structure contains two symmetry-distinct Li sites: Li1(purple, tetrahedral coordination, 24d) and Li2 (green, octahedral coordination, 96h).

5.2 Methodology

5.2.1 Computational models for LLZO.

Figure 5.1 shows the cubic unit cell of LLZO. This compound crystallizes with space group $Ia\bar{3}d$ (No. 230), and exhibits partial occupancy on both the 24d Li (1) tetragonal sites and the 96h Li (2) octahedral sites. Our calculations adopted the experimental crystal structure, as reported in the literature.[23] The cubic unit cell contains 24 La atoms, 16 Zr atoms, 96 O atoms and 120 available Li sites, with 56 occupied by Li atoms.

Experiments show that the ionic conductivity and stability of the cubic phase both depend on the presence of Al, which is incorporated during synthesis.[171,172] Our calculations adopt the composition $Li_{6.25}La_3Al_{0.25}Zr_2O_{12}$ (LLAZO), which contains 2 Al ions per unit cell, with Al occupying sites within the Li sublattice. A recent NMR and first principles computational study argued that the site preference for Al was: Li 24d (tetrahedral site) > Li 96h (octahedral site) > Zr (16a) >> La (24c).[173] The ordering of Li and Al ions in LLZAO was revisited here using a sampling approach similar to that described in Ref. 14, wherein the location of Ga dopants in LLZO was determined. This approach aims to identify low-energy arrangements of Li ions, Li vacancies, and Al ions on the Li sublattice. The first step in the procedure is to generate symmetry-distinct arrangements of Al ions, assuming two Al per conventional cubic unit cell. The Al can in principle occupy 24d or 96h sites, however, given the small separation between adjacent 96h sites, these site pairs were treated as a single site (i.e., a 48g site). A total of approximately 100 symmetry-distinct Al orderings were generated. These configurations were ordered according to their electrostatic energies using Pymatgen,[174–177] with the 50 lowest-energy configurations promoted to the next step of the process. Next, these 50 structures were used as starting points for determining low energy arrangements for Li ions and Li vacancies (assuming fixed positions for Al). One hundred candidate structures were generated from each of the 50 input structures, for a total of 5000 candidates. The Li sites in each candidate were randomly filled with Li ions, to the appropriate stoichiometry. Finally, the total energy of all structures was minimized in LAMMPS with an appropriate interatomic potential (see details below). The

lowest energy structure was adopted at the 'pristine' LLAZO system in subsequent diffusion calculations.

For LLAZO models containing transition metal (TM) impurities, one to four TM ions were included in the LLAZO unit cell (188 atoms), with the number of Li atoms adjusted according to the stoichiometry and oxidation state of the added impurity. This range of TM inclusions results in atomic percentages of 0.5 to 2.2%, and were selected to be similar to the observed experimental concentrations. Transition metals used in common cathode materials were selected as impurities in LLZO: Co, Mn, Ni and Fe. Based on previous DFT calculations, Co, Mn, and Ni are predicted to reside on Zr sites, while Fe prefers the Li sublattice.[36] Our calculations considered more a more general scenario in which the TMs were placed either on the Zr sublattice or on the Li sublattice.

The lowest energy pristine LLAZO structure was used as a starting point for the generation of supercells containing TM impurities, via a procedure similar to that used to position Al ions. The lowest total energy structures were used in subsequent MD simulations. Additional details regarding the structure generation process are provided in the Supporting Information.

5.2.2 Molecular Dynamics Simulation.

NVE and NPT molecular Dynamics (MD) simulations were performed on 3×3×3 supercells of pristine LLAZO and on LLAZO containing TM impurities. All MD simulations were carried out using the LAMMPS package[138] with a timestep of 2 fs. Starting from the low-energy structures described above, the following heating schedule was used to prepare structures for diffusivity calculations: (i) 10 ps of NVE MD at 300 K, (ii) temperature ramping from 300 K to the target temperature (ranging from 700 to 1400 K) with an incrementing rate of 1 K per ps, and (iii) 1 to 30 ns of NPT MD at the target temperature. The external pressure for constant pressure ensembles was set to 1 atm. Atomic interactions were modeled with the long-range Columbic

potential and short-range Morse potential described by Adams et al.[135,178] The charge states adopted for the TMs were as follows: Co^{2+}, Ni^{2+}, Mn^{2+}, and Fe^{3+}.

5.2.3 Sample Preparation and Characterization.

Cubic LLZO with nominal composition $Li_{6.25}Al_{0.25}La_3Zr_2O_{12}$ was prepared using a solid-state synthesis method.[172] Li_2CO_3 (with 10 wt. % excess to compensate for Li loss in the following calcination process), $La(OH)_3$, ZrO_2 and Al_2O_3 precursors were stoichiometrically mixed in a 500 ml agate vial for 8 h at 400 rpm using a planetary mill (PM 100; Retsch, Germany). This precursor mixture was pressed into a pellet in a stainless steel die, calcined at 1000 °C in air for 4 h with the temperature ramped from room temperature at a rate of 100 °C h^{-1} and ground with a mortar and pestle to obtain fine LLZO powder. The calcined LLZO powder was pressed for 0.5 h at 63 MPa into a pellet with no heat applied, and then hot-pressed using an induction hot-pressing technique in Ar gas at 1100 °C for 0.5 h under constant pressure of 63 MPa.[170] A temperature of 1100 °C was reached (from room temperature) within 5 min and the cooling rate was ~20 °C/min. The resulting billet was >95% dense and was cut into disks using a diamond saw.

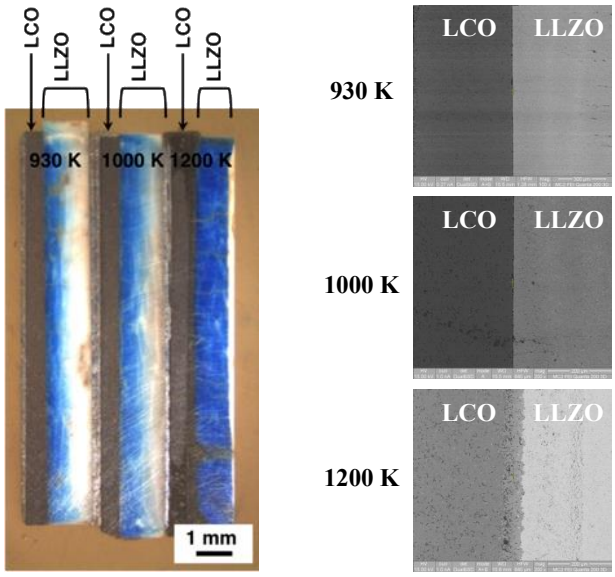

Figure 1.28 Optical (left) and SEM (right) images of the LCO/LLZO interface at three temperatures used for interface bonding. Figure courtesy from Woo-ram Lee.

Commercial LCO powder from MTI was used as received. An LCO disk (~99% relative density, ~1 mm thickness, 1/2 inch diameter) was prepared in a similar manner as that used for LLZO, except that the hot-pressing temperature was 900 °C. The resulting LCO billet was cut into disks using a diamond saw.

LLZO-LCO bilaminar structures were fabricated by diffusion bonding LLZO and LCO disks in the same induction hot-press. The bonding occurred at 1 MPa over a 30-minute duration. Four different temperatures were examined: 873, 930, 1000, and 1200 K. Compositional profiles were measured by electron probe micro-analysis (EPMA), with a focused beam, with an acceleration voltage of 15 kV, and a beam current of 20 nA.

Raman spectra were collected on a Renishaw inVia Raman Microscope using a 523 nm laser, 1800 lines/mm grating, 50 μm slit, and a RenCam CCD detector. Spectra was collected from 50-1500 cm^{-1}. Calibration was performed with a silicon standard. Spectra were normalized to the maximum value and N = 3 for each region were averaged.

5.2.4 Cobalt Diffusion Model.

The geometrical construction for modeling Co diffusion into LLZO comprised a constant cobalt source (taken as the Co concentration in LCO) and a semi-infinite LLZO plane. The initial t = 0 distribution is as follows:

$$C = C_0 (x < 0) \text{ and } C = 0\ (x > 0)$$

A solution to Fick's second law was employed to model the Co concentration, n_{Co}, as a function of diffusion time at a given temperature. The resulting cobalt distribution is given by:

$$n_{Co}(x,t) = n_{Co}(x=0) erfc\left(\frac{x}{2\sqrt{Dt}}\right). \quad (1.8)$$

Where $n_{Co}(x=0)$ is taken from averaging the cobalt concentration in LCO from x = -50 μm to x = 0 μm. D is the Co interdiffusion coefficient, and t is diffusion time. x = 0 corresponds to the LCO/LLZO interface.

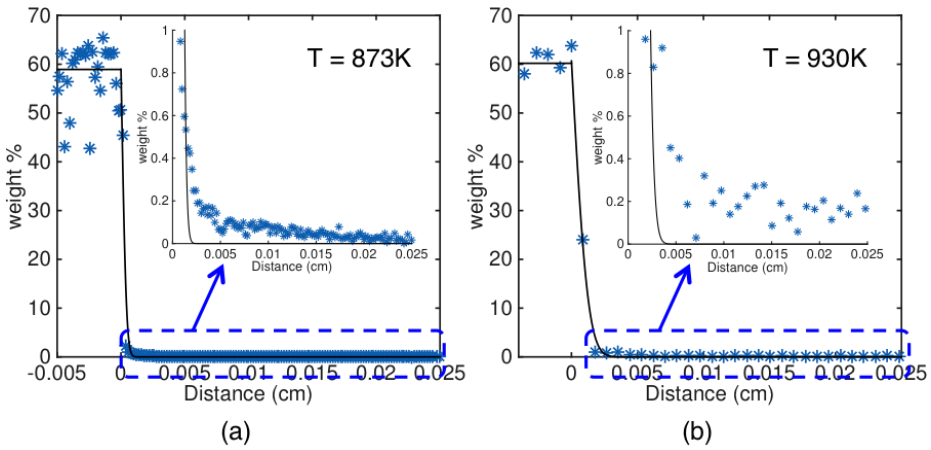

Figure 1.29 Co concentration as a function of temperature and of distance normal to the LCO/LLZO interface. Blue data points represent EPMA measurements, while solid lines depict the diffusion profiles obtained from fitting the data with Equation 5.1.

5.3 Results and discussion

5.3.1 Co Diffusion Across the LLZO/LCO Interface.

The $LiCoO_2$/LLZO bilayer samples sintered at different temperatures were mounted in cross-section and prepared for optical and SEM imaging by following metallographic polishing procedures. Figure 5.2 (right panel) shows SEM images of the samples processed at T = 930, 1000, and 1200 K. The two samples processed at the lower temperatures exhibit a sharp phase boundary at the interface between $LiCoO_2$ and LLZO. In contrast, the sample prepared at 1200 K does not exhibit a sharp boundary; rather, it appears a reaction layer with thickness of 70-80 μm has formed between the two compounds. The left panel of Figure 5.2 shows optical images of the same three bilayer samples. As shown there, LLZO undergoes a color change from white to blue upon heat treatment, with the blue-colored region of LLZO being adjacent to the interface with LCO. As the processing temperature increases, the blue region in LLZO widened and

darkened. As demonstrated below, this change in color results from the incorporation of Co impurities within LLZO, which had diffused from LCO during hot-pressing.

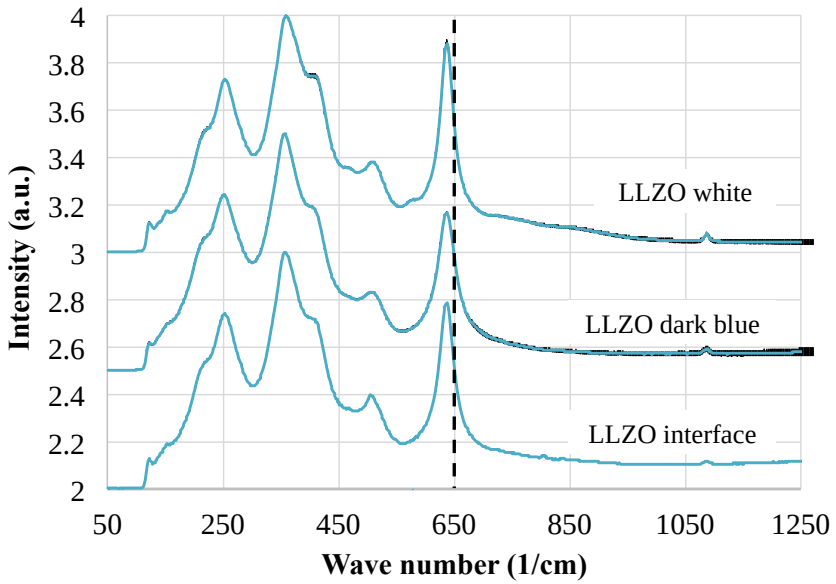

Figure 1.30 Raman spectrum of LLZO after diffusion bonding with LCO. The "interface" region corresponds to the LLZO a few microns away from the LCO, the "dark blue" region corresponds to the LLZO which was significantly blue approximately 50-100 microns away from the interface, and the "white" region corresponds to the LLZO which was furthest away from the interface and still white as the native LLZO. N=3 spectra were recorded in each region and averaged. The average along with the standard error ($\pm$ one standard devation / $\sqrt{N}$). Figure courtesy to Travis Thompson.

Figure 5.3 shows the cobalt concentration in LLZO after hot pressing at 873 and 930 K, as measured by EPMA. For both processing temperatures, the Co concentration exhibits a sharp initial drop at the LCO/LLZO interface, followed by a long tail that penetrates into the LLZO. For example, at 930 K the concentration of Co is ~0.2 wt. % at a distance of 250 μm from the interface. The resulting Co concentration profiles were fit to the solution of Fick's 2nd law, Eq. 1. The modeled Co concentration is overlaid onto the EPMA data in Figure 5.3. We note that the limited number of EPMA data points in the immediate vicinity of the interface, and the scatter evident in the data (even far from the interface), present challenges to achieving a precise fit to the data. Consequently, the resulting diffusion coefficients are best interpreted as a qualitative measure of Co diffusion in LLZO. The resulting diffusivities are: 6×10^{-10} cm^2 s^{-1} at 930K and 8×10^{-11} cm^2 s^{-1} at 873 K.

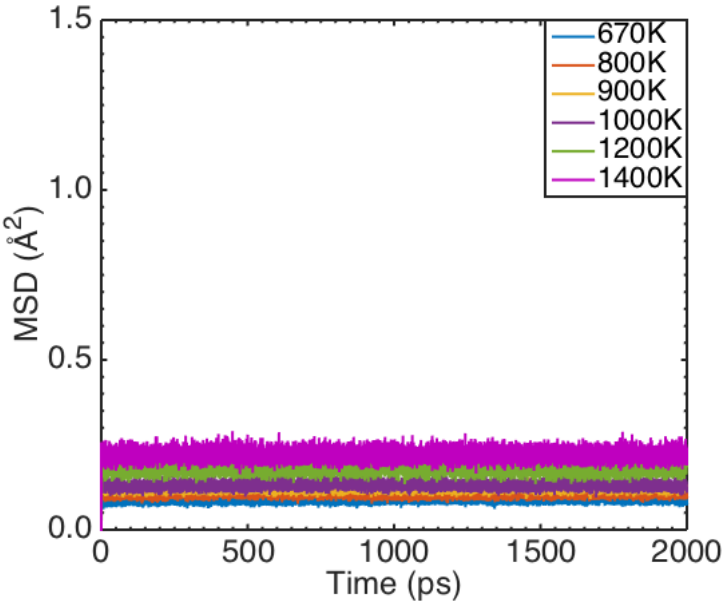

Figure 1.31 Mean Square Displacement (MSD) plots (670 – 1400 K) of Co atoms taken from 2 ns NPT MD simulations for x = 0.5 in $Li_{6.25}Al_{0.25}Co_xLa_3Zr_{2-x}O_{12}$.

There are no experimental observations available in the literature for which sites TM impurities favor upon incorporation into LLZO. As previously described, Miara *et al.* used DFT[36] to evaluate formation energies for the substitution of Fe, Co, Mn, and Ni into LLZO. The most stable substitution sites identified for Co, Mn, and Ni were Zr sites, while for Fe the most stable sites were on the Li sublattice. Previous work has shown that Ta substitution on the Zr sublattice in LLZO can be observed by Raman spectroscopy.[179] DFT calculations and experiments demonstrate that the band near 640 cm^{-1} corresponds to the breathing mode of oxygen atoms coordinated with Zr. This band is sensitive to bond length. When an atom is partially substituted on the Zr site, the band will shift in energy, with the peak intensity correlated with the degree of substitution. Raman measurements (Figure 5.4) performed on the present LLZO membranes (that were interfaced with LCO,) show no band shift near 640 cm^{-1}, suggesting that Co does not substitute on Zr sites. In addition, our own molecular dynamics calculations reveal that TM impurities substituted on Zr sites are essentially immobile (even at elevated temperatures), Figure 5.5. Nevertheless, EPMA and optical microscopy indicate that Co from LCO diffuses into LLAZO (Figure. 5.2-5.3). This implies that cross over of Co into LLZO could occur if Co were to instead occupy La or Li sites. Regarding La sites, earlier simulations[180] have shown that La framework cations are very slow diffusers – at odds with the present

experimental data – thus ruling out Co occupation of La sites. Taken together, these data imply that Co diffusion in LLZO occurs via the Li sublattice.

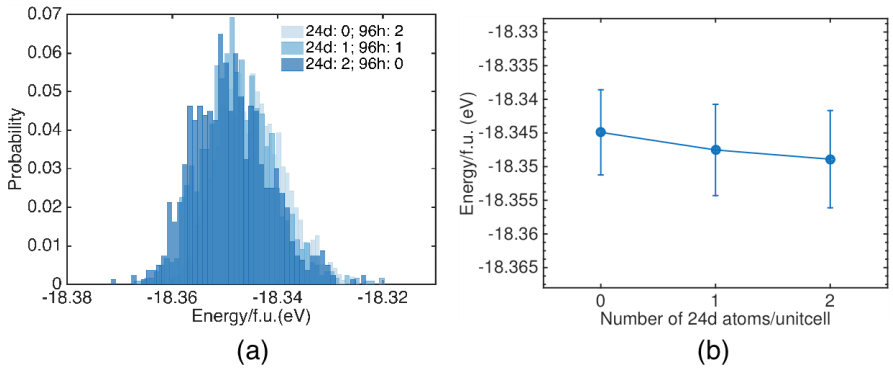

Figure 1.32 (a) Energy Distribution and (b) standard deviation of Al doped LLZO with two Al atoms on all 24d sites; one on 24d, one on 96h; two on 96h sites, respectively.

5.3.2 Low-Energy LLZO Structures.

Figure 5.6a shows histograms of the total energies associated with the different configurations of Al and Li ions in LLAZO. We reiterate that the doping level examined corresponds to two Al ions per conventional unit cell. These two ions can occupy either of (i.) two 96h sites, (ii.) one 96h site and one 24d site, or (iii.) two 24d sites. Separate histograms are plotted in Figure 5.6 for each of these three possibilities, with each histogram illustrating the energy spread associated with different arrangements of the Li ions for the specified Al ordering. In all of these cases, the width of the distribution is very narrow, corresponding to a standard deviation of only 0.5 meV/atom. This implies that the total energy is not strongly dependent on the distribution of Li ions (i.e., there is little energy difference between an ordered Li arrangement and a disordered one.) The lowest energy configuration overall corresponds to both Al ions occupying 24d sites. This conclusion is in good agreement with prior NMR and DFT calculations showing that Al dopants prefer to occupy 24d sites in LLZO.[173] Nevertheless, Figure 5.6b shows that on average the energy penalties associated with Al occupation of 96h sites (cases ii. and iii.) are very small.

Figures 5.7-5.8 show energy histograms generated from different configurations of TMs and Li ions in LLAZO, assuming the Al ions occupy the low energy 24d sites identified above. Similar to our observation for Al ordering, the total energy of these systems is not strongly dependent on the distribution of Li ions. For Co, Mn, and Ni impurities, the lowest energy

configuration places the TM ions in 96h sites. The situation is different, however, for Fe, where three quarters of the ions favor 24d sites, with the remainder in 96h sites. Nevertheless, the energy penalty associated with deviating from this low-energy ordering is small (less than 1 meV/f.u.), suggesting that the TMs will be disordered over the 24d and 96h sites at moderate temperatures.

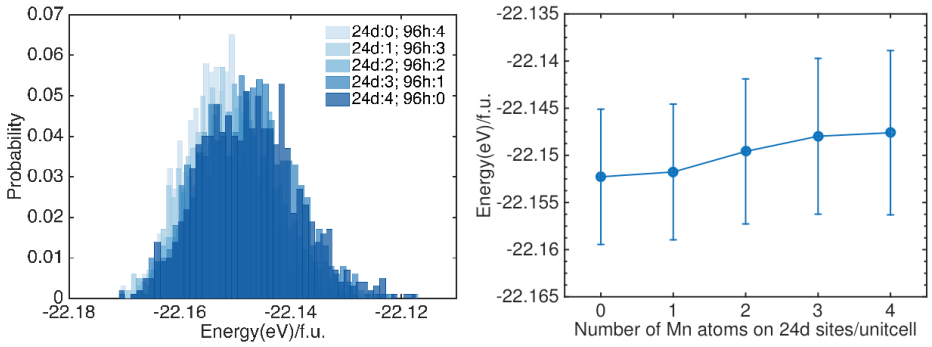

Figure 1.33 (a) Energy Distribution and (b) standard deviation of Mn doped LLAZO with four Mn atoms on all 24d sites; three on 24d, one on 96h; two on 24d, two on 96h sites; one on 24d, three on 96h sites; four on 96h sites, respectively.

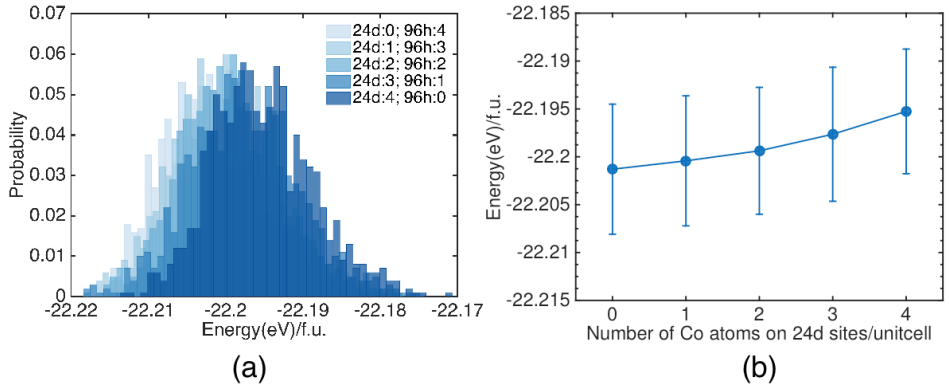

Figure 1.34 (a) Energy Distribution and (b) standard deviation of Mn doped LLAZO with four Mn atoms on all 24d sites; three on 24d, one on 96h; two on 24d, two on 96h sites; one on 24d, three on 96h sites; four on 96h sites, respectively.

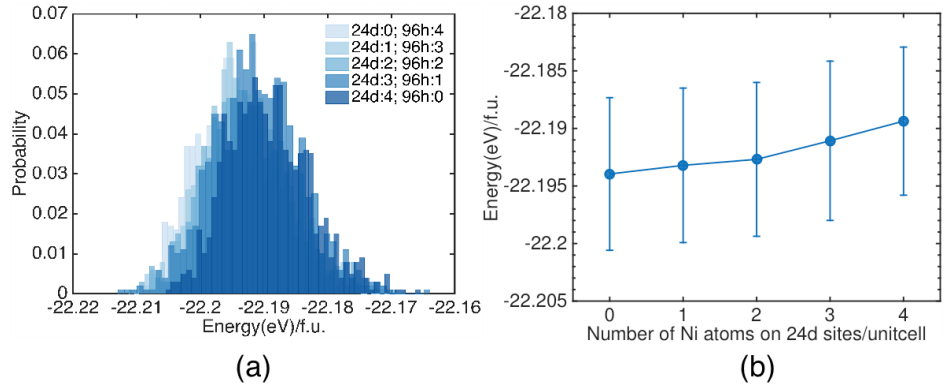

Figure 1.35 (a) Energy Distribution and (b) standard deviation of Ni doped LLAZO with four Ni atoms on all 24d sites; three on 24d, one on 96h; two on 24d, two on 96h sites; one on 24d, three on 96h sites; four on 96h sites, respectively.

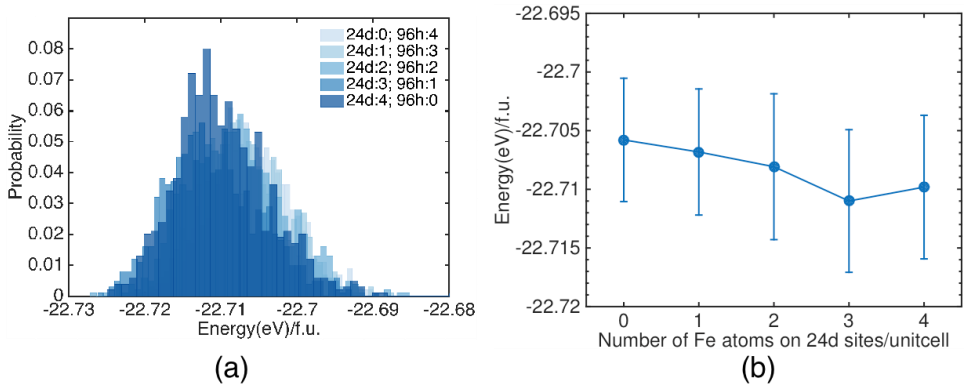

Figure 1.36 (a) Energy Distribution and (b) standard deviation of Fe doped LLAZO with four Fe atoms on all 24d sites; three on 24d, one on 96h; two on 24d, two on 96h sites; one on 24d, three on 96h sites; four on 96h sites, respectively.

5.3.3 Molecular Dynamics Simulations of Transition Metal and Li-Ion Transport.

The 3D network formed by mobile Li migrating along the Li sublattice in LLZO can be visualized by plotting probability density isosurfaces for Li ions over a MD time window. Figure 5.11 shows an example of these isosurfaces visualized along the <111> direction over a 1 ns time period. The magnified isosurface for pristine LLAZO (Figure 5.11a, left panel) is comprised of junctions between rings at 24d sites, and lobes formed by 96h sites. The isosurface forms a percolating network that spans the entire simulation cell, consistent with high Li-ion mobility.

In contrast to the highly connected isosurface for Li in pristine LLAZO, Figure 5.11b shows that the probability density for TM impurities in LLAZO is highly fragmented. This fragmentation implies that TMs are less mobile in LLAZO than is Li. The degree of fragmentation appears to be largest for Mn, roughly similar for Co and Ni, and smallest for Fe. Based on this qualitative analysis we expect Mn to be the slowest diffuser, Fe to be the fastest, and Co/Mn to fall in between. Figure 5.12 illustrates the temperature dependence of the probability density isosurfaces for Co and Fe at T = 800, 1000, and 1200 K.

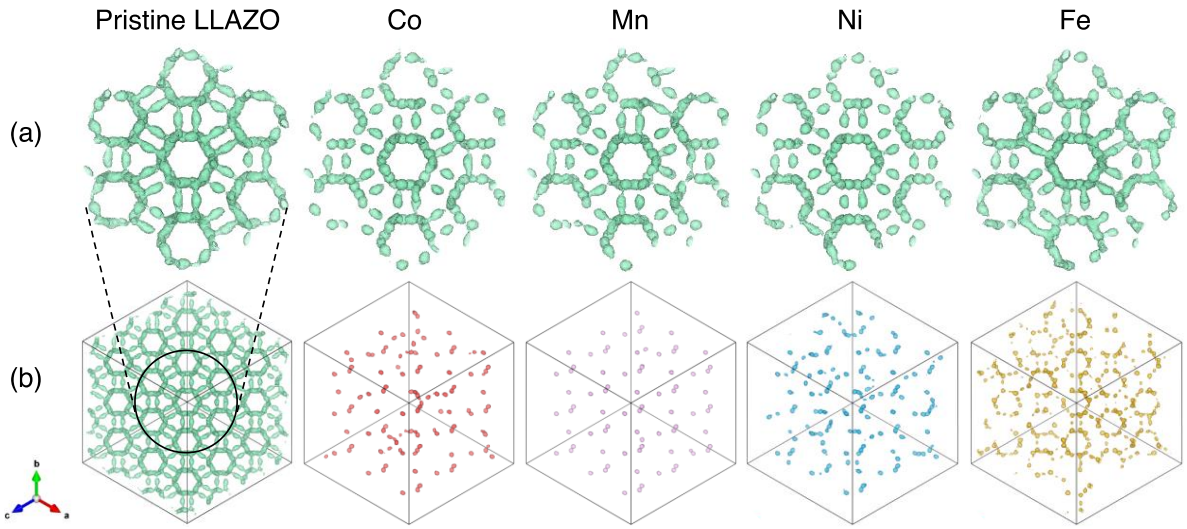

Figure 1.37 Probability density isosurfaces for Li and four transition metal impurities in LLAZO at T = 1000 K over a 1 ns MD simulation. (a) Magnified view of a portion of the Li isosurface from a pristine (i.e., impurity-free) LLAZO cell, and for LLAZO cells containing Co, Mn, Ni, or Fe TM impurities. (b). Isosurfaces from the entire simulation cell viewed along <111> depicting the mobility of Li-ions (far left), and for the various TM impurities (2nd through 5th panels). The isosurface level is equal to 10% of the maximum probability density.

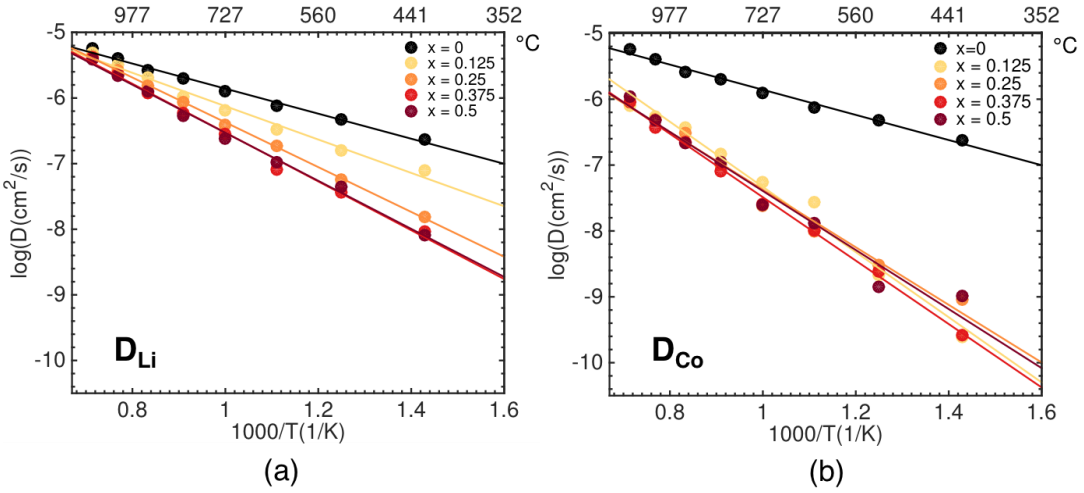

Figure 1.38 Diffusion coefficient of (a) Li (b) Co as a function of temperatures at different Co concentration (x = 0.125 to x = 0.5) in $Li_{6.25-2x}La_3Al_{0.25}Co_xZr_2O_{12}$.

Figure 5.11a shows the Li probability isosurfaces in the presence of TM impurities. These isosurfaces exhibit a larger degree of fragmentation relative to the pristine LLAZO case. Such an effect would occur if the TMs diffuse more slowly than Li, and thus act as an impediment to Li-ion motion along the Li-sublattice. Based on the isosurfaces in Figure 5.11a, it appears the slower motion of the TM is more harmful to Li migration than are the benefits conveyed by the additional Li vacancies these supervalent TMs generate (for charge balance). The TMs appear to have a similar effect to that of Al^{3+} dopants at high temperatures, which can also impede Li diffusion via their lower mobility and occupation of the Li sublattice.[173,181] Consequently, the cross-over of Co (or other TMs) from the cathode to LLZO could result in an impedance increase.

Figure 5.12 displays Arrhenius plots for diffusion coefficients derived from MD simulations on pristine LLAZO and TM doped LLAZO. The calculated activation energy, E_a, for Li-ions in pristine LLAZO is 0.38 eV, which is in good agreement with typical experimental values which range from 0.3 – 0.37 eV.[172,182,183] As expected, our activation energy is lower than that reported for undoped LLZO, 0.48 eV (at temperatures above the cubic-tetragonal phase transformation);[135] the lower value observed in the present study is consistent with the higher Li-

ion conductivity observed in Al-doped LLZO.

The diffusion behavior of the TMs is shown in Figure 5.13a. Consistent with the probability density isosurfaces of Figure 5.11b, the TMs exhibit lower diffusivity compared to Li^+. Moreover, the ordering of the relative diffusivities in Figure 5.13a are identical to those suggested in Figure 5.11b: Fe is the fastest diffuser, Co is the slowest, and Ni/Co fall between. The activation energies associated with diffusion of TMs are summarized in Table 5.1. As expected, Fe has the smallest activation energy overall, 0.49 eV, while Ni, Co, and Mn, and have values of 0.90, 0.98, and 1.09 eV.

Figure 5.13b shows the effect of TM impurities on the diffusion of Li in LLAZO. Overall, the presence of TMs impedes Li diffusion, as compared to pristine LLAZO. The relative impact of the different TM on Li-ion mobility follows a trend similar to that of the diffusivity of the TMs themselves: Fe, being the fastest TM diffuser, has the smallest impact on Li diffusion, with Ni, Co, and Mn having a similar, but more substantial impact. These trends are also reflected in the activation energy for Li diffusion, Table 5.1. We recall that in pristine LLAZO E_a = 0.38 eV. E_a increases in the presence of TM impurities, to 0.57 eV for Fe, and fall between 0.68 to 0.73 eV for Ni, Co, and Mn. Figure 5.12 shows that the negative impact of TMs impurities on Li diffusion depends on the impurity concentration. For example, as the concentration of Co increases from 0.5 to 2.2 at. %, the Li diffusion coefficient decreases by more than an order of magnitude at 1000 K. If bonding of LLZO with LCO is performed at high temperatures, then Co impurities will have a greater chance to diffuse into LLZO, thereby slowing Li diffusion (Figure 5.13b) and increasing interfacial resistance.

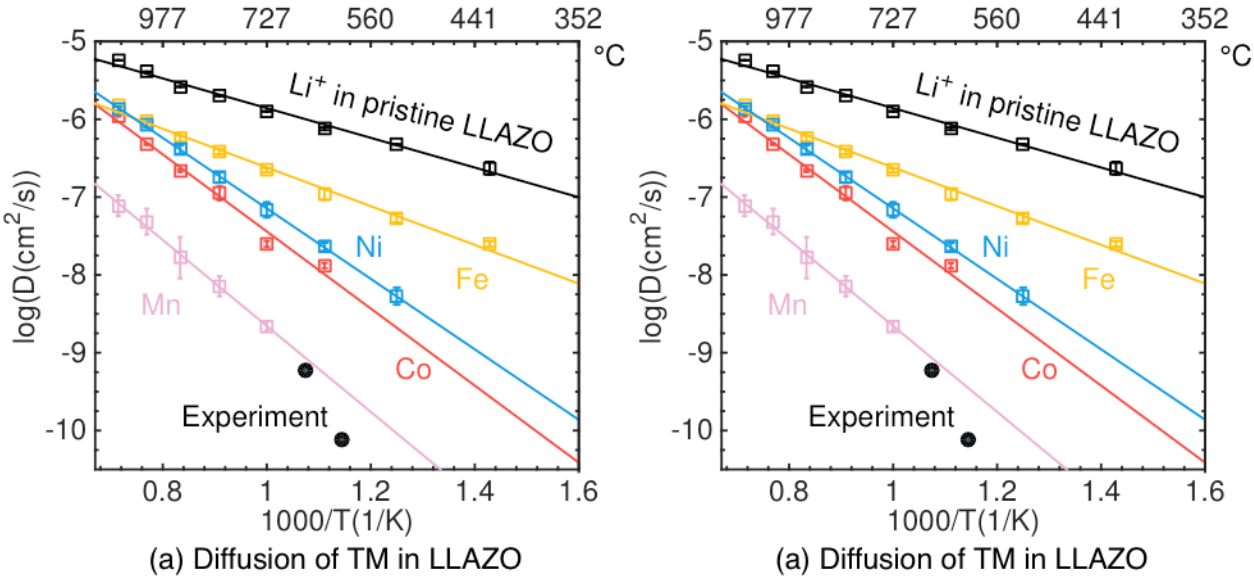

Figure 1.39 Arrhenius plots of (a) diffusivity of transition metals (Fe, Co, Mn, Ni) in LLAZO and Li in pristine LLAZO; (b) diffusivity of Li in LLAZO containing transition metal impurities. Black circles in panel (a) represent the Co diffusivity as estimated from EPMA measurements.

Why do TMs, and as a consequence, Li, move slower in TM-doped LLAZO? A potential explanation may be traced to the so-called bottleneck size for ion migration. We recall that the Li sublattice in LLZO is comprised of adjacent 24d (tetrahedral) and 96h (octahedral) sites. These polyhedral have oxygen at their vertices and share triangular faces at their junctions; a bottleneck occurs when an ion passes through these triangular faces. We observe that the size of this bottleneck is sensitive to the presence of TM impurities. The Zeo++ code was used to analyze the structure and topology of the Li sublattice within LLAZO. The bottleneck size was determined by calculating the largest pore diameter along the ion migration pathway.[184] Tabulated ionic radii were used for TMs and oxygen anions. We note that the TM ions considered here (Co^{2+}, Mn^{2+}, Ni^{2+}, Fe^{3+}) have smaller ionic radii (0.69Å~0.83Å) than does Li^{+}(0.90Å). Thus, we anticipate that TM occupation of Li sublattice sites will reduce the bottleneck radius, due to the smaller size of the TMs (relative to Li), and because supervalent TMs increase the Li vacancy concentration. Calculated bottleneck sizes are summarized in Table 1. The presence of TM impurities decreases the bottleneck radius from ~1.30 Å in pristine LLAZO, to 1.22 – 1.25 Å. This decrease potentially explains the reduced ionic mobility in TM-containing LLAZO. A similar observation of increased fragmentation of the Li probability

density was made for Ga-doped LLZO (Ga^{3+} ionic radius = 0.76Å).[180]

Table 1.8 Calculated activation energies (E_a) for transition metal (TM) diffusion in LLAZO (E_a (TM)) and for Li ion diffusion in pristine and TM-containing LLAZO (E_a (Li)). R_B refers to the bottleneck radius (R_B) for diffusion in pristine and TM-containing LLZO.

Impurity	E_a (TM) /eV	E_a (Li) /eV	R_B (Å)
Pristine/Li	-	0.38	1.299
Fe	0.49	0.57	1.245
Co	0.98	0.73	1.233
Mn	1.09	0.68	1.232
Ni	0.90	0.69	1.223

It is proposed that the Li^+ conductivity is determined by the active vacancy density at the octahedral sites.[185] Supervalent impurities such as Al and TM ions can increase Li vacancies, but the impurities themselves can also play a role by potentially jam the Li pathway. The octahedral (24d) site is thought to be critical for fast Li^+ transport. The doping may alter the vacancy distribution in the octahedral site to impact the conductivity. Chen et al. summarized experimental data and proposed a relationship between active octahedral vacancy density (ν) and the valence state, n, and doping level, x, of an impurity:[185] $\nu = 16 - (40 - 8n + 8f)x$, where f is the average number of vacancies that a dopant creates. The typical value of $f \sim 3.2$, which is estimated experimentally.[185] When $\nu > 0$, it was divided as high conductivity; when $\nu < 0$, it was divided as low conductivity. Therefore, for pristine LLAZO, Al^{3+} has $n = 3$ and $x = 0.25$, leading to $\nu = 5.6$, which falls into high conductivity region. In the case of LLAZO with TM impurities, namely $Li_{7-0.25*3-nx}La_3Al_{0.25}M_xZr_2O_{12}$, both Al^{3+} and TM ions exist. A derived formula for calculating active octahedral vacancy density is

$$\nu = 5.6 - (40 - 8n + 8f)x.$$

This results in a value of -15.2 for LLAZO with Fe^{3+} impurity and a value of -19.2 for LLAZO with Co^{2+}, Ni^{2+}, Mn^{2+} impurities. We noticed that LLAZO with TM impurities all falls into the low conductivity region. LLAZO with Co^{2+}, Ni^{2+}, Mn^{2+} impurities are estimated to have same value of ν, while Fe^{3+} has higher value of ν than them. This is qualitatively consistent with our diffusion coefficient calculation (Figure 5.13b), where we found LLAZO with Fe^{3+} impurities possess higher Li^{+} diffusion coefficient than LLAZO with other TM impurities (Co^{2+}, Ni^{2+}, Mn^{2+}), and LLAZO with Co^{2+}, Ni^{2+}, Mn^{2+} impurities show nearly identical Li^{+} diffusion coefficient.

5.4 Conclusion

In summary, we performed a combination of experimental and computational study to investigate the transition metal impurities in LLAZO. Experimentally, we found the Co will diffuse into LLAZO at high temperatures by substitute Li sites. A color change of LLZO was observed from white to blue in after hot-pressing of LLZO and LCO pallets. The concentration of Co impurities in LLAZO seems to increase as temperature increases. We estimated cobalt diffusion coefficient based on the concentration from EPMA measurements. The estimated diffusion coefficients are 6×10^{-10} cm^2 s^{-1} at 930K and 8×10^{-11} cm^2 s^{-1} at 873 K. Computationally, we examined transition metal impurities from common cathode materials. The effects of TM impurities on garnet-type LLAZO were investigated through classical molecular dynamics simulations using Morse potentials. The impurities were studied from probability density of ions, topological analysis and estimation of number of vacancies. We found diffusion of TMs is fast at very high temperatures, but also weaken quickly as temperature goes down. The diffusion of TM impurities is estimated in the order of D(Fe) > D(Ni) > D(Co) > D(Mn). TM impurities in LLAZO can impair Li diffusion in different level: Co, Mn and Ni have the similar level of damage while Fe has the smaller effect.

Chapter 6: Conclusions

Metal-oxygen batteries and solid electrolyte-based Li batteries are promising next generation batteries due to their potential for and high energy densities. However, there are several challenges that remain to be addressed before these batteries are practical. In metal-oxygen batteries, high overpotentials during charging result in low energy efficiencies of 60% and short cycle lifetimes. [1] In solid electrolyte-based batteries, cross-diffusion at the solid electrolyte/cathode interface may lead to high interfacial resistance, power density.[2,3] This thesis focused on understanding the charge transport properties in the discharge products of metal-oxygen batteries and in solid electrolytes containing transition metal impurities.

6.1 Transport in peroxides and superoxides

The high charging overpotentials in metal-oxygen batteries appear to correlate with the identity of the discharge products. Batteries that discharge to superoxide (LiO_2, NaO_2, KO_2) have low charging overpotentials, while batteries that discharge to peroxide (Na_2O_2, Li_2O_2) have high charging overpotentials. To understand the reason for the high overpotential, we performed density functional and quasi-particle GW calculations in peroxides and superoxides. Throughout, we used hybrid functionals to mitigate the delocalization errors typical of semi-local functionals.

As a first step we examined properties of the defect-free bulk materials. We found that both peroxides and superoxides are highly ionic crystals and that the electronic properties are mainly controlled by the oxygen p orbitals. For sodium peroxide (Na_2O_2), our calculations reveal that it is an electronic insulator, with a bandgap of nearly 7 eV. For the superoxides, in contrast to the half metallic behavior reported with semilocal functionals in the literature, the present hybrid functional calculations reveal bandgaps formed by splitting of oxygen π^* states. The GW

calculations predict that all the alkali metal superoxides are good insulators, with bandgaps in excess of 4 eV.

As a next step, the electronic and ionic conductivity arising from the migration of intrinsic defects was explored by calculating the equilibrium concentrations and mobilities of several carrier types. We found that the electronic transport in alkali peroxides and superoxides is governed by the unusual ability of oxygen dimers to adopt three charge states: O_2^{2-}, O_2^{1-}, and O_2^{0}. In both peroxides and superoxides, self-trapped holes and electrons localize on the oxygen dimers, forming small polarons.

In Na_2O_2, peroxide dimers O_2^{2-} tend to shed electrons to form superoxide dimers, O_2^{-} (i.e. a hole polaron). The electronic transport properties are remarkably similar to those reported previously for lithium peroxide, suggesting a low electronic conductivity on the order of 10^{-20} S/cm.

Compared to the peroxides; transport in superoxides has not been widely explored. The present study reveals that transport in superoxides has some features in common with the peroxide; nevertheless several important distinctions exist.

NaO_2, similar to Na_2O_2, is predicted to be a poor electrical conductor. Different from Na_2O_2, electronic transport in NaO_2 is mediated by a *combination* of electron and hole polarons. More specifically, conductivity arising from electron polarons is predicted to be 8.2×10^{-20} S/cm, while for holes the conductivity is about 5.5 times smaller, 1.5×10^{-20} S/cm. The mixed contribution to electrical conductivity is due to counterbalancing trends in the concentrations and mobilities of these carriers.

KO_2 is also predicted to be a poor electrical conductor. In KO_2, hole polarons also dominate electronic transport, and superoxide dimers O_2^{-} can shed electrons to form neutral oxygen dimers, O_2^{0}. This mechanism results in a conductivity of 1×10^{-20} S/cm.

LiO_2 is predicted to have the highest electronic conductivity amongst the superoxides. Here, electron polarons, which are formed by the addition of an electron to a superoxide dimer, dominate the electronic conductivity due to their relatively high concentrations and mobility. The conductivity (9×10^{-12} S/cm) originating from electron polarons is 8 times higher than in NaO_2 or KO_2.

Additionally, the ionic transport properties of superoxides and peroxides were found to differ significantly. In Na_2O_2, the ionic conductivity is low, and comparable to the electronic conductivity; it is comprised primarily of n-type contributions from negative vacancies. In superoxides, in addition to n-type contributions from negative metal vacancies, *p*-type contributions to conductivity from mobile oxygen dimer vacancies can be much larger. These dimer vacancies have the highest concentrations amongst the defects considered, and migrate relatively quickly (without O-O bond dissociation). This leads to higher ionic conductivity in superoxides compared to the peroxides. The high mobility of oxygen dimers in the superoxides is consistent with a recent experimental study by Gerbig *et al*.[4] on potassium superoxide and other heavier superoxides.

The limited electronic conductivity predicted for NaO_2 and KO_2 suggests that bulk transport within them is unlikely to account for the low overpotentials associated with their decomposition during charging. We therefore conclude that the enhanced efficiency observed in cells that discharge to NaO_2 and KO_2 must arise from other phenomena.

6.2 Solid electrolyte with transition metal impurities

The garnet with composition $Li_7La_3Zr_2O_{12}$ (LLZO) is regarded as a highly promising solid electrolyte. Al is usually doped into LLZO to stabilize the cubic phase and to enhance the room temperature Li^+ conductivity, forming $Li_{6.25}Al_{0.25}La_3Zr_2O_{12}$ (LLAZO). Computation, in combination with experimental measurements by collaborators, was used to investigate the impact of transition metal impurities on diffusion in LLAZO. We constructed a cobalt diffusion model to calculate cobalt diffusion coefficient based on the experimental measurement of cobalt concentration in LLAZO. A computational model of the transition metal doped LLAZO structure was created using a random sampling approach. We performed classical molecular dynamics simulations to investigate the transport rates of transition metals (Co, Mn, Ni and Fe) in LLAZO, and to predict how transition metal impurities impact Li ion migration. Transition metals are found to diffuse slower than Li, with the diffusivity magnitudes given in the order of D(Fe) > D(Ni) > D(Co) > D(Mn). Based on probability density analysis and mean squared displacements, we found that slower motion of the transition metals is more harmful to Li migration than are the benefits conveyed by the Li vacancies the transition metal generates. Transition metal impurities

in LLAZO slow Li diffusion via a traffic-jam mechanism: Co, Mn and Ni have a similar effect on Li diffusion, while Fe has the smallest (i.e., least harmful) effect. Our calculations provide a possible explanation for the mechanisms underlying resistance at LLZO/cathode interfaces.

6.3 Outlook and Future work

To our knowledge, the present study is the first to perform a comprehensive theoretical analysis of transport mechanisms across the alkali superoxides. We note that in this thesis the conductivity is calculated under equilibrium conditions, whereas in real batteries, the actual conductivity may be much higher due to non-equilibrium effects, or do to contributions from microstructural features such as surfaces and grain boundaries. Additional research needs to be undertaken to understand the charge transport mechanisms under non-equilibrium conditions and in the presence of these features. Moreover, other factors could substantially contribute to the charging overpotential, such as electrolyte degradation and contributions from soluble charge carriers (i.e., redox mediators) that could bypass solid-state transport. Future studies of the overpotential mechanism should also consider these mechanisms.

As for ion cross diffusion in solid electrolytes, future studies could explore transition metal cross over in other solid electrolyte materials such as $Li_{10}GeP_2S_{12}$ and $Li_5La_3Ta_2O_{12}$. Additionally, more research is needed to explore the effects on stability due to oxygen or lithium loss from the garnet during high-temperature sintering.

Bibliography

(1) Chu, S.; Majumdar, A. Opportunities and Challenges for a Sustainable Energy Future. *Nature* **2012**, *488* (7411), 294–303.

(2) Tarascon, J. M.; Armand, M. Issues and Challenges Facing Rechargeable Lithium Batteries. *Nature* **2001**, *414* (6861), 359–367.

(3) Luntz, A. C.; Voss, J.; Reuter, K. Interfacial Challenges in Solid-State Li Ion Batteries. *J. Phys. Chem. Lett.* **2015**, *6* (22), 4599–4604.

(4) Li, N. W.; Yin, Y. X.; Yang, C. P.; Guo, Y. G. An Artificial Solid Electrolyte Interphase Layer for Stable Lithium Metal Anodes. *Adv. Mater.* **2016**, *28* (9), 1853–1858.

(5) Li, N. W.; Yin, Y. X.; Li, J. Y.; Zhang, C. H.; Guo, Y. G. Passivation of Lithium Metal Anode via Hybrid Ionic Liquid Electrolyte toward Stable Li Plating/Stripping. *Adv. Sci.* **2017**, *4* (2), 2–7.

(6) Yang, C.-P.; Yin, Y.-X.; Zhang, S.-F.; Li, N.-W.; Guo, Y.-G. Accommodating Lithium into 3D Current Collectors with a Submicron Skeleton towards Long-Life Lithium Metal Anodes. *Nat. Commun.* **2015**, *6* (May), 8058.

(7) Janek, J.; Zeier, W. G. A Solid Future for Battery Development. *Nat. Energy* **2016**, *1* (9), 16141.

(8) Xu, W.; Wang, J.; Ding, F.; Chen, X.; Nasybulin, E.; Zhang, Y.; Zhang, J.-G. Lithium Metal Anodes for Rechargeable Batteries. *Energy Environ. Sci.* **2014**, *7* (2), 513–537.

(9) Xin, S.; Chang, Z.; Zhang, X.; Guo, Y. G. Progress of Rechargeable Lithium Metal Batteries Based on Conversion Reactions. *Natl. Sci. Rev.* **2017**, *4* (1), 54–70.

(10) Sun, Y.; Liu, N.; Cui, Y. Promises and Challenges of Nanomaterials for Lithium-Based Rechargeable Batteries. *Nat. Energy* **2016**, *1* (7), 16071.

(11) Zheng, G.; Wang, C.; Pei, A.; Lopez, J.; Shi, F.; Chen, Z.; Sendek, A. D.; Lee, H.-W.; Lu, Z.; Schneider, H.; Safont-Sempere, M. M.; Chu, S.; Bao, Z.; Cui, Y. High-Performance Lithium Metal Negative Electrode with a Soft and Flowable Polymer Coating. *ACS Energy Lett.* **2016**, *1* (6), 1247–1255.

(12) Sacci, R. L.; Black, J. M.; Balke, N.; Dudney, N. J.; More, K. L.; Unocic, R. R. Nanoscale Imaging of Fundamental Li Battery Chemistry: Solid-Electrolyte Interphase Formation and Preferential Growth of Lithium Metal Nanoclusters. *Nano Lett.* **2015**, *15* (3), 2011–

2018.

(13) Chang, H. J.; Ilott, A. J.; Trease, N. M.; Mohammadi, M.; Jerschow, A.; Grey, C. P. Correlating Microstructural Lithium Metal Growth with Electrolyte Salt Depletion in Lithium Batteries Using Li MRI. *J. Am. Chem. Soc.* **2015**, *137* (48), 15209–15216.

(14) Lv, D.; Shao, Y.; Lozano, T.; Bennett, W. D.; Graff, G. L.; Polzin, B.; Zhang, J.; Engelhard, M. H.; Saenz, N. T.; Henderson, W. A.; Bhattacharya, P.; Liu, J.; Xiao, J. Failure Mechanism for Fast-Charged Lithium Metal Batteries with Liquid Electrolytes. *Adv. Energy Mater.* **2015**, *5* (3), 1–7.

(15) Luntz, A. C.; Voss, J.; Reuter, K. Interfacial Challenges in Solid-State Li Ion Batteries. *J. Phys. Chem. Lett.* **2015**, *6* (22), 4599–4604.

(16) Xin, S.; You, Y.; Wang, S.; Gao, H.-C.; Yin, Y.-X.; Guo, Y.-G. Solid-State Lithium Metal Batteries Promoted by Nanotechnology: Progress and Prospects. *ACS Energy Lett.* **2017**, *2* (6), 1385–1394.

(17) Ohzuku, T.; Ueda, A.; Nagayama, M. Electrochemistry and Structural Chemistry of $LiNiO_2$ (R3m) for 4 Volt Secondary Lithium Cells. *J. Electrochem. Soc.* **1993**, *140* (7), 1862.

(18) Yang, X. Q.; McBreen, J.; Yoon, W. S.; Grey, C. P. Crystal Structure Changes of $LiMn_{0.5}Ni_{0.5}O_2$ Cathode Materials during Charge and Discharge Studied by Synchrotron Based in Situ XRD. *Electrochem. commun.* **2002**, *4* (8), 649–654.

(19) Yoon, W. S.; Chung, K. Y.; McBreen, J.; Yang, X. Q. A Comparative Study on Structural Changes of $LiCo_{1/3}Ni_{1/3}Mn_{1/3}O_2$ and $LiNi_{0.8}Co_{0.15}Al_{0.05}O_2$ during First Charge Using in Situ XRD. *Electrochem. commun.* **2006**, *8* (8), 1257–1262.

(20) Yang, X. Q.; Sun, X.; McBreen, J. New Phases and Phase Transitions Observed in $Li_{(1-x)}CoO_2$ during Charge: In Situ Synchrotron X-Ray Diffraction Studies. *Electrochem. commun.* **2000**, *2* (2), 100–103.

(21) Yue, L.; Ma, J.; Zhang, J.; Zhao, J.; Dong, S.; Liu, Z.; Cui, G.; Chen, L. All Solid-State Polymer Electrolytes for High-Performance Lithium Ion Batteries. *Energy Storage Mater.* **2016**, *5*, 139–164.

(22) Manuel Stephan, A.; Nahm, K. S. Review on Composite Polymer Electrolytes for Lithium Batteries. *Polymer (Guildf).* **2006**, *47* (16), 5952–5964.

(23) Xie, H.; Alonso, J. a.; Li, Y.; Fernández-Díaz, M. T.; Goodenough, J. B. Lithium Distribution in Aluminum-Free Cubic $Li_7La_3Zr_2O_{12}$. *Chem. Mater.* **2011**, *23* (16), 3587–3589.

(24) Bernstein, N.; Johannes, M. D.; Hoang, K. Origin of the Structural Phase Transition in $Li_7La_3Zr_2O_{12}$. *Phys. Rev. Lett.* **2012**, *109* (20), 1–5.

(25) Rangasamy, E.; Wolfenstine, J.; Allen, J.; Sakamoto, J. The Effect of 24c-Site (A) Cation Substitution on the Tetragonal-Cubic Phase Transition in $Li_{7-x}La_{3-x}A_xZr_2O_{12}$ Garnet-Based Ceramic Electrolyte. *J. Power Sources* **2013**, *230*, 261–266.

(26) Wu, J.-F.; Chen, E.-Y.; Yu, Y.; Liu, L.; Wu, Y.; Pang, W. K.; Peterson, V. K.; Guo, X. Gallium-Doped $Li_7La_3Zr_2O_{12}$ Garnet-Type Electrolytes with High Lithium-Ion Conductivity. *ACS Appl. Mater. Interfaces* **2017**, *9* (2), 1542–1552.

(27) Huang, M.; Shoji, M.; Shen, Y.; Nan, C.-W.; Munakata, H.; Kanamura, K. Preparation and Electrochemical Properties of Zr-Site Substituted $Li_7La_3(Zr_{2-x}M_x)O_{12}$ (M = Ta, Nb) Solid Electrolytes. *J. Power Sources* **2014**, *261*, 206–211.

(28) Wang, D.; Zhong, G.; Dolotko, O.; Li, Y.; McDonald, M. J.; Mi, J.; Fu, R.; Yang, Y. The Synergistic Effects of Al and Te on the Structure and Li^+ -Mobility of Garnet-Type Solid Electrolytes. *J. Mater. Chem. A* **2014**, *2* (47), 20271–20279.

(29) Thompson, T.; Wolfenstine, J.; Allen, J. L.; Johannes, M.; Huq, A.; David, I. N.; Sakamoto, J. Tetragonal vs. Cubic Phase Stability in Al - Free Ta Doped $Li_7La_3Zr_2O_{12}$ (LLZO). *J. Mater. Chem. A* **2014**, *2* (33), 13431–13436.

(30) Kotobuki, M.; Munakata, H.; Kanamura, K.; Sato, Y.; Yoshida, T. Compatibility of $Li_7La_3Zr_2O_{12}$ Solid Electrolyte to All-Solid-State Battery Using Li Metal Anode. *J. Electrochem. Soc.* **2010**, *157* (10), A1076–A1079.

(31) Kim, K. H.; Iriyama, Y.; Yamamoto, K.; Kumazaki, S.; Asaka, T.; Tanabe, K.; Fisher, C. a. J.; Hirayama, T.; Murugan, R.; Ogumi, Z. Characterization of the Interface between $LiCoO_2$ and $Li_7La_3Zr_2O_{12}$ in an All-Solid-State Rechargeable Lithium Battery. *J. Power Sources* **2011**, *196* (2), 764–767.

(32) Ni, J. E.; Case, E. D.; Sakamoto, J. S.; Rangasamy, E.; Wolfenstine, J. B. Room Temperature Elastic Moduli and Vickers Hardness of Hot-Pressed LLZO Cubic Garnet. *J. Mater. Sci.* **2012**, *47* (23), 7978–7985.

(33) Kotobuki, M.; Kanamura, K. Fabrication of All-Solid-State Battery Using Li5La 3Ta2O12 Ceramic Electrolyte. *Ceram. Int.* **2013**, *39* (6), 6481–6487.

(34) Ohta, S.; Kobayashi, T.; Seki, J.; Asaoka, T. Electrochemical Performance of an All-Solid-State Lithium Ion Battery with Garnet-Type Oxide Electrolyte. *J. Power Sources* **2012**, *202*, 332–335.

(35) Park, K.; Yu, B. C.; Jung, J. W.; Li, Y.; Zhou, W.; Gao, H.; Son, S.; Goodenough, J. B. Electrochemical Nature of the Cathode Interface for a Solid-State Lithium-Ion Battery: Interface between $LiCoO_2$ and Garnet-$Li_7La_3Zr_2O_{12}$. *Chem. Mater.* **2016**, *28* (21), 8051–8059.

(36) Miara, L. J.; Richards, W. D.; Wang, Y. E.; Ceder, G. First-Principles Studies on Cation Dopants and Electrolyte|Cathode Interphases for Lithium Garnets. *Chem. Mater.* **2015**, *27* (11), 4040–4047.

(37) Ller, È.; Holzer, F.; Haas, O.; Mu, S. Optimized Zinc Electrode for the Rechargeable Zinc ± Air Battery. *J. Appl. Electrochem.* **1998**, *28*, 895–898.

(38) Mori, R. A Novel Aluminium-Air Secondary Battery with Long-Term Stability. *Rsc Adv.* **2014**, *4* (4), 1982–1987.

(39) Reddy, T. *Linden's Handbook of Batteries*; McGraw-Hill Education, 2010.

(40) Abraham, K. M.; Jiang, Z. A Polymer Electrolyte − Based Rechargeable Lithium / Oxygen Battery TECHNICAL PAPERS ELECTROCHEMICAL SCIENCE AND TECHNOLOGY A Polymer Electrolyte-Based Rechargeable Lithium / Oxygen Battery. *J. Electrochem. Soc.* **1996**, *143* (1), 1–5.

(41) Das, S. K.; Lau, S.; Archer, L. a. Sodium–oxygen Batteries: A New Class of Metal–air Batteries. *J. Mater. Chem. A* **2014**, *2* (32), 12623.

(42) Ren, X.; Wu, Y. A Low-Overpotential Potassium-Oxygen Battery Based on Potassium Superoxide. *J. Am. Chem. Soc.* **2013**, *135* (8), 2923–2926.

(43) Shiga, T.; Hase, Y.; Yagi, Y.; Takahashi, N.; Takechi, K. Catalytic Cycle Employing a TEMPO–Anion Complex to Obtain a Secondary Mg–O_2 Battery. *J. Phys. Chem. Lett.* **2014**, *5* (10), 1648–1652.

(44) Adams, B. D.; Radtke, C.; Black, R.; Trudeau, M. L.; Zaghib, K.; Nazar, L. F. Current Density Dependence of Peroxide Formation in the Li–O_2 Battery and Its Effect on Charge. *Energy Environ. Sci.* **2013**, *6*, 1772.

(45) Mitchell, R.; Gallant, B. Mechanisms of Morphological Evolution of Li_2O_2 Particles during Electrochemical Growth. *J. Phys. Chem. Lett.* **2013**, *4* (7), 1060–1064.

(46) Viswanathan, V.; Thygesen, K. S.; Hummelshj, J. S.; Nrskov, J. K.; Girishkumar, G.; McCloskey, B. D.; Luntz, A. C. Electrical Conductivity in Li_2O_2 and Its Role in Determining Capacity Limitations in Non-Aqueous Li-O_2 Batteries. *J. Chem. Phys.* **2011**, *135* (21).

(47) Griffith, L. D.; Sleightholme, A. E. S.; Mansfield, J. F.; Siegel, D. J.; Monroe, C. W. Correlating Li/O_2 Cell Capacity and Product Morphology with Discharge Current. *ACS Appl. Mater. Interfaces* **2015**, *7* (14), 7670–7678.

(48) Jung, H.-G.; Kim, H.-S.; Park, J.-B.; Oh, I.-H.; Hassoun, J.; Yoon, C. S.; Scrosati, B.; Sun, Y.-K. A Transmission Electron Microscopy Study of the Electrochemical Process of Lithium–Oxygen Cells. *Nano Lett.* **2012**, *12* (8), 4333–4335.

(49) Lau, K. C.; Lu, J.; Luo, X.; Curtiss, L. A.; Amine, K. Implications of the Unpaired Spins in Li-O_2 Battery Chemistry and Electrochemistry: A Minireview. *Chempluschem* **2015**, *80* (2), 336–343.

(50) Sangster, J.; Pelton, A. D. The Li-O (Lithium-Oxygen) System. *J. Phase Equilibria* **1992**, *13* (3), 296–299.

(51) Lu, J.; Jung, H.-J.; Lau, K. C.; Zhang, Z.; Schlueter, J. a; Du, P.; Assary, R. S.; Greeley, J.; Ferguson, G. a; Wang, H.-H.; Hassoun, J.; Iddir, H.; Zhou, J.; Zuin, L.; Hu, Y.; Sun, Y.-K.; Scrosati, B.; Curtiss, L. a; Amine, K. Magnetism in Lithium-Oxygen Discharge Product. *ChemSusChem* **2013**, 1–8.

(52) Radin, M. D.; Rodriguez, J. F.; Tian, F.; Siegel, D. J. Lithium Peroxide Surfaces Are Metallic, While Lithium Oxide Surfaces Are Not. *J. Am. Chem. Soc.* **2012**, *134* (2), 1093–1103.

(53) Zhai, D.; Wang, H. H.; Yang, J.; Lau, K. C.; Li, K.; Amine, K.; Curtiss, L. A.

Disproportionation in Li-O_2 Batteries Based on a Large Surface Area Carbon Cathode. *J. Am. Chem. Soc.* **2013**, *135* (41), 15364–15372.

(54) Ong, S. P.; Mo, Y.; Ceder, G. Low Hole Polaron Migration Barrier in Lithium Peroxide. *Phys. Rev. B* **2012**, *85* (8), 81105.

(55) Radin, M. D.; Siegel, D. J. Charge Transport in Lithium Peroxide: Relevance for Rechargeable Metal–air Batteries. *Energy Environ. Sci.* **2013**, *6* (8), 2370–2379.

(56) Lu, J.; Jung Lee, Y.; Luo, X.; Chun Lau, K.; Asadi, M.; Wang, H.-H.; Brombosz, S.; Wen, J.; Zhai, D.; Chen, Z.; Miller, D. J.; Sub Jeong, Y.; Park, J.-B.; Zak Fang, Z.; Kumar, B.; Salehi-Khojin, A.; Sun, Y.-K.; Curtiss, L. A.; Amine, K. A Lithium–oxygen Battery Based on Lithium Superoxide. *Nature* **2016**, *529* (7586), 377–382.

(57) Nandy, A. K.; Mahadevan, P.; Sen, P.; Sarma, D. D. KO_2: Realization of Orbital Ordering in a p-Orbital System. *Phys. Rev. Lett.* **2010**, *105* (5), 56403.

(58) Johnson, L.; Li, C.; Liu, Z.; Chen, Y.; Freunberger, S. a.; Tarascon, J.-M.; Ashok, P. C.; Praveen, B. B.; Dholakia, K.; Bruce, P. G. The Role of LiO_2 Solubility in O_2 Reduction in Aprotic Solvents and Its Consequences for Li–O_2 Batteries. *Nat. Chem.* **2014**, *6* (12), 1091–1099.

(59) Aetukuri, N. B.; McCloskey, B. D.; García, J. M.; Krupp, L. E.; Viswanathan, V.; Luntz, A. C. Solvating Additives Drive Solution-Mediated Electrochemistry and Enhance Toroid Growth in Non-Aqueous Li–O_2 Batteries. *Nat. Chem.* **2014**, 1–41.

(60) Kwabi, D. G.; Bryantsev, V. S.; Batcho, T. P.; Itkis, D. M.; Thompson, C. V.; Shao-Horn, Y. Experimental and Computational Analysis of the Solvent-Dependent O_2/Li^+-O_2- Redox Couple: Standard Potentials, Coupling Strength, and Implications for Lithium-Oxygen Batteries. *Angew. Chemie - Int. Ed.* **2016**, *55* (9), 3129–3134.

(61) Gutmann, V. Solvent Effects on the Reactivities of Organometallic Compounds. *Coord. Chem. Rev.* **1976**, *18* (2), 225–255.

(62) Henderson, W. A. Glyme-Lithium Salt Phase Behavior. *J. Phys. Chem. B* **2006**, *110* (26), 13177–13183.

(63) Aurbach, D.; McCloskey, B. D.; Nazar, L. F.; Bruce, P. G. Advances in Understanding Mechanisms Underpinning Lithium–air Batteries. *Nat. Energy* **2016**, *1* (9), 16128.

(64) Ganapathy, S.; Adams, B. D.; Stenou, G.; Anastasaki, M. S.; Goubitz, K.; Miao, X. F.; Nazar, L. F.; Wagemaker, M. Nature of Li_2O_2 Oxidation in a Li-O_2 Battery Revealed by Operando X-Ray Diffraction. *J. Am. Chem. Soc.* **2014**, *136* (46), 16335–16344.

(65) Meini, S.; Solchenbach, S.; Piana, M.; Gasteiger, H. A. The Role of Electrolyte Solvent Stability and Electrolyte Impurities in the Electrooxidation of Li_2O_2 in Li-O_2 Batteries. *J. Electrochem. Soc.* **2014**, *161* (9), A1306–A1314.

(66) Gao, X.; Chen, Y.; Johnson, L.; Bruce, P. G. Promoting Solution Phase Discharge in Li–O_2 Batteries Containing Weakly Solvating Electrolyte Solutions. *Nat. Mater.* **2016**, *15* (8), 882–888.

(67) Freunberger, S. a; Chen, Y.; Peng, Z.; Griffin, J. M.; Hardwick, L. J.; Bardé, F.; Novák, P.; Bruce, P. G. Reactions in the Rechargeable Lithium-O2 Battery with Alkyl Carbonate Electrolytes. *J. Am. Chem. Soc.* **2011**, *133* (20), 8040–8047.

(68) McCloskey, B. D.; Garcia, J. M.; Luntz, A. C. Chemical and Electrochemical Differences in Nonaqueous Li–O_2 and Na–O_2 Batteries. *J. Phys. Chem. Lett.* **2014**, *5* (7), 1230–1235.

(69) Chen, Y.; Freunberger, S. A.; Peng, Z.; Fontaine, O.; Bruce, P. G. Charging a Li–O_2 Battery Using a Redox Mediator. *Nat. Chem.* **2013**, *5* (6), 489–494.

(70) Bergner, B. J.; Schurmann, A.; Peppler, K.; Garsuch, A.; Janek, J. TEMPO: A Mobile Catalyst for Rechargeable Li-O_2 Batteries. *J. Am. Chem. Soc.* **2014**, *136* (42), 15054–15064.

(71) Bergner, B. J.; Hofmann, C.; Schürmann, A.; Schröder, D.; Peppler, K.; Schreiner, P. R.; Janek, J. Understanding the Fundamentals of Redox Mediators in Li–O_2 Batteries: A Case Study on Nitroxides. *Phys. Chem. Chem. Phys.* **2015**, *17* (47), 31769–31779.

(72) Kwak, W.-J.; Hirshberg, D.; Sharon, D.; Shin, H.-J.; Afri, M.; Park, J.-B.; Garsuch, A.; Chesneau, F. F.; Frimer, A. A.; Aurbach, D.; Sun, Y.-K. Understanding the Behavior of Li–oxygen Cells Containing LiI. *J. Mater. Chem. A* **2015**, *3* (16), 8855–8864.

(73) Zhang, T.; Liao, K.; He, P.; Zhou, H. A Self-Defense Redox Mediator for Efficient lithium–O_2 Batteries. *Energy Environ. Sci.* **2016**, *9* (3), 1024–1030.

(74) Lim, H. D.; Song, H.; Kim, J.; Gwon, H.; Bae, Y.; Park, K. Y.; Hong, J.; Kim, H.; Kim, T.; Kim, Y. H.; Leprõ, X.; Ovalle-Robles, R.; Baughman, R. H.; Kang, K. Superior Rechargeability and Efficiency of Lithium-Oxygen Batteries: Hierarchical Air Electrode Architecture Combined with a Soluble Catalyst. *Angew. Chemie - Int. Ed.* **2014**, *53* (15), 3926–3931.

(75) Hartmann, P.; Bender, C. L.; Vračar, M.; Dürr, A. K.; Garsuch, A.; Janek, J.; Adelhelm, P. A Rechargeable Room-Temperature Sodium Superoxide (NaO_2) Battery. *Nat. Mater.* **2013**, *12* (3), 228–232.

(76) Sun, Q.; Yang, Y.; Fu, Z.-W. Electrochemical Properties of Room Temperature Sodium–air Batteries with Non-Aqueous Electrolyte. *Electrochem. commun.* **2012**, *16* (1), 22–25.

(77) Yadegari, H.; Li, Y.; Banis, M. N.; Li, X.; Wang, B.; Sun, Q.; Li, R.; Sham, T.-K.; Cui, X.; Sun, X. On Rechargeability and Reaction Kinetics of Sodium–air Batteries. *Energy Environ. Sci.* **2014**, *7* (11), 3747–3757.

(78) Zhao, N.; Li, C.; Guo, X. Long-Life Na–O_2 Batteries with High Energy Efficiency Enabled by Electrochemically Splitting NaO_2 at a Low Overpotential. *Phys. Chem. Chem. Phys.* **2014**, *16* (29), 15646.

(79) Hueso, K. B.; Armand, M.; Rojo, T. High Temperature Sodium Batteries: Status, Challenges and Future Trends. *Energy Environ. Sci.* **2013**, *6* (3), 734.

(80) Hartmann, P.; Bender, C. L.; Sann, J.; Dürr, A. K.; Jansen, M.; Janek, J.; Adelhelm, P. A Comprehensive Study on the Cell Chemistry of the Sodium Superoxide (NaO_2) Battery. *Phys. Chem. Chem. Phys.* **2013**, *15* (28), 11661–11672.

(81) Bender, C. L.; Hartmann, P.; Vračar, M.; Adelhelm, P.; Janek, J. On the Thermodynamics, the Role of the Carbon Cathode, and the Cycle Life of the Sodium Superoxide (NaO_2) Battery. *Adv. Energy Mater.* **2014**, *4* (12), 1301863.

(82) Lee, B.; Seo, D.-H.; Lim, H.-D.; Park, I.; Park, K.-Y.; Kim, J.; Kang, K. First-Principles Study of the Reaction Mechanism in Sodium–Oxygen Batteries. *Chem. Mater.* **2014**, *26* (2), 1048–1055.

(83) Bender, C. L.; Schröder, D.; Pinedo, R.; Adelhelm, P.; Janek, J. One- or Two-Electron Transfer? The Ambiguous Nature of the Discharge Products in Sodium-Oxygen Batteries. *Angew. Chemie - Int. Ed.* **2016**, *55* (15), 4640–4649.

(84) Kang, S.; Mo, Y.; Ong, S. P.; Ceder, G. Nanoscale Stabilization of Sodium Oxides: Implications for Na-O_2 Batteries. *Nano Lett.* **2014**, *14* (2), 1016–1020.

(85) Khan, A. U.; Mahanti, S. D. Collective Electron Effects of O_2^- in Potassium Superoxide. *J. Chem. Phys.* **1975**, *63* (6), 2271.

(86) Gerbig, O. Defect Chemistry in Alkali Peroxides and Superoxides. **2014**.

(87) Gerbig, O.; Merkle, R.; Maier, J. Electrical Transport and Oxygen Exchange in the Superoxides of Potassium, Rubidium, and Cesium. *Adv. Funct. Mater.* **2015**, *25* (17), 2552–2563.

(88) Hohenberg, P.; Kohn, W. Inhomogeneous Electron Gas. *Phys. Rev.* **1964**, *136* (3B), B864.

(89) Rajagopal, A. K.; Callaway, J. Inhomogeneous Electron Gas. *Phys. Rev. B* **1973**, *7* (5), 1912–1919.

(90) Kohn, W.; Sham, L. J. Self-Consistent Equations Including Exchange and Correlation Effects. *Phys. Rev.* **1965**, *140* (4A).

(91) CEPERLEY, D.; ALDER, B. Quantum Monte Carlo. *Science (80-.).* **1986**, *231* (4738), 555–560.

(92) Klimeš, J.; Michaelides, A. Perspective: Advances and Challenges in Treating van Der Waals Dispersion Forces in Density Functional Theory. *J. Chem. Phys.* **2012**, *137* (12), 120901.

(93) Martin, R. M. *Electronic Structure: Basic Theory and Practical Methods*; Cambridge University Press: Cambridge, UK, 2004.

(94) Mori-Sánchez, P.; Cohen, A.; Yang, W. Localization and Delocalization Errors in Density Functional Theory and Implications for Band-Gap Prediction. *Phys. Rev. Lett.* **2008**, *100* (14), 146401.

(95) Cohen, A. J.; Mori-Sánchez, P.; Yang, W. Insights into Current Limitations of Density Functional Theory. *Science* **2008**, *321* (5890), 792–794.

(96) Dion, M.; Rydberg, H.; Schröder, E.; Langreth, D. C.; Lundqvist, B. I. Van Der Waals Density Functional for General Geometries. *Phys. Rev. Lett.* **2004**, *92* (24), 246401–1.

(97) Román-Pérez, G.; Soler, J. M. Efficient Implementation of a van Der Waals Density

Functional: Application to Double-Wall Carbon Nanotubes. *Phys. Rev. Lett.* **2009**, *103* (9), 96102.

(98) Klimeš, J.; Bowler, D. R.; Michaelides, A. Chemical Accuracy for the van Der Waals Density Functional. *J. Phys. Condens. Matter* **2010**, *22* (2), 22201.

(99) Lee, K.; Murray, É. D.; Kong, L.; Lundqvist, B. I.; Langreth, D. C. Higher-Accuracy van Der Waals Density Functional. *Phys. Rev. B - Condens. Matter Mater. Phys.* **2010**, *82* (8).

(100) Klime, J.; Bowler, D. R.; Michaelides, A. Van Der Waals Density Functionals Applied to Solids. *Phys. Rev. B - Condens. Matter Mater. Phys.* **2011**, *83* (19), 1–13.

(101) Thonhauser, T.; Cooper, V. R.; Li, S.; Puzder, A.; Hyldgaard, P.; Langreth, D. C. Van Der Waals Density Functional: Self-Consistent Potential and the Nature of the van Der Waals Bond. *Phys. Rev. B - Condens. Matter Mater. Phys.* **2007**, *76* (12), 1–11.

(102) Mori-Sánchez, P.; Cohen, A. J.; Yang, W. Many-Electron Self-Interaction Error in Approximate Density Functionals. *J. Chem. Phys.* **2006**, *125* (20), 201102.

(103) Heyd, J.; Scuseria, G. E.; Ernzerhof, M. Hybrid Functionals Based on a Screened Coulomb Potential. *J. Chem. Phys.* **2003**, *118* (18), 8207.

(104) Krukau, A. V; Vydrov, O. a; Izmaylov, A. F.; Scuseria, G. E. Influence of the Exchange Screening Parameter on the Performance of Screened Hybrid Functionals. *J. Chem. Phys.* **2006**, *125* (22), 224106.

(105) Perdew, J. P.; Burke, K.; Ernzerhof, M. Generalized Gradient Approximation Made Simple. *Phys. Rev. Lett.* **1996**, *77* (18), 3865–3868.

(106) Lambrecht, W. R. L. Which Electronic Structure Method for the Study of Defects: A Commentary. *Phys. Status Solidi B* **2011**, *248* (7), 1547–1558.

(107) Alkauskas, A.; Broqvist, P.; Pasquarello, A. Defect Levels Through Hybrid Density Functionals: Insights and Applications. *Phys. Status Solidi B* **2011**, *248* (4), 775–789.

(108) Choi, M.; Janotti, A.; Van de Walle, C. G. Native Point Defects and Dangling Bonds in α-Al_2O_3. *J. Appl. Phys.* **2013**, *113* (4), 44501.

(109) Shishkin, M.; Kresse, G. Self-Consistent GW Calculations for Semiconductors and Insulators. *Phys. Rev. B* **2007**, *75* (23), 235102.

(110) Shishkin, M.; Marsman, M.; Kresse, G. Accurate Quasiparticle Spectra from Self-Consistent GW Calculations with Vertex Corrections. *Phys. Rev. Lett.* **2007**, *99* (24), 246403.

(111) Aulbur, W. G.; Jönsson, L.; Wilkins, J. W. Quasiparticle Calculations in Solids. *Solid State Phys.* **1999**, *54*, 1–218.

(112) Hedin, L. New Method for Calculating the One-Particle Green's Function with Application to the Electron-Gas Problem. *Phys. Rev.* **1965**, *139* (3A), A796–A823.

(113) Shishkin, M.; Kresse, G. Implementation and Performance of the Frequency-Dependent GW Method within the PAW Framework. *Phys. Rev. B* **2006**, *74* (3), 35101.

(114) Fuchs, F.; Furthmüller, J.; Bechstedt, F.; Shishkin, M.; Kresse, G. Quasiparticle Band Structure Based on a Generalized Kohn-Sham Scheme. *Phys. Rev. B* **2007**, *76* (11), 115109.

(115) Kresse, G.; Hafner, J. Ab Initio Molecular-Dynamics Simulation of the Liquid-Metal-Amorphous-Semiconductor Transition in Germanium. *Phys. Rev. B* **1994**, *49* (20), 14251–14269.

(116) Kresse, G.; Furthmüller, J. Efficient Iterative Schemes for Ab Initio Total-Energy Calculations Using a Plane-Wave Basis Set. *Phys. Rev. B. Condens. Matter* **1996**, *54* (16), 11169–11186.

(117) Kresse, G.; Furthmüller, J. Efficiency of Ab-Initio Total Energy Calculations for Metals and Semiconductors Using a Plane-Wave Basis Set. *Comput. Mater. Sci.* **1996**, *6* (1), 15–50.

(118) Kresse, G.; Hafner, J. Ab Initio Molecular Dynamics for Liquid Metals. *Phys. Rev. B* **1993**, *47* (1), 558–561.

(119) Blöchl, P. E. Projector Augmented-Wave Method. *Phys. Rev. B* **1994**, *50* (24), 17953.

(120) Monkhorst, H.; Pack, J. Special Points for Brillouin-Zone Integrations. *Phys. Rev. B* **1976**, *13* (12), 5188–5192.

(121) Momma, K.; Izumi, F. VESTA : A Three-Dimensional Visualization System for Electronic and Structural Analysis. *J. Appl. Crystallogr.* **2008**, *41* (3), 653–658.

(122) Kudo, T.; Fueki, K. *Solid State Ionics*; Kodansha VCH: Tokyo, Japan Weinheim, F.R.G. New York, NY, USA, 1990.

(123) Tilley, R. J. D. *Defects in Solids*; John Wiley & Sons, Inc., 2008.

(124) Kröger, F. A. *The Chemistry of Imperfect Crystals.*; North-Holland Pub. Co.; American Elsevier: Amsterdam, New York, 1973.

(125) Makov, G.; Payne, M. C. Periodic Boundary Conditions in Ab Initio Calculations. *Phys. Rev. B* **1995**, *51* (7), 4014–4022.

(126) Komsa, H.-P.; Rantala, T. T.; Pasquarello, A. Finite-Size Supercell Correction Schemes for Charged Defect Calculations. *Phys. Rev. B* **2012**, *86* (4), 45112.

(127) Taylor, S. E.; Bruneval, F. Understanding and Correcting the Spurious Interactions in Charged Supercells. *Phys. Rev. B* **2011**, *84* (7), 75155.

(128) Chase Jr., M. W. *NIST-JANAF Thermochemical Tables*; 1998.

(129) Wang, L.; Maxisch, T.; Ceder, G. Oxidation Energies of Transition Metal Oxides within the GGA+U Framework. *Phys. Rev. B* **2006**, *73* (19), 1–6.

(130) Kurth, S.; Perdew, J. P.; Blaha, P. Molecular and Solid-State Tests of Density Functional Approximations: LSD, GGAs, and Meta-GGAs. *Int. J. Quantum Chem.* **1999**, *75* (4-5), 889.

(131) Hummelshøj, J. S.; Luntz, a C.; Nørskov, J. K. Theoretical Evidence for Low Kinetic

Overpotentials in Li-O_2 Electrochemistry. *J. Chem. Phys.* **2013**, *138* (3), 34703.

(132) Sholl, D. S.; Steckel, J. A. *Density Functional Theory: A Practical Introduction*; Wiley: Hoboken, N.J., 2009.

(133) Jónsson, H.; Mills, G.; Jacobsen, K. W. Nudged Elastic Band Method for Finding Minimum Energy Paths of Transitions. In *Classical And Quantum Dynamics In Condensed Phase Simulations*; Berne, B. J., Ciccotti, G., Coker, D. F., Eds.; World Scientific, 1998; pp 385–404.

(134) Grubmüller, H.; Heller, H.; Windemuth, A.; Schulten, K. Generalized Verlet Algorithm for Efficient Molecular Dynamics Simulations with Long-Range Interactions. *Mol. Simul.* **1991**, *6* (1–3), 121–142.

(135) Adams, S.; Rao, R. P. Ion Transport and Phase Transition in $Li_{7-x}La_3(Zr_{2-x}M_X)O_{12}$(M = Ta^{5+}, Nb^{5+}, X = 0, 0.25). *J. Mater. Chem.* **2012**, *22* (4), 1426–1434.

(136) Adams, S.; Prasada Rao, R. Simulated Defect and Interface Engineering for High Power Li Electrode Materials. *Solid State Ionics* **2011**, *184* (1), 57–61.

(137) Adams, S.; Rao, R. P. High Power Lithium Ion Battery Materials by Computational Design. *Phys. status solidi* **2011**, *208* (8), 1746–1753.

(138) Plimpton, S. Fast Parallel Algorithms for Short-Range Molecular Dynamics. *J. Comput. Phys.* **1995**, *117* (1), 1–19.

(139) Gerbig, O.; Merkle, R.; Maier, J. Electrical Transport and Oxygen Exchange in the Superoxides of Potassium, Rubidium, and Cesium. *Adv. Funct. Mater.* **2015**, n/a-n/a.

(140) Garcia-Lastra, J. M.; Myrdal, J. S. G.; Christensen, R.; Thygesen, K. S.; Vegge, T. DFT+U Study of Polaronic Conduction in Li_2O_2 and Li_2CO_3 : Implications for Li–Air Batteries. *J. Phys. Chem. C* **2013**, *117* (11), 5568–5577.

(141) Varley, J. B.; Viswanathan, V.; Nørskov, J. K.; Luntz, a. C. Lithium and Oxygen Vacancies and Their Role in Li2O2 Charge Transport in Li–O2 Batteries. *Energy Environ. Sci.* **2014**, *7* (2), 720.

(142) Kang, J.; Jung, Y. S.; Wei, S.-H.; Dillon, A. C. Implications of the Formation of Small Polarons in Li_2O_2 for Li-Air Batteries. *Phys. Rev. B* **2012**, *85* (3), 35210.

(143) Gerbig, O.; Merkle, R.; Maier, J. Electron and Ion Transport in Li_2O_2. *Adv. Mterials* **2013**, *25* (22), 3129–3133.

(144) Araujo, R. B.; Chakraborty, S.; Ahuja, R. Unveiling the Charge Migration Mechanism in Na_2O_2 : Implications for Sodium–air Batteries. *Phys. Chem. Chem. Phys.* **2015**, *17*, 8203–8209.

(145) Kresse, G.; Hafner, J. Ab Initio Molecular-Dynamics Simulation of the Liquid-Metal–amorphous-Semiconductor Transition in Germanium. *Phys. Rev. B* **1994**, *49* (20), 14251–14269.

(146) Kováčik, R.; Werner, P.; Dymkowski, K.; Ederer, C. Rubidium Superoxide: A P-Electron Mott Insulator. *Phys. Rev. B* **2012**, *86* (7), 75130.

(147) Kim, M.; Min, B. I. Temperature-Dependent Orbital Physics in a Spin-Orbital-Lattice-Coupled 2p Electron Mott System: The Case of K. *Phys. Rev. B* **2014**, *89* (12), 121106.

(148) Perdew, J.; Burke, K.; Ernzerhof, M. Generalized Gradient Approximation Made Simple. *Phys. Rev. Lett.* **1996**, *77* (18), 3865–3868.

(149) Tallman, R. L.; Margrave, J. L.; Bailey, S. W. THE CRYSTAL STRUCTURE OF SODIUM PEROXIDE. *J. Am. Chem. Soc.* **1957**, *79* (11), 2979–2980.

(150) Wriedt, H. A. The Na − O (Sodium-Oxygen) System. *Bull. Alloy Phase Diagrams* **1987**, *8* (3), 234–246.

(151) Carter, G. F.; Templeton, D. H. Polymorphism of Sodium Superoxide. *J. Am. Chem. Soc.* **1953**, *75* (21), 5247–5249.

(152) Templeton, D. H.; Dauben, C. H. The Crystal Structure of Sodium Superoxide. *J. Am. Chem. Soc.* **1950**, *72* (5), 2251–2254.

(153) Tian, F.; Radin, M. D.; Siegel, D. J. Enhanced Charge Transport in Amorphous Li_2O_2. *Chem. Mater.* **2014**, *26* (9), 2952–2959.

(154) Radin, M. D.; Tian, F.; Siegel, D. J. Electronic Structure of Li_2O_2 {0001} Surfaces. *J. Mater. Sci.* **2012**, *47* (21), 7564–7570.

(155) Van de Walle, C. G. First-Principles Calculations for Defects and Impurities: Applications to III-Nitrides. *J. Appl. Phys.* **2004**, *95* (8), 3851.

(156) Chambers, C.; Master, S. C.; Holliday, A. K. *Modern Inorganic Chemistry*; Butterworth & Co Publishers Ltd, 1975.

(157) Hummelshøj, J. S.; Blomqvist, J.; Datta, S.; Vegge, T.; Rossmeisl, J.; Thygesen, K. S.; Luntz, a C.; Jacobsen, K. W.; Nørskov, J. K. Communications: Elementary Oxygen Electrode Reactions in the Aprotic Li-Air Battery. *J. Chem. Phys.* **2010**, *132* (7), 71101.

(158) Dunst, a.; Epp, V.; Hanzu, I.; Freunberger, S. a.; Wilkening, M. Short-Range Li Diffusion vs. Long-Range Ionic Conduction in Nanocrystalline Lithium Peroxide Li_2O_2 —the Discharge Product in Lithium-Air Batteries. *Energy Environ. Sci.* **2014**, *7* (8), 2739.

(159) Herranz, J.; Garsuch, A.; Gasteiger, H. a. Using Rotating Ring Disc Electrode Voltammetry to Quantify the Superoxide Radical Stability of Aprotic Li–Air Battery Electrolytes. *J. Phys. Chem. C* **2012**, *116* (36), 19084–19094.

(160) Kang, S.; Mo, Y.; Ong, S. P.; Ceder, G. A Facile Mechanism for Recharging Li_2O_2 in Li–O_2 Batteries. *Chem. Mater.* **2013**, *25* (16), 3328–3336.

(161) Geng, W.; He, B.; Ohno, T. Grain Boundary Induced Conductivity in Li_2O_2. *J. Phys. Chem. C* **2013**, *117* (48), 25222–25228.

(162) Gallant, B.; Mitchell, R. Chemical and Morphological Changes of Li–O_2 Battery Electrodes upon Cycling. *J. Chem. Phys. Lett.* **2012**, *116* (39), 20800–20805.

(163) McCloskey, B. D.; Bethune, D. S.; Shelby, R. M.; Girishkumar, G.; Luntz, A. C. Solvents Critical Role in Nonaqueous Lithium-Oxygen Battery Electrochemistry. *J. Phys. Chem.*

Lett. **2011**, *2* (10), 1161–1166.

(164) Ottakam Thotiyl, M. M.; Freunberger, S. a; Peng, Z.; Bruce, P. G. The Carbon Electrode in Nonaqueous Li-O_2 Cells. *J. Am. Chem. Soc.* **2013**, *135* (1), 494–500.

(165) Yang, J.; Zhai, D.; Wang, H.-H.; Lau, K. C.; Schlueter, J. a; Du, P.; Myers, D. J.; Sun, Y.-K.; Curtiss, L. a; Amine, K. Evidence for Lithium Superoxide-like Species in the Discharge Product of a Li-O_2 Battery. *Phys. Chem. Chem. Phys.* **2013**, *15* (11), 3764–3771.

(166) Yang, S.; Siegel, D. J. Intrinsic Conductivity in Sodium–Air Battery Discharge Phases: Sodium Superoxide vs Sodium Peroxide. *Chem. Mater.* **2015**, *27* (11), 3852–3860.

(167) Solovyev, I. V. Spin-Orbital Superexchange Physics Emerging from Interacting Oxygen Molecules in KO_2. *New J. Phys.* **2008**, *10* (1), 13035.

(168) Li, S.; Liu, J.; Liu, B. First-Principles Study of the Charge Transport Mechanisms in Lithium Superoxide. *Chem. Mater.* **2017**.

(169) Radin, M. D. First-Principles and Continuum Modeling of Charge Transport in Li-O_2 Batteries. *J. Chem. Inf. Model.* **2013**, *53* (9), 1689–1699.

(170) David, I. N.; Thompson, T.; Wolfenstine, J.; Allen, J. L.; Sakamoto, J. Microstructure and Li-Ion Conductivity of Hot-Pressed Cubic $Li_7La_3Zr_2O_{12}$. *J. Am. Ceram. Soc.* **2015**, *98* (4), 1209–1214.

(171) Allen, J. L.; Wolfenstine, J.; Rangasamy, E.; Sakamoto, J. Effect of Substitution (Ta, Al, Ga) on the Conductivity of $Li_7La_3Zr_2O_{12}$. *J. Power Sources* **2012**, *206*, 315–319.

(172) Rangasamy, E.; Wolfenstine, J.; Sakamoto, J. The Role of Al and Li Concentration on the Formation of Cubic Garnet Solid Electrolyte of Nominal Composition $Li_7La_3Zr_2O_{12}$. *Solid State Ionics* **2012**, *206*, 28–32.

(173) Rettenwander, D.; Blaha, P.; Laskowski, R.; Schwarz, K.; Bottke, P.; Wilkening, M.; Geiger, C. a.; Amthauer, G. DFT Study of the Role of Al^{3+} in the Fast Ion-Conductor $Li_{7-3X}Al_{3+X}La_3Zr_2O_{12}$ Garnet. *Chem. Mater.* **2014**, *26* (8), 2617–2623.

(174) Hart, G. L. W.; Nelson, L. J.; Forcade, R. W. Generating Derivative Structures at a Fixed Concentration. *Comp. Mater. Sci.* **2012**, *59*, 101–107.

(175) Hart, G. L. W.; Forcade, R. W. Generating Derivative Structures from Multilattices: Algorithm and Application to Hcp Alloys. *Phys. Rev. B - Condens. Matter Mater. Phys.* **2009**, *80* (1), 1–8.

(176) Hart, G. L. W.; Forcade, R. W. Algorithm for Generating Derivative Structures. *Phys. Rev. B - Condens. Matter Mater. Phys.* **2008**, *77* (22), 1–12.

(177) Ong, S. P.; Richards, W. D.; Jain, A.; Hautier, G.; Kocher, M.; Cholia, S.; Gunter, D.; Chevrier, V. L.; Persson, K. A.; Ceder, G. Python Materials Genomics (Pymatgen): A Robust, Open-Source Python Library for Materials Analysis. *Comput. Mater. Sci.* **2013**, *68*, 314–319.

(178) Prasada Rao, R.; Tho, T. D.; Adams, S. Ion Transport Pathways in Molecular Dynamics

Simulated Lithium Silicate Glasses. *Solid State Ionics* **2010**, *181* (1–2), 1–6.

(179) Mukhopadhyay, S.; Thompson, T.; Sakamoto, J.; Huq, A.; Wolfenstine, J.; Allen, J. L.; Bernstein, N.; Stewart, D. A.; Johannes, M. D. Structure and Stoichiometry in Supervalent Doped $Li_7La_3Zr_2O_{12}$. *Chem. Mater.* **2015**, *27* (10), 3658–3665.

(180) Jalem, R.; Rushton, M. J. D.; Manalastas, W.; Nakayama, M.; Kasuga, T.; Kilner, J. a.; Grimes, R. W. Effects of Gallium Doping in Garnet-Type $Li_7La_3Zr_2O_{12}$ Solid Electrolytes. *Chem. Mater.* **2015**, *27* (8), 2821–2831.

(181) Mukhopadhyay, S.; Thompson, T.; Sakamoto, J.; Huq, A.; Wolfenstine, J.; Allen, J. L.; Bernstein, N.; Stewart, D. a.; Johannes, M. D. Structure and Stoichiometry in Supervalent Doped $Li_7La_3Zr_2O_{12}$. *Chem. Mater.* **2015**, 150420005135003.

(182) Xia, W.; Xu, B.; Duan, H.; Guo, Y.; Kang, H.; Li, H.; Liu, H. Ionic Conductivity and Air Stability of Al-Doped $Li_7La_3Zr_2O_{12}$ Sintered in Alumina and Pt Crucibles. *ACS Appl. Mater. Interfaces* **2016**, *8* (8), 5335–5342.

(183) Buschmann, H.; Dölle, J.; Berendts, S.; Kuhn, A.; Bottke, P.; Wilkening, M.; Heitjans, P.; Senyshyn, A.; Ehrenberg, H.; Lotnyk, A.; Duppel, V.; Kienle, L.; Janek, J. Structure and Dynamics of the Fast Lithium Ion Conductor "$Li_7La_3Zr_2O_{12}$." *Phys. Chem. Chem. Phys.* **2011**, *13* (43), 19378.

(184) Willems, T. F.; Rycroft, C. H.; Kazi, M.; Meza, J. C.; Haranczyk, M. Algorithms and Tools for High-Throughput Geometry-Based Analysis of Crystalline Porous Materials. *Microporous Mesoporous Mater.* **2012**, *149* (1), 134–141.

(185) Chen, Y.; Rangasamy, E.; Liang, C.; An, K. Origin of High Li + Conduction in Doped Li $_7La_3Zr_2O_{12}$ Garnets. *Chem. Mater.* **2015**, *27* (16), 5491–5494.

(186) Lu, Y.-C.; Kwabi, D. G.; Yao, K. P. C.; Harding, J. R.; Zhou, J.; Zuin, L.; Shao-Horn, Y. The Discharge Rate Capability of Rechargeable Li–O_2 Batteries. *Energy Environ. Sci.* **2011**, *4* (8), 2999.

(187) Yongliang Li, Hossein Yadegari, Xifei Li, Mohammad N. Banis, Ruying Li, and X. S. Superior Catalytic Activity of Nitrogen-Doped Graphene Cathode for High Energy Capacity Sodium-Air Batteries. *Chem. Commun. (Camb).* **2013**, No. 207890.

(188) Zhuravlev, Y. N.; Kravchenko, N. G.; Obolonskaya, O. S. The Electronic Structure of Alkali Metal Oxides. *Russ. J. Phys. Chem. B* **2010**, *4* (1), 20–28.